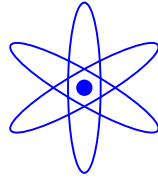


PHYSIK-DEPARTMENT



Doktorarbeit

Gamma-ray Bursts: Exploring the Early Universe

Aybüke Küpcü Yoldaş

TECHNISCHE UNIVERSITÄT MÜNCHEN



MAX-PLANCK-INSTITUT FÜR EXTRATERRESTRISCHE PHYSIK

Gamma-ray Bursts: Exploring the Early Universe

Aybüke Küpcü Yoldaş

Vollständiger Abdruck der von der Fakultät für Physik der Technischen Universität München zur Erlangung des akademischen Grades eines

Doktors der Naturwissenschaften

genehmigten Dissertation.

Vorsitzender: Univ.-Prof. Dr. W. Zwirger
Prüfer: 1. Hon.-Prof. Dr. G. Hasinger
2. Univ.-Prof. Dr. F. von Feilitzsch

Die Dissertation wurde am 17.11.2006 bei der Technischen Universität München eingereicht und durch die Fakultät für Physik am 19.12.2006 angenommen.

Abstract

Gamma-ray bursts (GRBs) are auspicious tools which can be used to probe cosmological distances with their bright prompt and afterglow emission that is detectable up to redshifts of $z \sim 20$. In that respect they offer the unique possibility to study galaxy formation, cosmic re-ionization and the star formation history of the Universe. However, the nature of the GRBs and the relation to their host galaxies must be well understood in order to use them as cosmological tools. This thesis comprises of different aspects of GRBs and their host galaxies based on afterglow and host galaxy observations using various methods; i.e. morphological, photometric and spectral analysis.

GRBs are variable sources with a decreasing flux that makes it difficult to observe the sources later in time, and thus requires rapid and systematic follow-up observations. The 7-band (griz JHK) imager GROND, which will be mounted at the ESO/MPI 2.2m telescope, is dedicated to GRB afterglow observations. The main aim of GROND is to determine the photometric redshift of GRBs within 30 minutes with an accuracy of 0.3 - 0.5 in z up to $z \sim 13$. This speed and accuracy can only be achieved by automated software for telescope control and data analysis. The GROND Pipeline (GP) system is developed to automate both the observations and the data analysis. The software autonomously controls the whole process: i) receiving GRB alerts from gamma-ray satellites (i.e. Swift, GLAST etc.), ii) scheduling observations for the night, iii) starting, controlling and stopping the observations, iv) reducing the data and conducting astrometric and photometric analysis, v) identifying the optical/near-infrared afterglow of the GRB among all the objects observed within the field of view, and vi) determining its redshift by fitting the spectral energy distribution (SED) of the afterglow constructed using 7 broadband filters. In other words, the GP system should act intelligently to conduct the analysis and decisions that are normally done by astronomers. I brought the approach of an astronomer to the GP which consisted of co-designing several parts of the system related to observations and data analysis, i.e. the GRB follow-up decision mechanism using GRB alert packets, the algorithm for scheduling the observations, analysis strategies of the observation blocks and of the photometric redshift determination. Furthermore I coded the automated photometric analysis component of the GP.

It is proposed that GRBs can themselves be used cosmologically to trace the star-formation rate (SFR) history of the Universe if they are connected with massive stars. Long duration (> 2 s) GRBs are generally believed to originate from explosions of very massive stars ($\sim 40 M_{\odot}$) and this has been supported by the detection of supernovae underlying the GRB afterglows and other evidence from host galaxy studies. One other indicator about the nature of the GRB progenitor is the density of the circumburst environment. The prompt

gamma/X-ray emission and the X-ray and UV afterglow emission is expected to photoionize the circumburst environment and thus, lead to time dependent absorption and emission line features, and also recombination line features. The line fluxes and recombination time scale depend on the density and temperature of the circumburst environment, which are expected to be different than the normal interstellar medium values, around massive stars like Wolf-Rayet stars. The spectral time-series analysis of the host galaxy of GRB 990712 is the first case that emission from cooling GRB remnants is probed on a time scale of years. We find that the emission line fluxes show no variation within the uncertainties up to 6 years after the burst. The lack of time variability in the [O III] λ 5007 line, combined with the $\lesssim 5$ ratio of the [O III] λ 5007/H β lines, has allowed us to set an upper limit to the contribution from the cooling gas. This limit is used to constrain the allowed range of densities within a region of about 2 parsec surrounding the burst.

Another important tool to probe the early Universe is the host galaxies in which GRBs reside. For nearly all well-localized GRBs a host galaxy has been observed after the decay of the afterglow. The current sample of long duration GRB host galaxies consists of ~ 80 members. The sample of GRB host galaxies differ from a normal galaxy sample as it is neither flux nor volume limited, and using GRBs, it is possible to probe redshifts much higher than those spanned by present optically-selected galaxy samples. The study of the known sample is crucial for our understanding of the general properties of GRB hosts, in view of future observations of hosts at very high redshifts. However only a small sample has detailed observations, most of which are faint compact blue galaxies with low stellar masses.

The host galaxy of GRB 011121 ($z = 0.36$) is one of the most extensively and deeply imaged hosts among low redshift ($z < 0.7$) cosmological GRBs, giving us the unique possibility to study the host galaxy properties through the parameter space from morphology to stellar mass. The surface brightness profile of the galaxy is best fitted by a Sersic law with index $n \sim 2 - 2.5$ and a rather large effective radius of ~ 7.5 kpc. The morphological analysis and the F450W - F702W colour image suggest that the host galaxy of GRB 011121 is either a disk-system with a rather small bulge, or a galaxy hosting a central, dust-enshrouded starburst. Therefore, the integrated spectral energy distribution of the galaxy is modelled by combining stellar population and radiative transfer models of starburst and normal star-forming, Sbc-like galaxies. A range of plausible fitting solutions indicates that the host galaxy of GRB 011121 has a stellar mass of $3.1 - 6.9 \times 10^9 M_{\odot}$, stellar populations with a maximum age ranging from 0.4 to 2 Gyr, and a metallicity ranging from 1 to 29 per cent of the solar value. Our results suggest that the host galaxy of GRB 011121 is a rather large disk-system in a relatively early phase of its star formation history. Therefore, the size and type of the galaxy prevents its classification as a dwarf galaxy, although the other galaxy properties, such as stellar mass, metallicity and colors, are in agreement with those of a relatively well studied subsample of GRB host galaxies.

Contents

Abstract	i
1 Introduction	1
1.1 Gamma-ray Bursts	1
1.1.1 Prompt emission	1
1.1.2 Afterglow emission	3
1.1.3 Fireball Model	5
1.1.4 Host Galaxies	8
1.1.5 Progenitors	10
1.2 High Redshift GRBs	12
1.2.1 The motivation	12
1.2.2 Present Strategies	14
1.2.3 A new instrument: GROND	15
2 Probing High Redshift: Automated Photometry with GROND Pipeline	21
2.1 The GROND Pipeline	21
2.2 System layer: Observing GRB Afterglows	24
2.2.1 Receiving GRB Alerts	24
2.2.2 Scheduling of Observations	28
2.2.3 Automating the GRB Afterglow Observations	35
2.3 Analysis layer: Analysing GRB Afterglow Observations	38
2.3.1 Preparing for Analysis	40
2.3.2 Analysing each Observation Block	40
2.3.3 Photometric Analysis	42
2.3.4 Multi-band Photometric Calibration	47
2.3.5 Identifying the GRB Afterglow	49
2.3.6 Determining the Photometric Redshift	51
2.4 Summary	55
3 Nature of the Gamma-ray Burst Progenitors	57
3.1 Probing the close environment of GRBs through photoionization	57
3.2 The first example: Constraining the environment of GRB 990712	60
3.2.1 GRB 990712	61
3.2.2 Data Reduction and Analysis	61
3.2.3 The circumburst environment	65
3.2.4 Star formation rate and metallicity	66

3.2.5	Summary	67
4	Host Galaxies – An interesting case study: The Host Galaxy of GRB 011121	69
4.1	GRB 011121	69
4.2	Data reduction	70
4.2.1	Astrometry	73
4.2.2	Extinction	73
4.3	Morphology of the host galaxy	74
4.4	Photometry	77
4.5	Analysis of the Spectral Energy Distribution	78
4.5.1	Analysis using HyperZ	78
4.5.2	Broad-band SED fitting	81
4.6	Star Formation Rate	87
4.7	Summary	88
5	Conclusions	91
	Bibliography	95
	Acknowledgements	103

1 Introduction

1.1 Gamma-ray Bursts

Gamma-ray bursts (GRBs) are the most energetic cosmological explosions in the Universe, emitting energies on the order of 10^{52} erg in a very short time interval ranging from milliseconds to minutes. The prompt emission is released in γ -rays from a few keV in some cases up to GeV range, with a peak energy around a few hundred keV. In most cases, the prompt emission is observed to be followed by a long lasting afterglow emission in lower energies from X-rays to radio.

GRBs were first discovered by Vela satellites in 1967, in search for possible nuclear explosions on Earth that would violate Nuclear Test Ban Treaty. This discovery was announced to the scientific community in 1973, as a new mysterious cosmic phenomenon (Klebesadel et al. 1973). The first important observational contribution to explain the origin of GRBs was achieved after the launch of Burst and Transient Source Experiment (BATSE) instrument on-board Compton Gamma-ray Observatory in 1991 (Fishman & Meegan 1995). Through its operation-time of over 10 years, BATSE detected several thousands bursts that were distributed isotropically. The isotropic distribution was the first strong indication of a cosmic origin for these events (Fenimore et al. 1993). The evident proof came with Beppo-SAX in 1997, with the detection of fading X-ray emission after the GRB events (Costa et al. 1997). The afterglow emission in X-rays significantly improved the localization of GRBs and made it possible to conduct follow-up observations in optical and longer wavelengths. The discovery of the GRB afterglows in longer wavelengths yielded the measurement of the redshift of GRBs, establishing their cosmological nature (van Paradijs et al. 1997).

Despite these recent observational discoveries, the origin and physics of GRBs continues to be a challenging problem.

1.1.1 Prompt emission

GRBs fall into two subclasses based solely on the spectral and temporal properties of their prompt γ -ray emission. The long-soft GRBs are those that have a soft spectrum and emit 90% of the prompt γ radiation in longer than 2 seconds. The duration in which the 90% of the prompt emission is radiated is called T_{90} , and used as a conventional measure for the duration of GRBs. The other subclass is short-hard GRBs, which have a T_{90} less than 2 seconds and a harder spectrum.

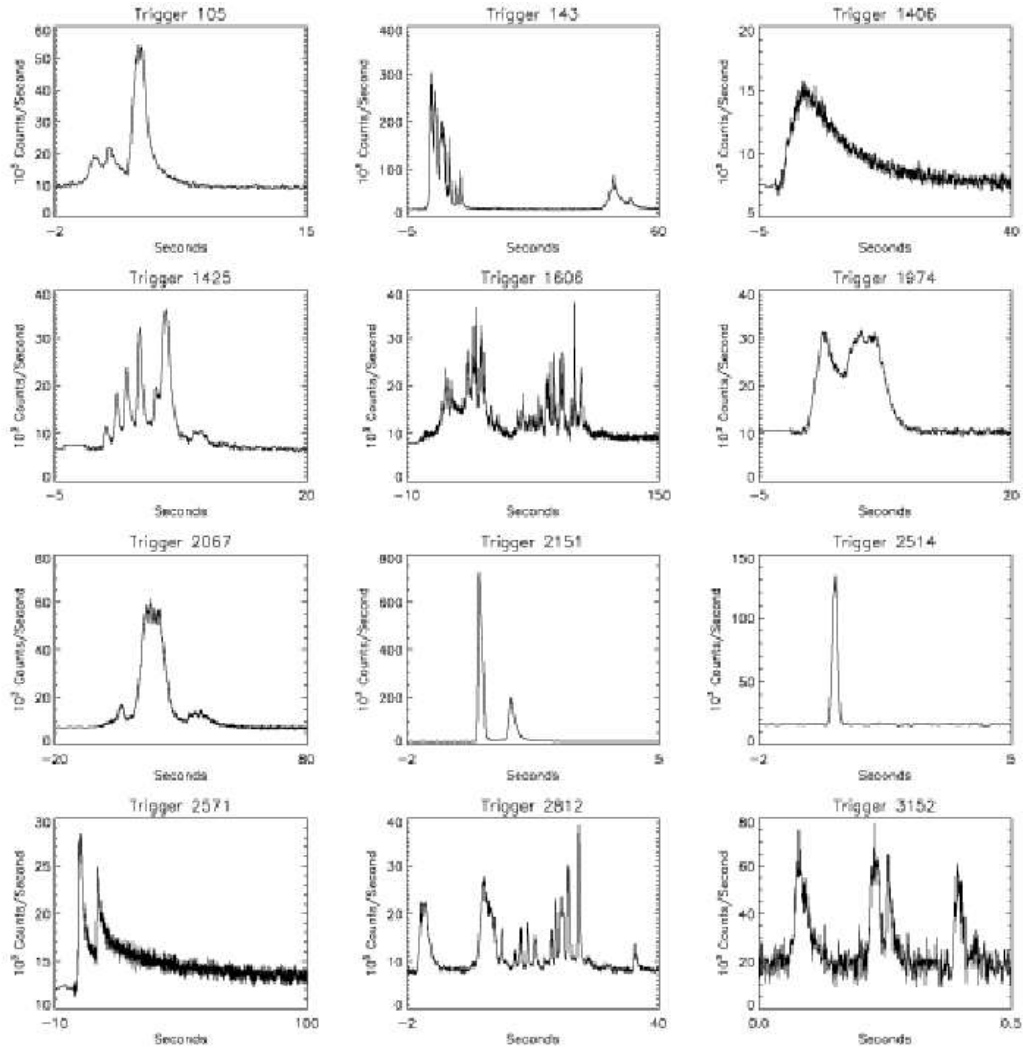


Figure 1.1: Some examples of prompt γ -ray light-curve of GRBs.

GRBs exhibit non-thermal γ -ray spectra. In general, the spectrum of a GRB can be well described by a Band function. It is an empirical function which is a combination of two power laws with indices α and β , joined smoothly at a break energy E_0 . In general for bright BATSE bursts, the break energy ranges between 100 and 1000 keV, with a distribution peaking around 250 keV (Preece et al. 2000). However, there is also a subclass of GRBs, namely X-ray Flashes (XRFs), that have softer spectra and lower peak energies (Heise et al. 2001; Kippen et al. 2003).

The prompt emission of GRBs is explored into a softer wavelength range and with better sensitivity by the Swift mission. Swift satellite has three instruments on board; namely BAT, XRT and UVOT. BAT (Burst Alert Telescope) is a wide-field γ -ray detector sensitive to an energy range of 15 – 150 keV. XRT (X-Ray Telescope) is equipped with an X-ray detector sensitive to an energy range of 0.3 – 10 keV. It is designed to do X-ray imaging and spectroscopy of GRB afterglows. UVOT (UV/Optical Telescope) is equipped with UV and optical filters for imaging and a grism for spectroscopy, and it can observe for 170 – 650 nm wavelength range. When BAT triggers for a GRB, Swift slews to that direction so that in addition to the observation of the prompt γ -ray emission with BAT, it also observes the X-ray and UV/optical afterglow emission of the GRB with XRT and UVOT, respectively. As the energy range of BATSE and Swift are different, the classification of GRBs in terms of spectral hardness is not that distinct anymore. In fact, there is now a clear indication that the prompt emission is followed by a softer decaying component independent of the subclass of the GRB.

1.1.2 Afterglow emission

The afterglow emission starts during or after the prompt γ -ray event, and lasts up to several months with a decreasing flux. It exhibits a non-thermal behaviour and can be represented by a power-law emission, as in the case of the prompt γ -ray emission itself.

The X-ray afterglow of GRB 970228 was the first detected GRB afterglow ever (Costa et al. 1997). Since then, X-ray afterglows have been observed for many GRBs. In fact, Swift has observed X-ray emission with XRT for more than 80% of GRBs detected with BAT. The X-ray emission starts fast after or even during the GRB, and lasts from several hours up to several days. Integrated over the first 7 – 10 days, the X-ray afterglow typically contains the same energy as the primary γ -ray burst itself. It is very useful to localize the event up to few arcseconds as opposed to γ -rays which can be localized only up to few arcminutes with the best current instrument; i.e. Swift BAT. There had been claims for line emission in the X-ray spectra of several GRBs observed with different instruments. However both the statistical significance and the interpretation of the line emission are still under debate.

The next range of wavelengths popular for GRB afterglow science is the optical and infrared (IR) wavelength range. This wavelength range has the great advantage of the usage of most developed instruments that allow detailed photometry and spectroscopy allowing the determination of the redshift of the GRB and further analysis on its origin and nature. The

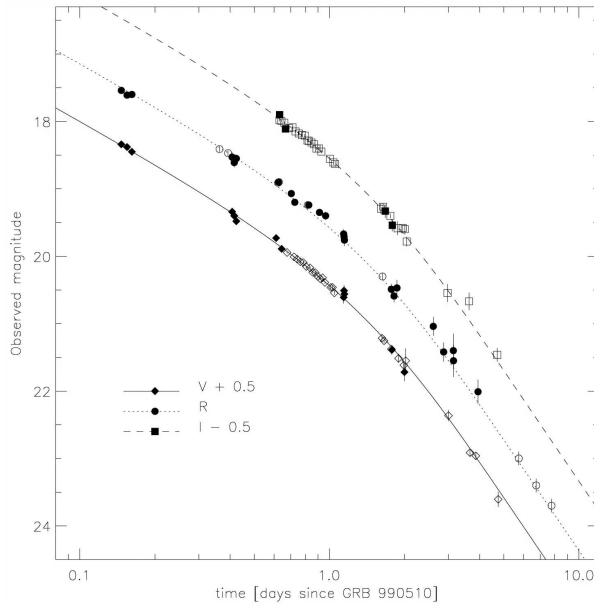


Figure 1.2: The jet break observed in GRB 990510, taken from Harrison et al. (1999).

optical/IR afterglow is observed for about 50% of well localized GRBs. Due to technical reasons (i.e., lack of prompt response and/or deep enough flux limits in the search of optical/IR afterglows), we do not have enough statistics to conclude on the starting time of the optical/IR afterglow. Usually it lasts from several days up to several months in extreme cases.

The difference of the detection statistics between optical and X-ray afterglows led to a classification called “dark GRBs”. In the beginning, the term “dark GRB” was used for all GRBs with no optical afterglow. Later on there had been more specific and systematic definitions comparing the X-ray and optical afterglow flux or detection limits. Nevertheless, the nature of the dark GRBs is still not clear. There are several explanations suggested such as, a very high absorption in the vicinity of the GRB, a very high redshift so that the Lyman break is redshifted beyond the optical range, or intrinsically faint GRB afterglows.

Both X-ray and optical afterglow flux have a power-law dependence on the frequency and time, described as $f_{\nu}(t) \propto \nu^{-\beta} t^{-\alpha}$. The typical indices for the X-ray afterglow are $\alpha \sim 1.4$ and $\beta \sim 0.9$. For a typical optical afterglow α is 1.2. There have been achromatic breaks to a steeper decline of $\alpha \sim 2$, observed in the optical afterglow light curves. These breaks are generally interpreted as “jet breaks” indicating the collimated nature of the emission. The jet breaks and the nature of the emission will be discussed in more detail under the Fireball Model section.

Also in many cases, bumps underlying the afterglow power-law spectra were observed at several weeks after the GRB. These bumps are interpreted as evidence for an underlying supernova (SN). However, the most significant proof was achieved by the spectroscopical confirmation of an underlying SN, for four GRB, which will be discussed in more detail

under the Progenitor section.

In general, the optical/IR range provides the most valuable information for GRBs, concerning their nature and progenitors, as well as providing their redshift. The current redshift range spanned by GRBs is $0.0085 - 6.29^1$ (Galama et al. 1998; Kawai et al. 2006). The huge luminosities of GRBs provide their detectability up to redshifts of ~ 20 , making them very promising tools to probe the early universe (e.g. Bromm & Loeb 2006, and the references therein). However, this may only be achieved if the follow-up observations can be conducted fast and accurately via dedicated instruments like GROND, as discussed in Chapter 2.

The radio afterglow is the latest afterglow emission to start and it is the one that lasts the longest, in some cases up to a few years. About 50% of the well localized GRBs have radio afterglows. The radio afterglows have a typical peak flux around 2 mJy and a non-detection limit of 0.1 mJy. The importance of the radio afterglows is revealed in the phenomenon of scintillation. The flux of the radio afterglow is modulated due to scintillation via the local interstellar medium and permits an indirect measurement of the angular size of the emission.

Most of the afterglow properties mentioned above are derived based on observations of long-soft bursts. Although we do not expect a great difference in the afterglow properties of the short-hard bursts, there had been no afterglow detections for short-hard bursts until Swift started operation. Currently, thanks to the localizations of Swift and HETE-2, there are several short GRBs with X-ray, optical or even radio afterglows. Despite probable differences of the progenitors of the long and short duration GRBs, the X-ray afterglows, which happens to be the most common and well studied afterglow emission range, of both subclasses exhibit a very similar behavior.

1.1.3 Fireball Model

The canonical model for the prompt and afterglow emission is the so-called “fireball model”. The fireball model explains all observational properties of the prompt and afterglow emission of GRBs, independent of the nature of the GRB progenitor. It explains the resultant stage after the GRB progenitor forms a central engine producing the burst. The fireball model assumes the existence of basic ingredients, i.e. a compact object as the central engine and a relativistic outflow of plasma “fireball” that it produces.

Although the details of the model varies yielding several different models (Paczynski & Rhoads 1993; Mészáros & Rees 1997; Sari & Piran 1997; Wijers et al. 1997; Waxman 1997), there are common ingredients involved in all of them. First of all, in all models the central engine that powers the emission is a compact object. The central engine cannot be observed directly because of the very high opacity, however, it can be constrained by the observational facts. To explain the release of a huge amount of energy on the order of 10^{52} erg within an interval of seconds, we need the involvement of a compact object.

¹see also <http://www.mpe.mpg.de/jcg/grbgen.html>

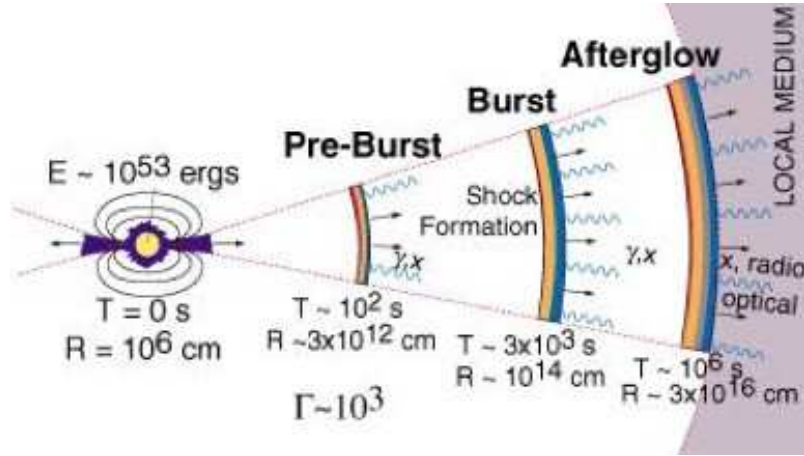


Figure 1.3: An illustration of the fireball emission and shocks.

The released energy amount is very similar to that of supernovae, and in fact there is no known source other than a compact object that can release those energies in such short timescales.

The second main common point in the fireball models is that the γ -rays are produced as a result of dissipation in the relativistic ejecta of a plasma fireball. The energy released during the formation of the compact object is converted into the kinetic energy of thin baryonic shells which expand collimated at ultra-relativistic speed as a jet like structure. The collimated ejecta are usually believed to have Lorentz factors $\Gamma \sim 100 - 1000$. The γ -rays are produced as a result of “internal shocks”, caused possibly by plasma instabilities, between the thin shells within the ejecta itself.

When the relativistic outflow meets with the circumburst medium, “external shocks” take place between the outflow and the medium. The expanding blast wave soon approaches a self-similar behavior where the Lorentz factor decreases with the expansion as $\Gamma \propto r^{-3/2}$. The shock continuously heats fresh gas and accelerates relativistic electrons. The internal/external shock mechanism explains the observed non-thermal prompt and afterglow spectra, as the emission is the Synchrotron emission of relativistic electrons accelerated within the shocks.

The synchrotron spectrum, as shown in Figure 1.4, is described by a peak flux and three characteristic frequencies, namely the synchrotron self-absorption frequency, the frequency at which the electron energy distribution is at its minimum, and the cooling frequency of the electrons that cool on the dynamic timescale. The peak flux and these three frequencies can be formalized in terms of the energy of the fireball, the density of the surrounding medium, the fractional energy densities in electrons and in the magnetic field, the slope of the electron energy distribution and the jet opening angle. Therefore the properties of the fireball and the surrounding medium can be deduced based on the spectra and the light curve of the GRB afterglow.

As the external shock is formed, a reverse shock is also produced, moving back into the

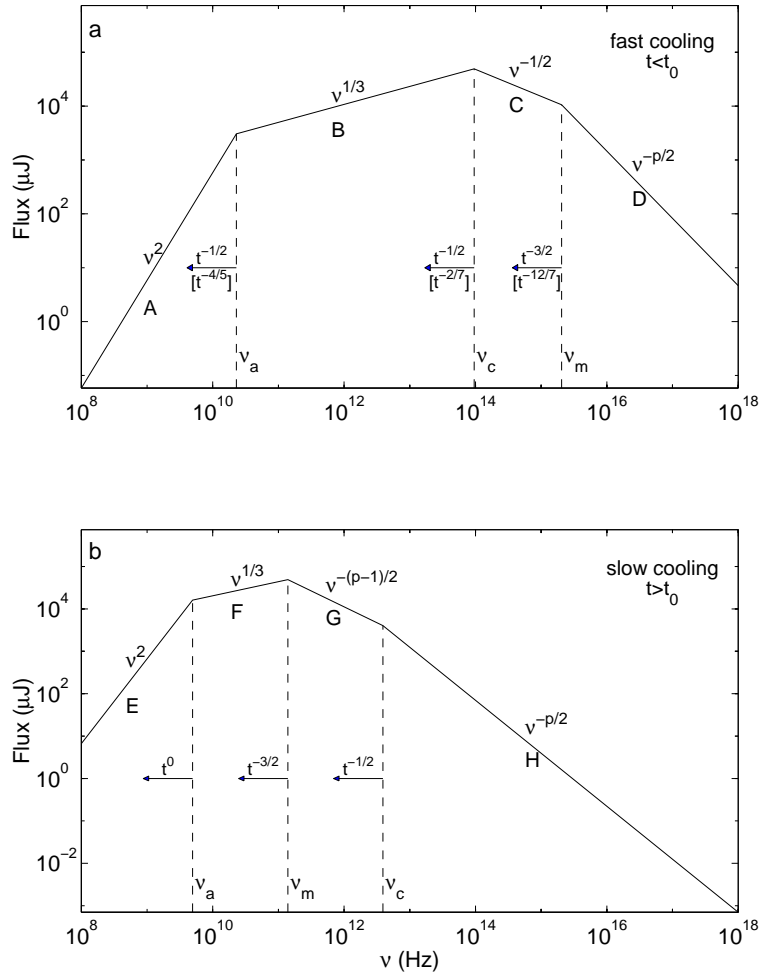


Figure 1.4: Fast cooling and slow cooling synchrotron spectra (Sari et al. 1998).

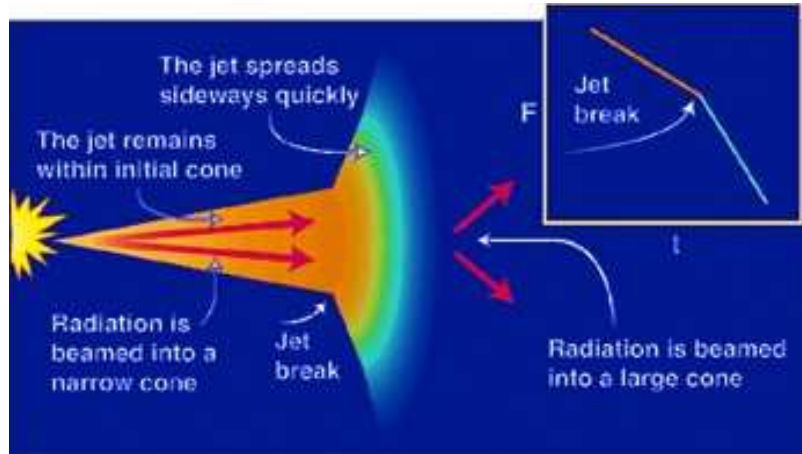


Figure 1.5: The jet break illustration from Piran 2002.

ejecta. This reverse shock may produce a very bright optical flash within a minute, or a radio flare about a day after the prompt event. Both an optical flash and a radio flare was observed in the case of GRB 990123. The flares due to the reverse shock decay rapidly and the forward shock dominates the emission.

As indicated by the achromatic breaks in many afterglow lightcurves, GRBs are beamed in the fireball model. There are several models for the structure of the jet. The two main jet models are the uniform jet model and the structured jet model. In the uniform jet model, the jet has a uniform energy and Lorentz factor inside the opening angle. Due to relativistic effects, the observer sees only part of the jet within an angle $1/\Gamma$ which defines the light cone within which the points are causally connected. As long as $\Gamma > 1/\theta$, where θ is the jet opening angle, all of the radiation is observed by an observer along the line of sight. However, as the jet decelerates, Γ becomes smaller than $1/\theta$, therefore the beaming angle of the radiation becomes smaller than the original jet opening angle. As a result the observed flux reduces, at the point $\Gamma < 1/\theta$. For the structured jet model, however, the energy of the jet varies with the angle. Nonetheless, structured jet models also suggest beamed radiation from GRBs and can account for achromatic breaks.

1.1.4 Host Galaxies

For nearly all well-localized GRBs an underlying host galaxy has been detected, after the decay of the afterglow. This association was only possible for long-soft GRBs until very recently. With the prompt response of Swift, localization of the short duration GRBs is now possible, leading to the detection of host galaxies also for this subclass of GRBs. As the possible origin of the two subclasses are claimed to be different, I will discuss the properties of their host galaxies separately.

The sample of GRB host galaxies differs from a normal sample of galaxies as it is neither flux nor volume limited. The hosts are selected solely by the localization of the GRB after-

glow. The very bright prompt gamma-ray emission is not affected by gas/dust absorption allowing the detection of GRBs independent of the distance and location. With fast and accurate follow-up observations of the bright early afterglow emission, via dedicated instruments like GROND, we may be able to localize the host galaxy which would probably be missed otherwise by optical/IR high-redshift galaxy surveys. The study of the known sample is crucial for our understanding of the general properties of GRB hosts, in view of future observations of hosts at very high redshifts.

The current sample of long duration GRB host galaxies has ~ 80 members spanning a redshift range of $0.0085 - 6.3$ (Fynbo et al. 2000; Berger et al. 2006). They span a very wide range in apparent magnitudes with $R \sim 22 - 30$ mag. A comparison between the core collapse supernova hosts and GRB hosts conducted by Fruchter et al. (2006) led to the conclusion that long duration GRBs are associated with the most massive stars and may be restricted to galaxies of limited chemical evolution. Statistical studies were applied on ~ 40 hosts leading to the conclusion that they are mostly disk galaxies with a median scale length of ~ 1.7 kpc, with a significant fraction of merging and interacting systems (Conselice et al. 2005; Wainwright et al. 2005). These studies are based mostly on the single band data covering the rest-frame blue or ultraviolet wavelength domain at the resolution of HST-WFPC2/ACS. This single band dependency may lead to misleading results as illustrated in the case of GRB 011121, in Chapter 3.

Accurate studies of the morphology, stellar populations, SFRs, and masses of GRB host galaxies are obviously ideally conducted at low redshift, given the better S/N and angular resolution. Imaging and spectroscopy of the hosts of the 3 closest long duration GRBs ($0.0085 < z < 0.168$) has yielded estimates of the fundamental characteristics (luminosities, ages, intrinsic extinction, SFR, metallicity) of those galaxies and has proven that detailed host investigation provides important information on the close environment of the GRB explosion site (Sollerman et al. 2005).

In general, the faintness of the GRB host galaxies represents a limit for good S/N spectroscopy. Broad-band spectral energy distributions (SEDs) are effective substitutes of spectra for determining the galaxy properties, such as, e.g., the SFR. Complementary imaging in K band for 10 long duration GRB host galaxies at $0.5 < z < 1.5$ reveals that these systems are sub-luminous (and, thus, dwarf), blue (i.e. with $R - K \sim 2.5$ mag) galaxies (Le Floch et al. 2003). Analysis of the optical/near-IR SEDs of 11 GRB host galaxies revealed that the majority are best fitted with starburst galaxy templates (Sokolov et al. 2001) or with a burst-type galaxy template (Gorosabel et al. 2003a,b; Christensen et al. 2004a; Bolzonella et al. 2000). In general, long duration GRB host galaxies are thought to be possibly in a starburst phase, independent of the maximum age of their stellar populations. This holds for the most distant GRB host galaxy as well. The SED analysis, together with the optical faintness and colours led to the conclusion that the long duration GRBs with a detected afterglow predominantly trace unobscured starbursts in subluminescent blue galaxies.

Recent studies conclude that the specific star formation rate (SSFR), i.e the SFR per unit stellar mass, is particularly high for GRB host galaxies, indicating that they are

among the most efficiently star-forming objects in the universe (Christensen et al. 2004a,b; Gorosabel et al. 2005). This is also concluded from numerical simulations of large-scale structure formation (Courty et al. 2004). However, there is no general consensus on the amount of attenuation by internal dust suffered by the best studied long duration GRB host galaxies at $0.5 < z < 1.5$ (Sokolov et al. 2001; Le Floch et al. 2003). If this reflects an uncertain determination of dust attenuation, the determination of the SFR is strongly affected (Berger et al. 2006). Interestingly, the first stringent constraints on the dust properties in the circumburst medium of a GRB afterglow revealed dust depletion patterns similar to the Milky Way one (Savaglio & Fall 2004).

Using the SED instead of spectroscopy to determine the galaxy properties requires interpreting observed broad-band SEDs in terms of age and metallicity of the stellar populations as well as of the opacity of the dusty interstellar medium in a robust way. Therefore, different sets of composite stellar population models coupled to models of radiative transfer of the stellar and scattered radiation through different dusty media need to be considered and evaluated statistically. By doing so, structural and geometrical effects may be better taken into account, as well as physical effects like self-enrichment of the stellar populations and dust attenuation. This has been illustrated in Chapter 3 in the case of GRB 011121, which is the first application of this method to a GRB host galaxy.

For the short duration GRBs, 6 host galaxies (out of 10 short GRBs detected during Swift era) were detected by the end of 2005. Four of these are elliptical galaxies, one is a nearby irregular galaxy and one is a star-forming galaxy (e.g. Gehrels et al. 2005; Fox et al. 2005; Prochaska et al. 2006). As opposed to the hosts of long duration GRBs, short duration GRBs have mostly early-type, i.e. elliptical, hosts with almost no star-formation. This indicates that the progenitors of the short duration GRBs are different from those of long duration GRBs, as will be discussed in more detail in the next section.

1.1.5 Progenitors

The prompt and afterglow emission of GRBs can be explained by the Fireball model. However, the Fireball model does not tell us about the nature of the progenitor of GRBs. There are several models that suggest different progenitors and mechanisms to form GRBs, however, two of them have the strongest support from the observations and may lead to the conditions of the fireball model. These are, the collapsar model which is the favored explanation for the long duration GRB progenitors (Woosley 1993), and the merger model which is the favored explanation for the short duration GRB progenitors (e.g. Janka et al. 1999).

In the collapsar model, the iron core of a rapidly rotating massive star ($M > 30M_{\odot}$) collapses to a black hole either directly, or during the accretion phase that follows the core collapse. An accretion disk, of about $0.1 M_{\odot}$, forms around the black hole together with a funnel along the rotation axis of the black hole. Accretion of the disk onto the black hole occurs within several tens of seconds and powers the GRB. This energy is then preferably ejected along the rotation axis producing a jet with opening angle of $\theta < 20$ degrees. For

the production of the prompt γ -rays and the afterglow, the jet should penetrate the stellar envelope.

For four GRBs, the connection between the GRB and the death of a massive star has been proven unambiguously by the detection of a Type Ib/c supernova underlying the GRB afterglow (Galama et al. 1998; Hjorth et al. 2003; Matheson et al. 2003; Stanek et al. 2003; Malesani et al. 2004; Mirabal et al. 2006; Pian et al. 2006). Other indicators for the GRB and massive star connection are the signatures of Wolf-Rayet stars in the spectra of GRB host galaxies like high-velocity absorption lines (Mirabal et al. 2003), the blue colors of the host galaxies (Le Floch et al. 2003), and the projected offsets between the locations of GRBs and the centers of their host that suggest a connection of GRB locations with the host UV light (Bloom et al. 2002a).

Further observational evidence on the nature of the progenitor may be obtained through studies of emission and absorption lines in the GRB afterglow and host galaxy spectra. Wolf-Rayet (WR) stars are the preferred progenitors of long-duration GRBs, since they are massive and they are expected to give rise to hydrogen-deficit supernova explosion (SNe) that is type Ibc SNe. WR stars have a short life-time meaning that they should reside in dense star-forming regions. Furthermore they have strong winds throughout their lives and therefore they are expected to have a dense circumstellar environment. WR simulations show that the WR stellar winds interact with the interstellar medium (ISM) resulting in a complex circumstellar environment as shown in Figure 1.6 (Eldridge et al. 2006; Fryer et al. 2006). The shell in Figure 1.6 is formed by the termination shock and its density and radial extent depend both on the progenitor characteristics (i.e. mass loss rate, wind velocity) and on the density of the medium (e.g. Fryer et al. 2006). With high resolution spectroscopy, it is possible to study the population ratios of excited ions and the chemical composition of the ISM and more importantly the circumburst medium. The circumburst medium can provide us important clues about the nature of the GRB progenitor. In Chapter 2, I present a study of the GRB environment based on the emission lines of a GRB host galaxy.

In general, the condition for the collapsar model is the existence of a rapidly rotating massive core star that removed its hydrogen envelope. Although it looks simple, it was difficult to form an evolutionary path for a single star that would lead to this condition. Recently, there have been identifications of such single star models (Yoon & Langer 2005; Woosley & Heger 2006). However, these new models need a low metallicity progenitor. This is supported by a recent discovery that gamma-ray bursts and supernovae are not found in similar environments and thus, it is proposed that long duration GRBs are associated with the most massive stars and may be restricted to galaxies of limited chemical evolution (Fruchter et al. 2006).

The model that is favored to account for the short GRBs, is the merger model. Neutron star binaries or neutron star - black hole binaries merge to produce a black hole and an accretion disk system leading to the fireball model. The merging takes place as a result of the decay of the binary orbit due to gravitational radiation as demonstrated in the case of the binary pulsar PSR 1913+16. As a result of the merging, an energy of $\sim 10^{53}$ erg

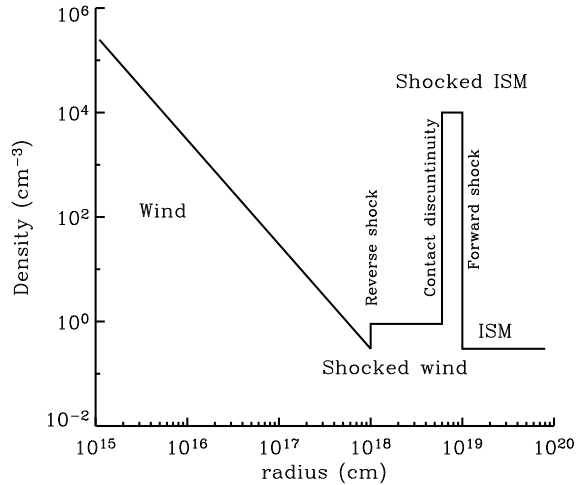


Figure 1.6: A representation of the density profile of circumstellar environments of Wolf-Rayet-like stars (Lazzati 2005).

is released, mostly in the form of neutrinos and gravitational waves. Nonetheless, there is still enough energy to power a GRB.

The merger model can account for the very short time variability of short duration bursts naturally via the intrinsic timescale of the merging event. Furthermore, the lifetime of the binary mergers are usually long ($\sim 10^8$ years) and thus they are expected to occur either in non-star forming galaxies or in regions where the star-formation is not going on. Hence, the evidence of an association between most of the short GRBs are associated and non star-forming galaxies supports the merger scenario. Note however that there are other calculations for merger lifetimes that yield values of the order of 10^5 years.

The collapsar model is the generally accepted model to explain the long duration GRB progenitors, whereas the merger model is favored for the short duration GRBs. Nevertheless, there are certain collapsar models that claim to account also for short GRBs (e.g. Zhang et al. 2003), and similarly certain merger models having the same claim for long GRBs (e.g. Fryer et al. 1999).

1.2 High Redshift GRBs

1.2.1 The motivation

GRBs are in principle detectable up to very high redshifts ($z \lesssim 15 - 20$) without being affected by dust extinction, hence they help localizing their host galaxies, facilitating deep searches and observations of the host galaxies. Therefore, GRBs can lead us to the first

galaxies in the Universe, and also shed light onto the cosmic re-ionization era and the star-formation history of the Universe.

There are two major theories of galaxy evolution, monolithic collapse and the hierarchical merging scenario. According to the monolithic collapse model, galaxy formation occurs in one large burst of star formation, followed by passive galaxy evolution, as the stars slowly age. In contrast, the hierarchical merging scenario describes galaxy formation as a slower process, where large galaxies are created by numerous mergers of smaller objects. The latter model tends to produce more star formation at later times. The star formation rate density as a function of redshift can distinguish between these two models by showing us when most of the stars in the universe were made.

Various different measurements of SFR history have been made at different redshift ranges up to $\lesssim 6$ using the Lyman-break drop-out technique (Lilly et al. 1996; Madau et al. 1996; Giavalisco et al. 2004; Bunker et al. 2004; Bouwens et al. 2004). Most of these studies yield that the dust uncorrected SFR increases from redshift $z=0$ to $z=1$, and stays constant up to redshift $z=4$ from which it starts to decline. These results are based on the estimate that for a given initial mass function (IMF), the total UV galaxy luminosity density is proportional to the instantaneous SFR (Madau et al. 1996, 1998). However, this is affected by the uncertainties in the dust correction especially at high redshifts (e.g. Hopkins et al. 2001). Moreover, there are other limitations in the determination of the SFR history. High-redshift studies are small in number because of the technical difficulties, i.e. huge exposure times with large telescopes to do both deep and large area surveys. Combining different small fields, on the other hand, introduces large Poissonian fluctuations and field to field variations. Furthermore, the surveys are magnitude limited in the optical and also selection by dropouts possibly limits the type of the galaxies included in the survey. GRBs offer a very nice alternative to the high-redshift surveys to study the SFR history and even possibly the first galaxies.

High-redshift objects are also interesting in terms of studying the cosmic re-ionization. Observations of quasars show that the neutral hydrogen in the IGM became fully ionized by $z \sim 6$ (Fan et al. 2004; Spergel et al. 2006). In the standard picture, this re-ionization was the result of a rapid rise in the production of hydrogen-ionizing photons due to the birth of the first sizable population of stars and accreting black holes. However, neither the exact type of ionizing source (e.g. AGN only make a negligible contribution to the ionizing flux at $z \sim 6$; Willott et al. (2005)) nor the epoch of re-ionization (anything between redshift 6 and 20–50 has been proposed) are constrained any further. GRBs can be used to constrain the epoch of re-ionization more advantageously than QSOs. First of all, it is not easy to find QSOs at $z > 6.5$ since the characteristic quasar luminosity declines sharply with increasing z (Wyithe & Loeb 2002), whereas GRB afterglows decrease in brightness only mildly with z due to cosmic time dilation and favorable K-correction. In addition, their intrinsic power-law spectra make it straightforward to delineate the shape of the Ly α line and/or find metal absorption lines.

1.2.2 Present Strategies

The present strategy of GRB follow-up observations all around the world involves multiple steps. In order to do detailed science with GRBs, as described in the previous chapters, one needs to conduct high-resolution spectroscopy in most cases. However, without knowing the redshift of the GRB it is not possible to select the optimum instrument and grism for doing spectroscopy. The higher the redshift of the GRB, the tighter gets the selection due to relativistic length contraction effects. Therefore, at least an initial guess of the redshift is necessary. This is currently obtained using the photometry information from different telescopes.

There are a few very small robotic telescopes, and several other small telescopes utilized by GRB observers around the world to follow-up GRB afterglows automatically. These telescopes usually observe the GRB afterglow in one filter at a time. However, observations in more than two filter bands are necessary even to roughly estimate the redshift of the GRB. There are currently 4 instrument systems in the world that can conduct simultaneous observations in more than one filter. These are PROMPT, SMARTS CTIO 1.3m, TRISPEC and SIRIUS. PROMPT is a system that consists of six 0.41-meter telescopes located at North Carolina, USA (Reichart et al. 2005). Each telescope is optimized for a different wavelength range and conducts single filter observation simultaneously with other five telescopes. Similar to GROND, the primary science goal of PROMPT is to conduct GRB follow-up observations. The CTIO 1.3-meter telescope, operated by the SMARTS consortium, holds a 2 channel instrument called ANDICAM that can conduct simultaneous observations in 2 wavelength bands, one being optical (one of U, B, V, R, I) and the other near-infrared (one of Y, J, H, K) (DePoy et al. 2003). TRISPEC is capable of conducting simultaneous observations in 3 bands either as imaging or spectroscopy, together with polarimetry if wanted, in either mode (Watanabe et al. 2005). However, it is not permanently mounted on one telescope, instead used as a visitor instrument at several telescopes. SIRIUS is a 3-channel imaging instrument mounted on IRSF 1.4-meter telescope at South Africa (Nagayama et al. 2003). It is dedicated for specialized surveys of the southern hemisphere sky. Note that among the current systems capable of simultaneous multi-band observations, only GROND and PROMPT are dedicated for GRB follow-up observations.

Photometric Redshift

The usual technique to determine the redshift is to search for the redshifted Lyman limit ($\lambda=912\text{\AA}$) or Lyman-alpha absorption ($\lambda=1216\text{\AA}$). To be able to detect the Lyman limit, first the spectral energy distribution (SED) of the afterglow should be constructed. To construct the SED using single band observations, one needs to extrapolate the observed brightnesses, which were obtained by different instruments at different times, to the same point in time. This requires knowledge about the lightcurve of the GRB afterglow for the extrapolated filter bands. For example, the afterglow SED of GRB 050904 ($z = 6.3$) was constructed by calculating the magnitudes at a common epoch of 1.55 days

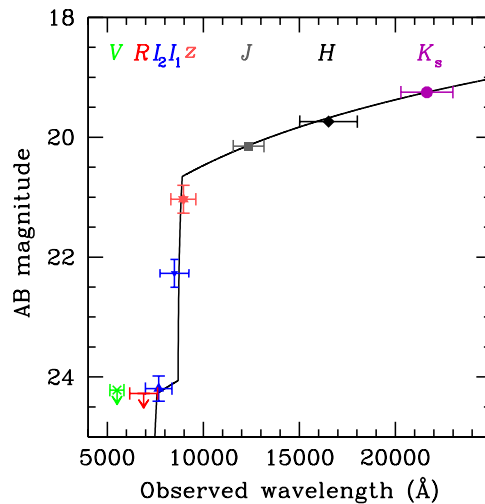


Figure 1.7: The SED of the afterglow of GRB 050904 (Tagliaferri et al. 2005). The magnitudes were interpolated to the same epoch using the measured decay of the afterglow light curve, and they are corrected for Galactic extinction. The solid line is the best fit model.

after the burst, using the measured decay of the afterglow light curve (citettag, see also Fig. 1.7). Therefore, it is more advantageous to use detectors which are able to conduct simultaneous multiple band photometry. GROND was designed and built such that it can do simultaneous observations in 7 wavelength bands. To observe the afterglow in 7 filters simultaneously is necessary to determine the redshift of the GRB in a rapid and firm way. Those 7 bands are chosen specifically to be tuned to high-redshifts. The GROND SED includes the Lyman limit break as long as the GRB has a redshift between $z \sim 3 - 13$.

1.2.3 A new instrument: GROND

GROND is an instrument designed and built at MPE with contributions from Landessternwarte Tautenburg. Its aim is to conduct rapid follow-up observations of GRBs which would serve for several scientific studies: i) rapidly determining the photometric redshift of the GRB, ii) studying the afterglow properties, iii) studying the properties of the jet via possible observations of the jet break and cooling frequency.

GROND is composed of 7 detectors each associated with a different wavelength band allowing observations in 7 bands simultaneously. Four of these detectors are optical CCDs of type E2V 42-40, covering $\sim 400 - 1000$ nm. The other three are HAWAII infrared detectors equipped with J, H and K filters covering $\sim 1100 - 2350$ nm. Therefore it covers the Lyman-limit or the Lyman- α absorption features, which are necessary for photometric redshift determination, for a redshift range of $z \sim 3 - 13$.

The design of the instrument was challenging due to three issues: i) different temperature

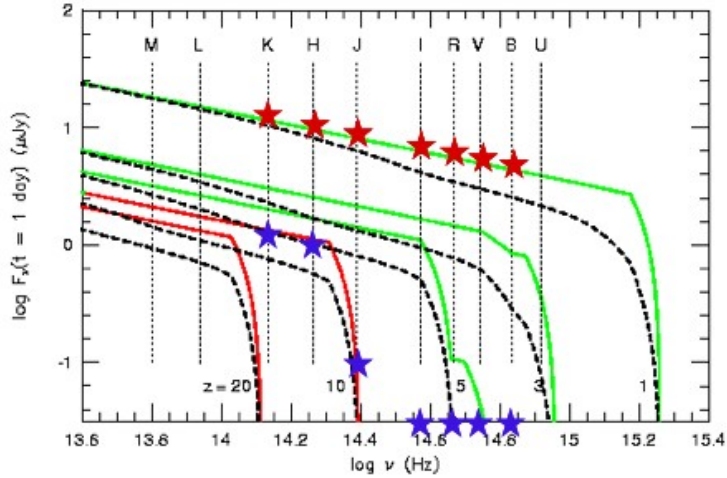


Figure 1.8: The redshifting of Lyman-limit break and Lyman- α absorption features of a power-law spectrum, i.e. spectrum of a GRB afterglow. The red stars represent the fluxes of a GRB afterglow at $z = 1$, and blue stars are those of a hypothetical GRB afterglow at $z = 10$. The solid curves are the model power-law spectra of the GRB afterglow at different redshifts, and the dashed curves are the same with an addition of extinction of $A_V = 1$ mag.

requirements of optical and infrared detectors in order to be operated, ii) operating CCD shutter in cold, and iii) dithering of infrared images. The optical CCDs have to operate above 155 K (ideally around 175 K), and the infrared detectors have to be operated below 80 K (ideally around 65 K) to optimally reduce the noise. The rest of the components of the instrument, such as the motors, are designed to be operated at 80 K. To provide the operation temperature of all the detectors and to lower the noise, the instrument sits in a cylindrical cryogenic vacuum vessel. The structure of the instrument is shown in Figure 1.9. On one side of the vessel, there is the entrance window, and a separate pick-off mirror for the independent guiding system. On the other side, there is the connection to the closed cycle cooler which is mounted outside the vessel. There are two benches inside the vessel; one hosts the optical detectors and the other hosts the IR detectors. The mechanical construction is designed such that it is stable at all possible orientations of the telescope.

The light coming from the entrance window is first split into three beams using two dichroics. The first dichroic reflects the wavelength range 398 – 687 nm, which is then split into g (398 – 538) and r (538 – 687) bands using another dichroic and reaches two of the optical CCDs. The light that passed through the first dichroic meets with a second dichroic which reflects the wavelength range 687 – 947 nm, which is split into i (687 – 817) and z (817 – 974) bands again using another dichroic and reaches to the remaining two optical CCDs. The way that the light is split, is illustrated in Figure 1.10. The resultant

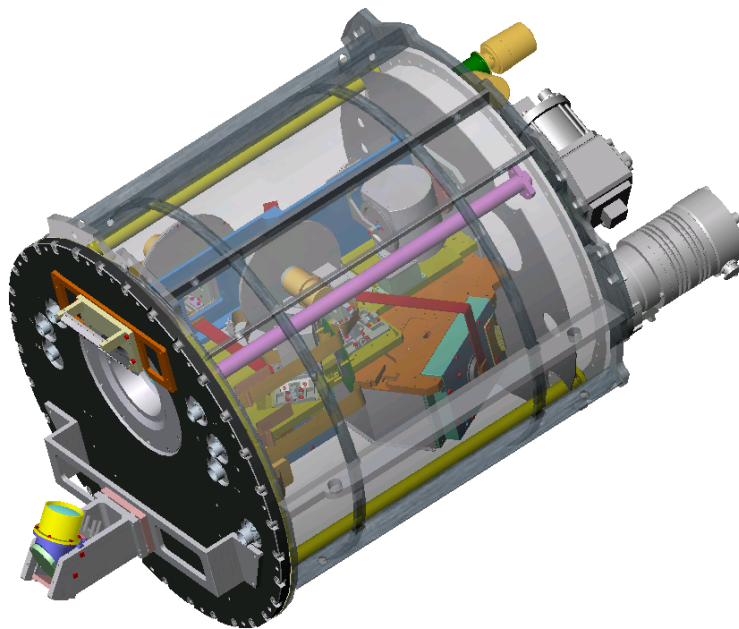


Figure 1.9: Drawing of the GROND vessel where the optical bench is on the top side and the optical part is visible.

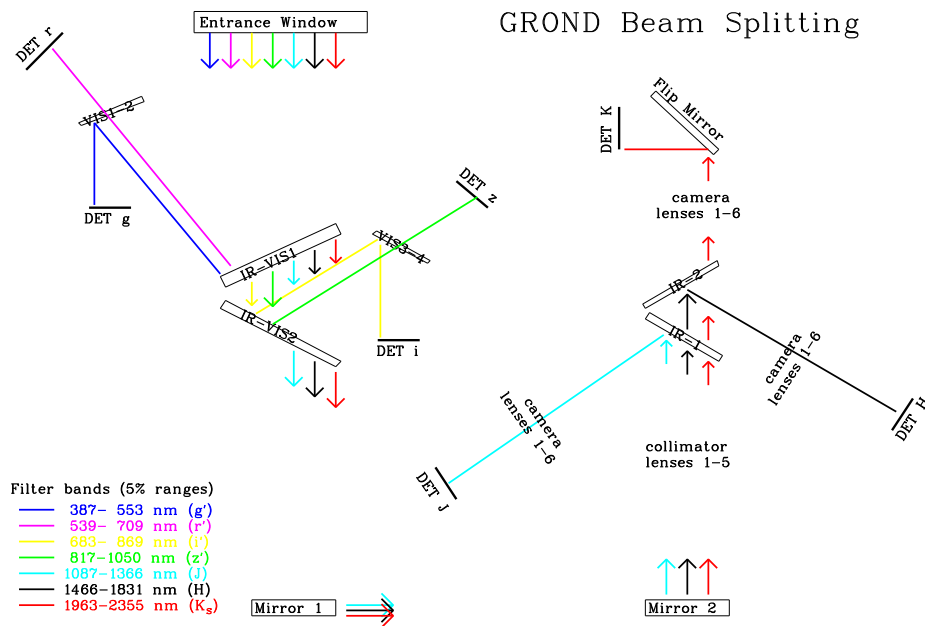


Figure 1.10: Schematic representation of how the light is split to the optical and infrared detectors of GROND.

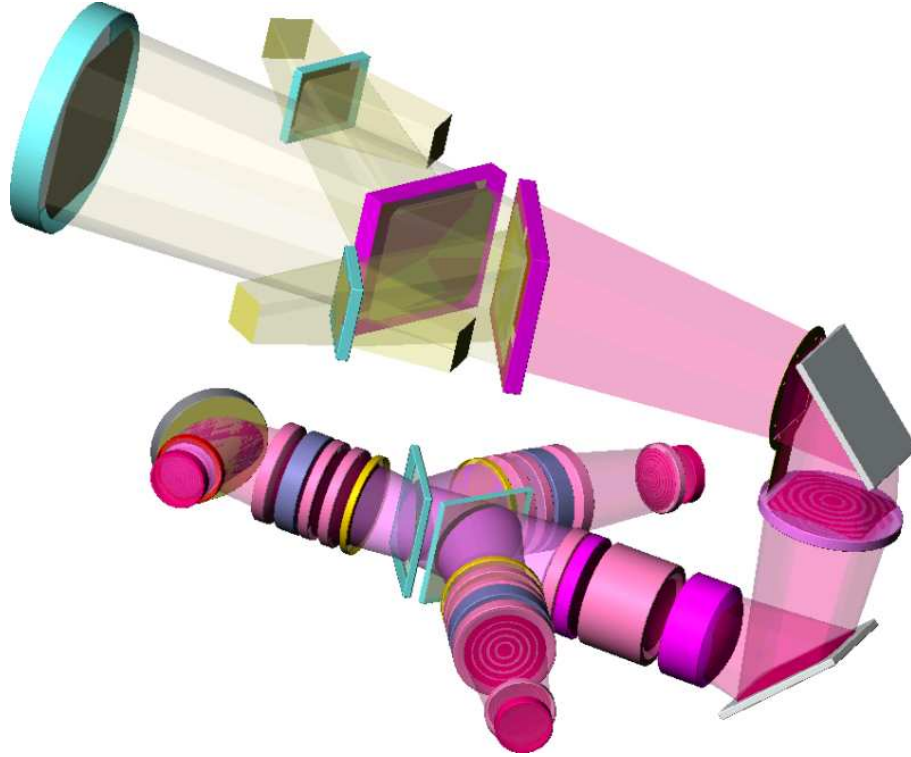


Figure 1.11: The optical elements of GROND. The light comes from the blue entrance window shown at the leftmost side, and is split to the four optical CCDs via two large dichroics (*violet*) and two smaller dichroics (*blue*). The rest of the light that passes through both of the large dichroics is folded to the infrared side using two folding mirrors (*grey*) shown at the rightmost side. After reaching the infrared side, the light is collimated by a set of lenses, and then split by two dichroics (*blue*) into three beams. These three beams are again collimated by groups of lenses located between the dichroics and the infrared detectors.

wavelength bands correspond to that of the filters used for the Sloan Digital Sky Survey². The rest of the light that passed also through the second dichroic is folded to the infrared bench with the help of two mirrors, one on the optical and the other on the infrared bench. The infrared part has a more complicated design to establish a large field of view for the small infrared detectors. The optical CCDs have a field of view of 5.4×5.4 arcminutes projected on 2048×2048 pixels each $13.5 \mu\text{m}$ in size. The infrared detectors however, have 1024×1024 pixels of each $18.5 \mu\text{m}$ in size. The aim is to cover a field of view of $\sim 10 \times 10$ arcminutes, which corresponds roughly to the pre-launch prediction of the GRB position error box of Swift BAT detector. In order to do this a focal reducer with 23 lenses was developed (see Fig. 1.11). The light coming from the folding mirror is collimated by a set of 5 lenses. Two dichroics are located in the parallel part of the beam and split the light into three bands: J (1103 – 1350), H (1495 – 1780) and K (2005 – 2320), as shown in Figure 1.10. These split light beams are focused with the help of sets of camera lenses in front of each infrared detector (see Fig. 1.11). Each infrared detector has an associated filter that is designed specifically for GROND, since the commercially available ones have low transmission.

GROND will be commissioned at the MPG/ESO 2.2m telescope at La Silla, Chile. The telescope has two other instruments mounted on it, namely the Wide Field Imager (WFI) and an optical spectrograph FEROS. GROND will be mounted on Coudé-like focus of the telescope. For all the three instruments be operable, an additional mirror (M3 mirror) is designed as a flip mirror that will move and fold the light to GROND instead of WFI or FEROS. When GROND is not conducting any observations the M3 mirror will stay in an upright position and will not be in the field of view of the other instruments.

²<http://www.sdss.org>

2 Probing High Redshift: Automated Photometry with GROND Pipeline

2.1 The GROND Pipeline

The Grond Pipeline System (GP) is a pipeline system designed and written specifically for GROND. Its prime objective is to conduct rapid GRB afterglow observations and determine the redshift as quickly as possible. All the components of GP will be deployed on a machine which will be located at the site of the telescope.

Rapidity is a key issue in the area of afterglow observations since the brightness of GRB afterglows decay quickly. Furthermore, there are additional time constraints introduced by the Swift satellite. Swift points 90° to the Sun meaning that a Swift-detected GRB is usually observable for only around 3 – 4 hours within the same night at an observatory on Earth. GP has been designed to identify the high redshift GRB afterglows in 1 – 2 hours. This would provide the time necessary to trigger larger telescopes like VLT and to tune high-resolution spectroscopy tuned for the highest signal-to-noise ratio at best spectral resolution, and therefore to maximise the scientific output.

The coordinates of a GRB is distributed to the world through the Gamma-ray bursts Coordinates Network (GCN) in a few seconds (Barthelmy et al. 2000). Therefore GROND should react to GCN notices and observe the provided GRB locations. One then needs to identify the optical/near-IR afterglow of the GRB and determine its redshift by fitting the SED of the afterglow constructed using 7 broadband filters. This whole process, starting from receiving the alerts and triggering the observations, and final determination of the afterglow redshift, is to be done automatically without human intervention, at the telescope-site via specially developed software (GP).

There is no other instrument like GROND that can observe in 7 filters simultaneously. This uniqueness gives us the opportunity to do pioneering science but presents major challenges as well. The observations must be simultaneously analyzed to take real advantage of multi-band simultaneous observations. The originality of GROND therefore necessitates a pioneering automatic data analysis system which is both fast and reliable.

The architecture of the GP is based on an asynchronous framework to provide speed and the degree of freedom necessary to apply different analysis strategies. In the context of the GP system, asynchrony means that the work is distributed among different processes which do not run sequentially but asynchronously. The asynchrony allows several different processes doing independent jobs to be run in parallel, as well as processes that do similar

Table 2.1: The duties of the system and the GRB analysis layers of the GP.

System - Observation Control Layer	GRB Analysis Layer
Receiving GRB alerts	Pre-processing the images
Deciding whether to observe the target	Photometric analysis of 7 band data
Calculating visibility of the target	Constructing the SED of the objects
Scheduling of the observations	Identifying the GRB afterglow
Triggering/continuing/stopping observations	Determining the photometric redshift
Providing web-interface for user interaction	Evaluating the accuracy of the redshift

jobs. In this way it speeds up the processing and analysis, and provides the opportunity to introduce any number of processes that run in parallel. Note however, that it is much more difficult to design and control an asynchronous system than a system that runs sequentially.

The GP mainly consists of two layers, the system layer and the GRB analysis layer (see Tab. 2.1). The system layer consists of the processes that receive the GRB alerts, decide whether to follow that burst or not, schedule and re-schedule observations and conduct the observations by initiating, continuing, interrupting or ending them. Furthermore, the main system process controls all processes including the analysis processes, and coordinates the interprocess communication which is realised via non-blocking socket channels using a well-defined messaging protocol¹.

The GRB analysis layer contains pre-processing of the images, photometric analysis, identifying the GRB afterglow, spectral energy distribution (SED) analysis and photometric redshift determination.

The system stores its state and all the results in a database using `pysqlite`² which is an interface for `SQLite`³ embedded relational database engine. `SQLite` is preferred because it is an embeddable, fast and easy to use database without any configuration or any need for administration. The database is not only used for storage but also some of the calculations and tests are done directly on the database as SQL queries. The database design of the GP system is based on relational database in which a database is a collection of relational tables. A relational table is composed of a set of named columns and an arbitrary number of unnamed rows, and a relationship is an association between two or more tables. Relational tables are like sets and hence set operations can be performed on them, i.e. it is possible to take the intersection of two tables, etc. Relational database model is a very effective and widely used database model.

The GP system is mainly designed to work automatically without any need for human interaction. Nevertheless, it still allows its authorized users to interact with the system in two ways: through a web interface and through a command shell. The command shell

¹see ESO Grond Pipeline document v1.0 for details.

²<http://www.pysqlite.org/>

³<http://www.sqlite.org/>

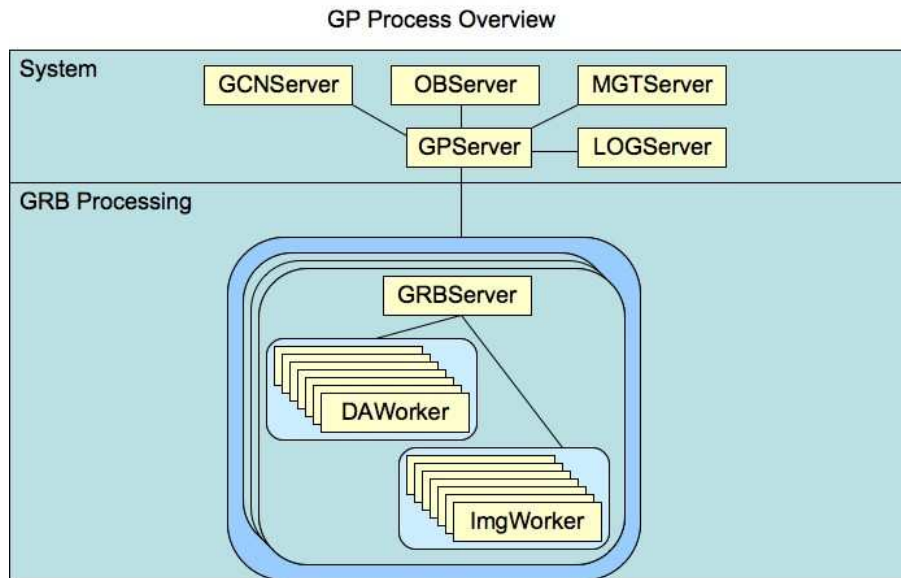


Figure 2.1: An overview of the processes of the GP system. The duties and working principles of the processes are explained in the subsections of this chapter.

interaction is much more restricted than the web interface. It is mainly implemented as a backup option for exceptional cases. The users can only configure the GP system or export its current configuration through shell commands. A much more feature-rich and useful user interaction interface is designed and accesible via the internet. A web server was designed and coded specifically for the system in order to conform to the asynchronous architecture. Through the web interface of the GP, the users can

- i) view the current state of the system and the analysis in differing levels of details
- ii) schedule new observations
- iii) change the already existing schedule
- iv) provide additional position information to be used in the analysis
- v) provide additional position information to re-point the telescope
- vi) configure the system.

The details of the processes are described in the following subsections of this chapter. The approach adopted to describe the system is to focus on the observation and analysis, rather than on the GP system structure itself. The organization of the subsections are such that they describe a sequential order of the events, although, of course this is not necessarily true for the actual processing of the system itself. Nevertheless, the events still happen in a certain sequence enforced by the prerequisites of each task, i.e. identification

of the GRB afterglow requires that the images of an observation block has been acquired, photometrically analysed, calibrated and the objects found in different filter band images are matched with each other.

Please note that the GP system has been designed and written mainly by Abdullah Yoldaş, with contributions to several subprocesses by other authors or publicly available programs mentioned under the relevant subsections. My contribution to the GP system is

- i) designing and coding of the photometric analysis part of the program described under subsection 2.2.6,
- ii) and co-designing the following components of the system:
 - a) database tables,
 - b) GRB follow-up decision mechanism using GCN packets,
 - c) scheduling algorithm,
 - d) analysis strategy for the observation blocks,
 - e) analysis strategy for the photometric redshift determination.

Time-wise, this constituted about 50% of my PhD studies.

2.2 System layer: Observing GRB Afterglows

2.2.1 Receiving GRB Alerts

Information about the detection of a new GRB, as well as various other information about its properties; such as the coordinates and the associated uncertainty, is announced to the world almost immediately via the Gamma-ray burst Coordinate Network (GCN). There are two main methods of distribution for GCN announcements; emails or socket packets. The method used by GP is the socket method, which is the faster option⁴. A process of GP listens to GCN packets all the time and filters the unnecessary ones (i.e. IMALIVE type of packets that are sent every minute by NASA GCN site to check the maintenance of the connection).

When a GRB alert comes, a packet is passed to the main process that controls all other components. The main process extracts all the information from the packet by parsing it according to its type. Part of a socket packet from Swift's BAT detector is illustrated in Figure 2.2. Packets coming from different satellites carry different information, furthermore there are different types of packets coming from the same satellite designed to carry different information (see the caption of Fig. 2.2). The main process decides what to do with the packet in a series of actions designed to optimize the duration and stability of the decision process.

⁴see http://gcn.gsfc.nasa.gov/gcn_describe.html

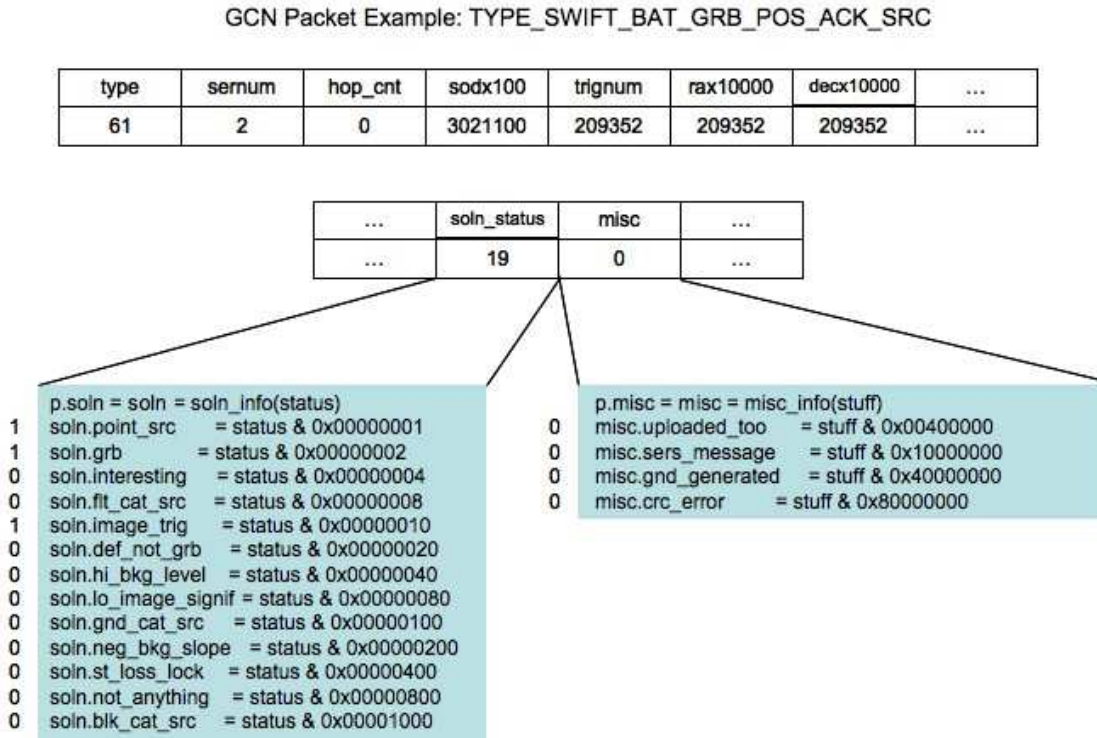


Figure 2.2: An example for a GCN socket packet carrying information from the BAT detector of Swift satellite. This is the main and initial packet that carries the position information of the target as detected by BAT. A GCN packet is composed of 40 long integers illustrated as a box. A long integer is 4 bytes and a byte is 8 bits. Thus, in principle each box carries 32 bits, each of which can hold a different information. For example the information carried by different bits of the soln_status box (one long integer) is shown in the blue box on the left. The soln_status carries the information regarding, i.e. whether the detected object is a point source, whether it is a known source included by the flight or ground catalog used by that satellite, whether this is a retraction of a previous GRB announcement, etc. Similarly some of the information carried by the misc box is shown in the blue box on the right. The misc box carries information regarding, i.e. whether this is a TOO observation, whether this is a ground generated alert, etc. The first long integer (first box) always contains the integer representing the GCN packet type. The other fields may hold different information depending on the packet type. For example, the Swift satellite has 19 different types of GCN packets.

GP first checks whether it is a packet for an existing GRB or it announces a new target for the system. Then the decision tree splits again according to packet types as they carry different information to be evaluated. It first checks whether the packet contains a bogus trigger. A trigger is called bogus, if the satellite sending the alert has lost its tracking and therefore sends totally wrong alerts and coordinates as if a GRB happened, or if the source is marked as “not an astrophysical object”. GP does not continue further if the packet contains a bogus trigger. Next it checks whether it is a retraction or not. In the context of GRB alerts, retraction is a term used to retract a previous trigger claiming existence of a GRB. By definition, under normal circumstances the packet carrying the retraction information should arrive after the packet which announces that object as a GRB. However, GP system checks the retraction information independent of whether the packet is for an existing target or not. This is done in order not to lose the information if a problem happens at the NASA GCN site and the packets are sent in a wrong order. If it is not a retraction, the main process checks certain fields of the packet, i.e. catalog source, point source etc., to decide whether the object can be regarded as a GRB for the system. In other words, the system uses one of the user defined decision rules and decides whether the object should be followed up by GROND. The system decision is therefore expressed as one of the three words: Retraction, Follow, Ignore. At this point the GP system holds three different pieces of information, whether the target is new, whether it is a retraction, and whether it should be followed up or ignored. These are derived using the incoming packet only.

For a new target, the system will act based on this information only when deciding what steps to take (see Fig. 2.3). However, the case is different for an existing target, where the current packet is the second or further packet for a target that has already been announced and entered the system before. In this case the system checks also its previous decision about the target, i.e. retraction, follow, ignore, or null if the target is entered to the system by a user instead of a GCN packet (see Fig. 2.3). Furthermore, it also checks the user decision on the target, if any. Users of the GP system can interact with the system and control the system to a certain degree via web. In this case, a user may mark any target as follow or ignore, which enters to the system as the user decision. If the user does not choose any of these two, the user decision stays null. Users can control the system actions as they can override the system’s decisions. For example, the auto decision (system’s decision based on packet information as explained above) is “follow”, but the user does not want that object to be observed and sets the user decision as “ignore”. In this case the object will not be scheduled for observation even if it is observable. No further GCN packet can change this decision of ignoring the target, but only the user her/himself.

There is one exception to the rule that no auto decision can overcome a user decision. It is allowed by a configurable decision, which is “Retraction overrides user decision”. If this option is in effect, the Retraction auto decision retracts the target regardless of the user decision. In summary, for an existing target, the process decides what to do according to the previous auto decision and user decision, as shown in Table 2.2. The main process acts only if the final decision is changed by the auto decision obtained from

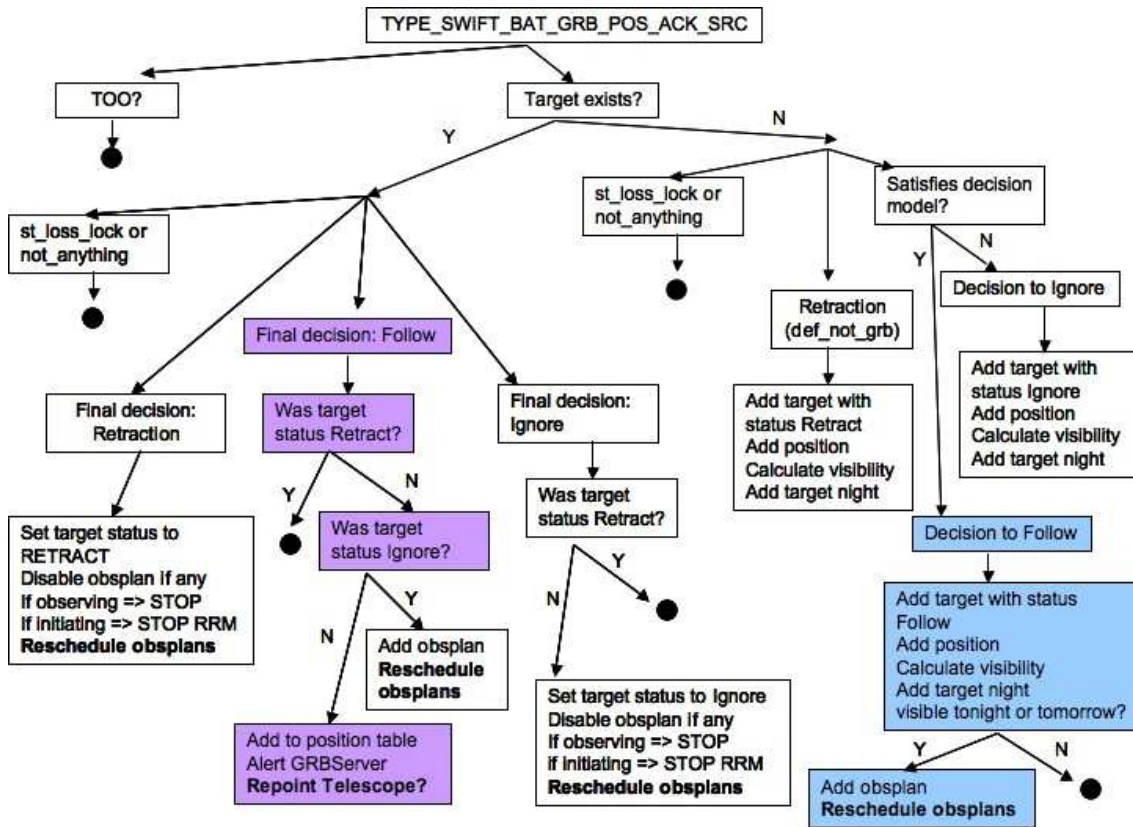


Figure 2.3: An example case illustrating in a simplified way the decision given upon the incoming packet (in this case SWIFT BAT position packet) and a summary of the consecutive actions, i.e. scheduling, starting/stopping observations, re-pointing the telescope, etc. The black dots means that no further action is taken. The light blue boxes show the “standard” track of a new GRB. The violet boxes show the “standard” track of an existing GRB that happens for example if this is the second SWIFT BAT position packet received for the same GRB. The details of how the final decision is taken for an existing target is shown in Table 2.2.

Table 2.2: Decision cases for which the final decision differs from the old decision

Old Final decision	User decision	Auto decision	Final decision
Follow	Follow	Retraction	Follow/Retraction *
Follow	None	Ignore	Ignore
Follow	None	Retraction	Retraction
Ignore	Ignore	Retraction	Ignore/Retraction *
Ignore	None	Follow	Follow
Ignore	None	Retraction	Retraction

* If the “Retraction overrides user decision” option is in effect, final decision is Retraction.

the currently evaluated packet. A change in the final decision necessitates reorganisation of the observation schedule for that night. If the final decision is changed from Follow to Retraction or to Ignore, the main process has to delete the observation plan for the target, if any. If the final decision is changed from Ignore to Follow, the target is scheduled for the night if it is observable. Note that if the previous auto decision is Retraction, it cannot be changed by the system but only by the user.

For a new target, the visibility of the target is calculated independent of the auto decision. The visibility calculations utilize skycalc, a C program written John Thorstensen⁵, with a python wrapper. The visibility of the object is normally calculated for tonight, which is the current night if GRB happens during nighttime in La Silla. The estimated percentage of GRBs that would happen during a La Silla night is about 15%. Otherwise if GRB happens during daytime in La Silla (other 85%), tonight means the upcoming night. However, if the GRB is not visible (totally or anymore) tonight, or if the visibility interval is shorter than the duration of the initial observation configured for the GP system, then the process calculates the object’s visibility for the next night. If it is observable during tonight or next night, meaning that if it has a visibility interval after now (or next night) and longer than a minimum duration and also longer than duration of the initial observation, both configurable by the user, then it is scheduled for observation. Scheduling means that the main process prepares an observation plan of the target, satisfying the above defined criteria, and tries to fit it among the other observation plans, if any. Due to the complexity of the scheduling algorithms they will be described in a separate subsection in more detail (see below).

2.2.2 Scheduling of Observations

The scheduling of observations for GROND is rather complicated since it needs to be fully automated like the other parts of the system, but at the same time it should allow the users to modify, add, and delete the scheduled observations. Furthermore, the automatically

⁵see http://www.eso.org/observing/skycalc_notes.html

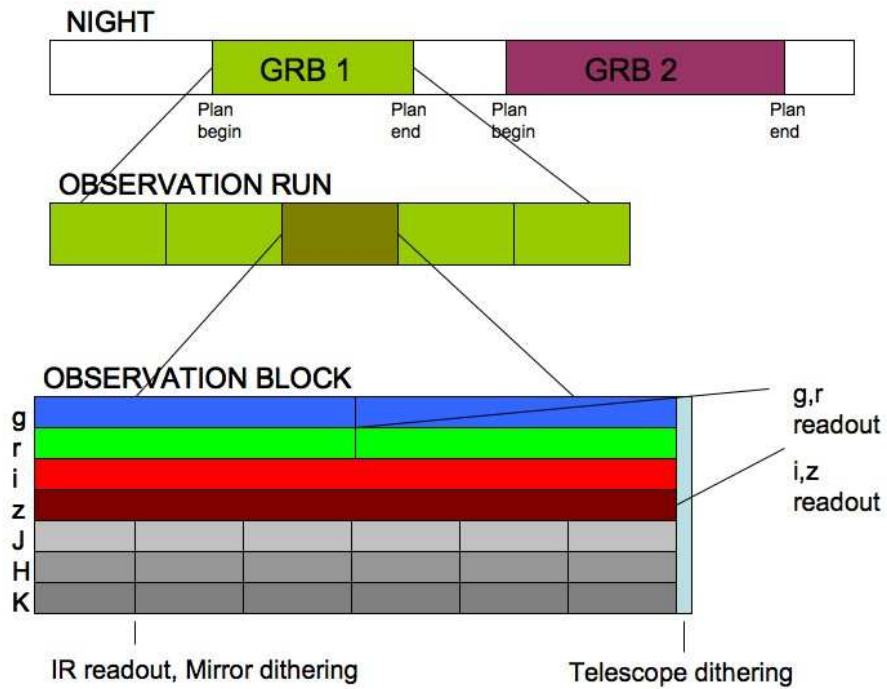


Figure 2.4: Representation of a night, an observation run and an observation block. The green and violet blocks on the night are the observation plans of GRB1 and GRB2, respectively. An observation run is a realised version of an observation plan. Each observation run is composed of a sequence of observation blocks.

Table 2.3: Properties of an Observation Plan

plan-begin	beginning of an observation plan
plan-end	end of an observation plan
allow-begin	beginning of the allowed observable interval
allow-end	end of the allowed observable interval
max-duration	maximum duration allowed for an observation plan
min-duration	minimum duration allowed for an observation plan
priority	priority (in percentage) of an observation

scheduled observations may be deleted by the system also, as a result of “Retraction” or a later “Ignore” decision derived from the GCN packets for that target.

Some of the other robotic or automated telescope systems use “just in time” (*jit*) scheduling which is based on choosing the observation to be conducted instantly at every time rather than scheduling a set of observations for a whole night. *jit* scheduling is not suitable for GROND because i) we would like to observe all GRBs that occur at the same night and that are visible, however *jit* scheduling system does not allow the system to foresee the night and hence to arrange the observation durations accordingly, and ii) we would like the user to be able to interact with and modify the system, however this would be impossible with *jit* scheduling. Therefore, we developed our own scheduling system that fulfils all the requirements of GROND and arrange the schedule for the whole night, and also for the next night depending on the configuration.

The parameters that define an observation plan are as follows: allow-begin, allow-end, plan-begin, plan-end, max-duration, min-duration, and priority (see Tab. 2.3). Plan-begin and plan-end define the actual⁶ beginning and end of the observation plan. In other words it shows the planned interval of observation for that target. By definition, an observation plan consists of a single interval. Any further intervals of planned observation of the same target are regarded as different observation plans. Allow-begin and allow-end define the beginning and end of the allowed time interval for an observation plan. In other words, neither the system, nor the user can modify the planned beginning and end of the observation in such a way that they exceed the allowed beginning and end times for that observation. Allow-begin and -end are constrained by the beginning and end of the visibility interval of that object. In this way, both the system and the users can schedule an observation that does not necessarily cover the whole visibility interval(s). Furthermore, by restricting the allow-begin and -end, the user can prevent possible shifting of the planned beginning and end of the scheduled observation, which may happen when another observation is scheduled or deleted.

Similarly, the min and max duration parameters supply configurable restrictions on the time of the scheduled observations, since the min (max) duration parameter sets the minimum (maximum) duration of the scheduled observation. Last but not least, the

⁶Note that in the context of scheduling, actual does not necessarily mean that it is happening.

priority parameter shows the priority of the observation which is extremely important for the resolution of conflicts between competing observation plans. By definition, at the times when the planned observations need to be re-scheduled, the observation plan with higher priority can partially or totally override another observation plan with lower priority. For GP, the latest burst has the highest priority. However, like all other scheduling parameters, the users can also change this.

These seven observation plan parameters have configurable default values. The GP system normally applies these configured values to all of the observations it schedules. However, after scheduling, those parameters are assigned as a part of that individual observation and therefore they can be modified by the users. In this way, the system gives the users maximum degree of freedom, and at the same time it is still able to schedule automatically.

For scheduling different intervals, we need to conduct interval algebra. Abdullah Yoldaş wrote a library for interval algebra developed based on Allen’s interval algebra (Allen 1983; Drakengren & Jonsson 1997), which involves set operations applicable on intervals.

There are two modes of scheduling: *lazy* and *smart*. The *lazy* mode is named so because it does not expand the length of observation plans. It works on the planned beginning and end times of all the observations and tries to schedule them accordingly. It shifts them only within their previously planned interval. It means that, for the *lazy* mode, once a modification is made on the begin and end times of an observation plan, it cannot be taken back. For example, if a plan, eg. plan A, is partially or totally covered by a higher priority plan, plan B; in the *lazy* mode the system does not try to shift plan A to another location within the allowed observable interval. Hence plan A is disabled if it is totally covered by plan B, or shortened if it is partially covered. In the *lazy* mode, the length of plan A cannot be expanded even if at a later time plan B is deleted or disabled.

Note however that, if at the time of scheduling, the starting time (plan-begin) of an observation plan has passed and the end time (plan-end) is not reached yet, it means that the plan is active; in other words, it is either being observed or initiated. For the *lazy* mode, in the cases of observation and initiation, the observation plan cannot be treated as if not started, and hence modifications are allowed only if they are a continuation of the currently active plan. So the only allowed case, for observing or initiating plans, is contracting the length of the observation plan.

An example case of the *lazy* mode scheduling is illustrated in Figure 2.5. In this case, GRB1 happens first, GRB2 happens next and GRB3 happens as the last GRB. When the GCN alert notifying the GRB1 arrives, we stand at a point before the beginning of the night, before the planned observation interval for GRB1, which is the blue part shown in Figure 2.5, starts. The allowed observable interval for GRB1 is 5 hours, but the maximum time configured to be allocated for observations is 3 hours. Hence the observation run of GRB1 is allocated as 3 hours at the beginning of its allowed observable interval. Then, the GCN alert for GRB2 arrives. At this point, we are before the start of the orange part shown on the second grey rectangle in Figure 2.5. The allowed observable interval for GRB2 is 6 hours, but again since the maximum time to be allocated is 3 hours, the observation run fo GRB2 would be 3 hours at the beginning of its allowed interval.

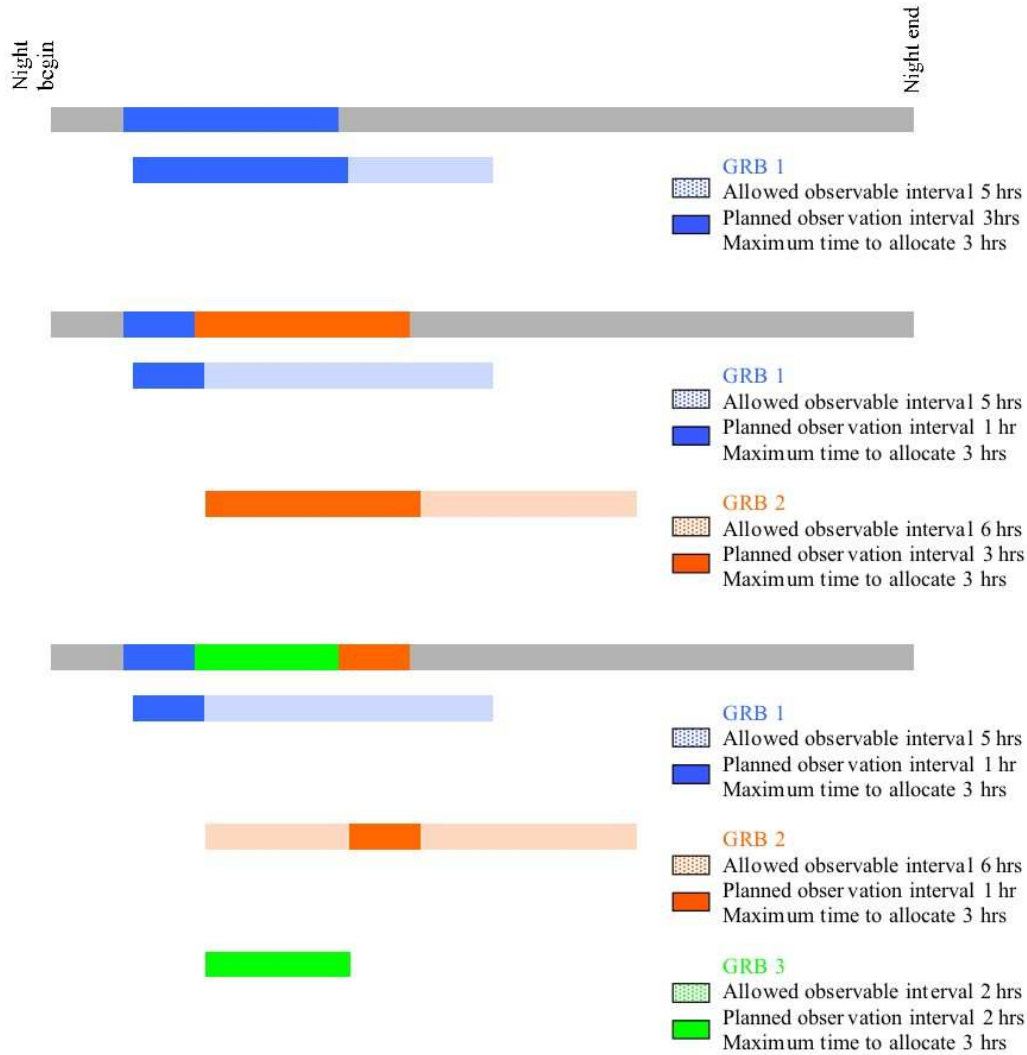


Figure 2.5: An example case illustrating the scheduling mechanism for the *lazy* mode.

The night is represented in grey color. Each grey rectangle represents the schedule of the same night, where the latter grey rectangles are the schedule of night after the arrival of a new GRB. At the beginning, as shown in the first two boxes, there is only GRB1 and its observation plan is added to the schedule. Next, GRB2 arrives and since it happens later it has a higher priority. Therefore the observation plan of GRB2 is scheduled as 3 hours, overriding the last two hours of that of GRB1, as shown in the 3rd, 4th and 5th boxes. As the last GRB, GRB3 arrives and thus it has the highest priority. It is visible only for 2 hours and therefore its observation plan is scheduled covering its whole observable interval, overriding the first two hours of the observation plan of GRB2, as shown in the last four boxes.

However, the first 2 hours of this plan coincides with the last two hours of the scheduled observation for GRB1. In this case, the priority comparison takes stage. GRB2 occurred later in time and there were no user modifications to the priorities, so GRB2 is prior than GRB1. Therefore, the observation plan of GRB2 overwrites the last two hours of the observation plan of GRB1. The last GRB for this example is GRB3, for which the GCN alert arrives at a point in time earlier than the start of the green rectangle (see Fig.2.5). The allowed observable interval for GRB3 is 2 hours, which is smaller than the maximum time to be allocated for observations. Thus, all of the allowed interval of GRB3 is planned for observation. However, it falls on top of the first two hours of the previously planned observation of GRB2. Similar to the case between GRB1 and GRB2, GRB3 has the highest priority since it occurred as the latest. Therefore it overwrites the first two hours of the observation plan of GRB2. The final situation of the observation schedule for the night is shown on the third grey rectangle in Figure 2.5.

The *smart* mode is named such because it shifts or rescales the observation plans when necessary. For this purpose, it always works on the allowed intervals of the observation plans. If we take the same example in the *lazy* mode, that when plan A is partially or totally covered by a higher priority plan B, the system in *smart* mode tries to shift plan A to another location within its allowed interval. An example case is illustrated in Figure 2.6. The GRBs and therefore their allowed observable intervals and the order of their occurrence are the same as in the previous example used for explaining the *lazy* mode scheduling (see also Fig. 2.5). The difference between the *lazy* and *smart* modes show itself when there is a coincidence between observation plans of two GRBs. Let us first have a look at the case when the GCN alert of GRB2 arrives. As in the example for the *lazy* mode scheduling, since GRB2 is prior than GRB1, its observation plan is allocated first. The planned observation for GRB2 is 3 hours, 2 of which coincides with the last 2 hours of the planned observation of GRB1. In this case, the GP system tries to re-allocate the observation plan of GRB1 if we are at a point in time earlier than the start of the blue rectangle in Figure 2.6. Otherwise, if the observation of GRB1 has started, its observation plan cannot be re-allocated.

Similar to the *lazy* mode, the observing and initiating plans are treated separately also in the *smart* mode. However, the treatment and hence the results are not the same. For the *smart* mode, a plan that is currently being observed, is handled almost the same as in the *lazy* mode, that is, the system is not allowed to shift it completely to another place, but the plan can be contracted or it can also be expanded which is not possible in the *lazy* mode. The plans that are not yet observed but initiated, are handled differently than the currently being observed ones, because they are allowed to be shifted. However, they are still different than the other observation plans, because if the modification is a continuation of the current plan, like a contraction or expansion of its duration, then it cannot be treated as a shifting.

Let us assume that the observation has not started yet. The GP system searches for the longest interval available within the allowed observable interval of GRB1 omitting the interval coinciding with the observation plan of GRB2. There are two intervals left,

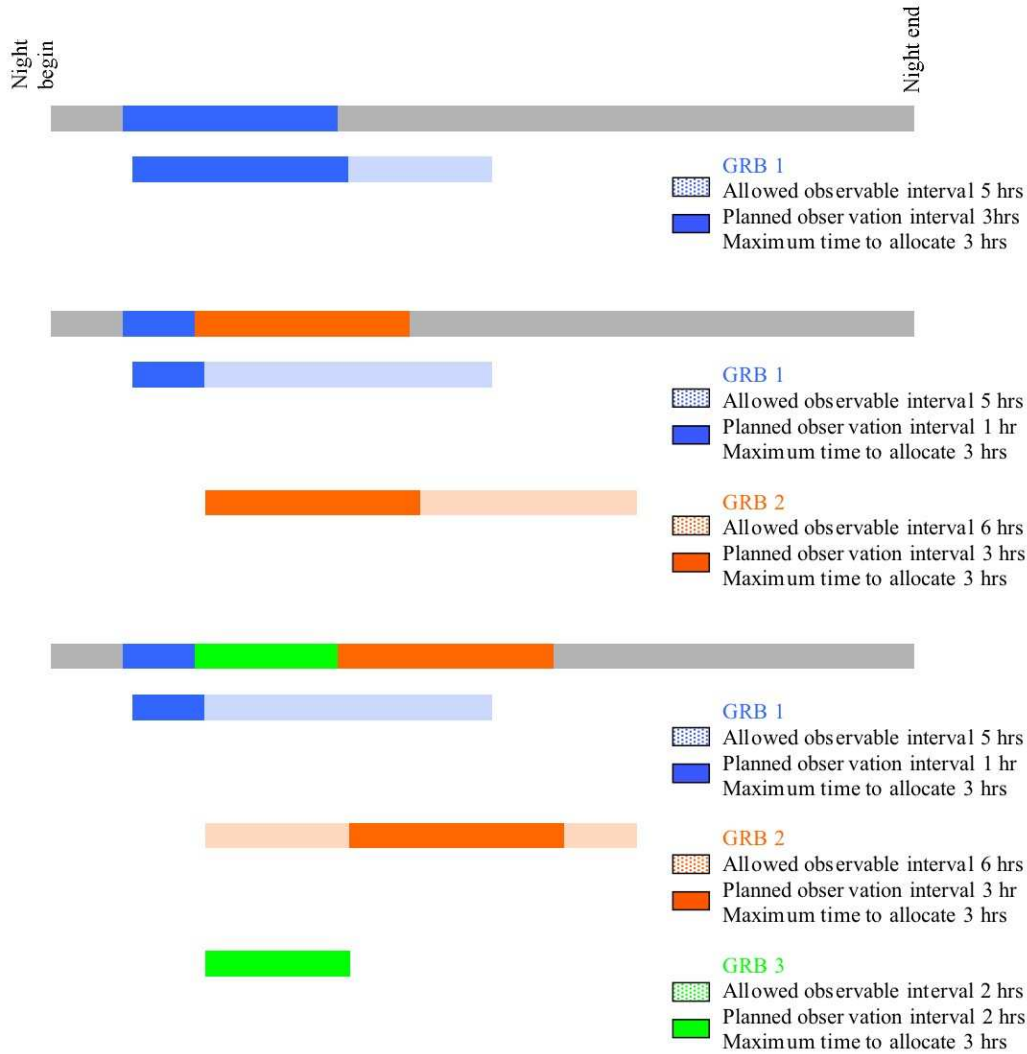


Figure 2.6: An example case illustrating the scheduling mechanism for the *smart* mode.

The night is represented in grey color. Each grey rectangle represents the schedule of the same night, where the latter grey rectangles are the schedule of night after the arrival of a new GRB. At the beginning, as shown in the first two boxes, there exist a single observation plan that belongs to GRB1. Next, GRB2 arrives as the latest burst, and thus it has a higher priority. The observation plan of GRB2 is scheduled as 3 hours, overriding the last two hours of that of GRB1, as shown in the 3rd,4th, and 5th boxes. As the last GRB, GRB3 arrives and thus it has the highest priority. It is visible only for 2 hours and therefore its observation plan is scheduled covering its whole observable interval. Due to the conflict between the observation plans of GRB3 and GRB2, the observation plan of GRB2 is shifted to its next available visible interval of 3 hours. The latest schedule of the observations and the individual observation plans are shown in the last four boxes.

each one hour long. In this case, the GP chooses the first interval in time. The resultant schedule of the night is illustrated on the second grey rectangle in Figure 2.6. Then, GRB3 arrives as the latest and most prior GRB. Since GRB3 has the highest priority its observation is planned first, and the other observation plans are re-scheduled accordingly. The allowed and planned observation interval for GRB3 is 2 hours, which coincides with the first two hours of the observation plan of GRB2. The GP searches for the longest time interval within the allowed observable interval of GRB2 omitting the coincident interval. The longest and in fact the only time interval available for GRB2 is 4 hours just after the end of the observation plan of GRB3 (see Fig. 2.6). However, the maximum time for allocation is configured as 3 hours, hence the observation for GRB2 is planned as 3 hours starting at the end of the observation plan of GRB3. The resultant schedule of observations of the night is illustrated on the third grey rectangle in Figure 2.6.

The *smart* mode is set to be the default scheduling mode, however, users may change it whenever they want. The advantage of *smart* mode is that it tries to schedule longer observations via shifting the observation plans when overridden. On the other hand, the advantage of the *lazy* mode is that it is simpler and hence the resultant schedule of observations is easier to predict.

2.2.3 Automating the GRB Afterglow Observations

After scheduling, timers are set by the system to the planned beginning and ends of the observations, in order to start and stop the observations at those times. At a planned observation time, the timer is activated to run the observation executer service. Instead of immediately starting or stopping an observation, the executer checks the current state of the observation plan table by polling the observation plans for the night and the current observing and initiating plans, if any. It examines the planned begin and end times of the observation plans to find the ones that have to be stopped and started. It is done in this way because the scheduling of the observation plans is subject to change. For example, an observation plan may be scheduled and the timers are set accordingly to the start and stop time, but another GRB may occur and shift this plan. In this case the timers to run the executer service would still run but there will not be any plan to be started, or the first set stop time would be wrong. Therefore, every time the executer service runs, it always checks the current state and acts accordingly.

The dataflow for the automated observations is illustrated in Figure 2.7. When the start time of an observation is confirmed, the system triggers the Rapid Response Mode (RRM) with the coordinates of the target and the name of the observation block to be used. RRM is a system used at the Paranal observatory of ESO⁷, and implemented for the first time to the La Silla observatory for GROND. It is a system that is used to trigger the telescope and the instrument for observation in a very short time and almost automatically. The only human intervention in the RRM system occurs as an acceptance or rejection of the

⁷see <http://www.eso.org/observing/p2pp/rrm.html>

trigger and the selection of the guide star, both done by the night astronomer at the observatory site. However, this intervention is only allowed for a duration of 30 seconds after the trigger is activated, and if the night astronomer does not interrupt during that time, the RRM trigger is automatically accepted.

For GROND, the GP system triggers RRM always with an observation block (OB) having zero exposure time. In this way we trigger the telescope and point it to the coordinates of the target, but still have the degree of freedom to choose the type and exposure time of the first observation block. The RRM is sent via ftp to the RRM server of ESO. However, the ESO RRM system is not always active, and moreover even if the system is active, it is not guaranteed that the RRM trigger will be accepted. There is a web page provided by ESO for the RRM log, so the GP system parses that web page periodically to understand whether the RRM was accepted or not.

After the RRM trigger, the next observation blocks are sent in a different way, that is to the Instrument Work Station (IWS). IWS is a system based on ESO instrument control software and it controls the instrument GROND. The GP system does not have direct control on GROND but it does it via the IWS, in an indirect manner. Due to the regulations of ESO, in order to connect to and be connected via internet, the GP system is located outside the special security area where all the instrument work stations are located. However, this restricts the communication of the GP with the IWS; the GP is not allowed to access directly to the IWS.

To solve this problem, Abdullah Yoldas, with Gyula Szokoly, designed and implemented a communication protocol between the IWS and the GP. Whenever the IWS is triggered or finishes an observation, it asks “NEXT” to the GP, and the GP answers with the parameters of the next observation block to be executed by the IWS. If the GP decides not to continue to the observation, it replies as “STOP” to the “NEXT” question of the IWS. In this way, the GP controls the observations by arranging their parameters, sequence and start (via RRM) and stop times.

The communication between IWS and the GP should be fast, with a typical timeout of 5 seconds, and if the main system process communicates with the IWS, there is a risk that it may not reply to the “NEXT” question on time, and so cause it to be stopped. Hence, the process that communicates with the IWS is not the main process but a dedicated one called OBServer.

When the GP triggers the RRM, without waiting to see whether it was successful, it sends the parameters of the first observation block in the OB sequence of the triggered observation run, to the OBServer. This is done to overcome the possible problems, i.e. network problems etc., that prevents the GP system learning the success result of the RRM trigger on time. For example, the GP may not learn the state of its RRM trigger because of a problem in the internet connection, but in the mean time the trigger may have been accepted and the IWS is asking the “NEXT” question for the parameters of the next real OB. However, with this design, the OBServer is ready to answer with the parameters of the next real OB.

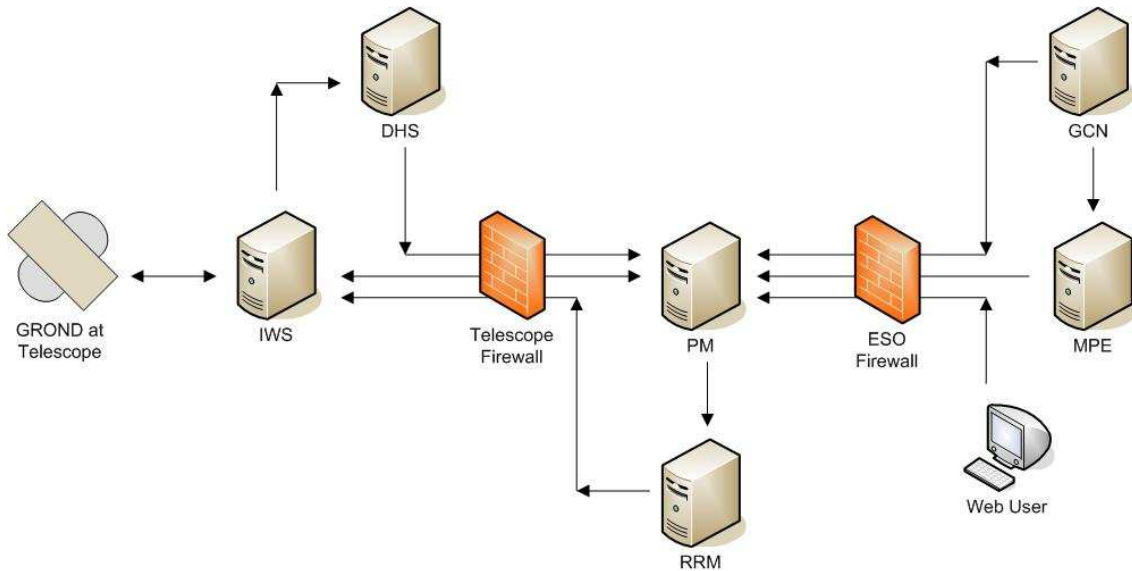


Figure 2.7: The dataflow scheme of the automated observations. GRB alerts are sent both from the GCN machine and from a server at MPE, passes through the ESO firewall and arrives at the Pipeline Machine (PM) where the GP is located. The GP triggers the RRM system via the ftp server on the RRM machine. The RRM machine then sends the triggered OB to the IWS through a firewall which secures the telescope area. When IWS receives the RRM OB, it controls GROND and thus the telescope to obtain data. When the data arrives to IWS, it is forwarded to the DHS machine which hosts a data handling system. The DHS system then sends the data to the PM again through the telescope firewall. The GP at the PM machine can communicate with the other machines in the specially secured telescope area only in an indirect manner.

The situation is more complicated if there is another ongoing observation of another target or another observation run. In this case the OBServer possibly holds the parameters of the new trigger (without yet knowing whether the trigger is accepted or not), the parameters of the next OB of the ongoing observation run, and the parameters of the last sent OB. When the IWS asks “NEXT”, if the last and next OBs belong to the same observation run, and if the “NEXT” question is asked approximately after the duration of the last submitted observation block is passed, the OBServer decides to send the OB parameters of ongoing observation run. Otherwise it sends the OB parameters of the new trigger.

The analysis part of the system (see section 2.3) can also affect the next observation block such that the exposure time and therefore the type, and the telescope pointing position of the next observation block can change as a result of the analysis of the previous set of images. The GP main process always passes the parameters of the next observation block in the OB sequence of that observation run, to the OBServer. If the parameters change as a result of the analysis, the main process passes these new parameters to overwrite the previously passed ones. However, since the system works asynchronously, it is not guaranteed that these new parameters will be received on time and passed to the IWS as an answer to the “NEXT” question.

Once the RRM is accepted and/or the first OB of the new target is submitted to the IWS, the main process of the GP system creates a GRB process called GRBServer. This GRB process has several subprocesses that it controls. It is responsible for the analysis of all the images obtained for that observation run. However, the automation of the observations is still under the control of main system process since there can be more than one GRB process running at the same time, i.e. one GRB process that is analysing the incoming data from the currently ongoing observation run, and another GRB process that has not finished the analysis of the data from the previous observation run, possibly data of another GRB.

The rest of the subsections are a part of the analysis layer of the GP system, and all of them are controlled by the GRB process⁸.

2.3 Analysis layer: Analysing GRB Afterglow Observations

The analysis layer consists of GRB processes that host and control several other subprocesses doing the data analysis. Similar to the method adopted for the system–observation layer, the organization of the subsections are such that they describe a sequential order of the events, although the system itself has an asynchronous structure. The sequence, as illustrated in Figure 2.8, is enforced by the prerequisites of each task, i.e. identification of the GRB afterglow requires that the images of an observation block has been acquired, photometrically analysed, calibrated and the objects found in different filter band images are matched with each other.

⁸When there is more than one GRB process running, each GRB process controls its own analysis subprocesses

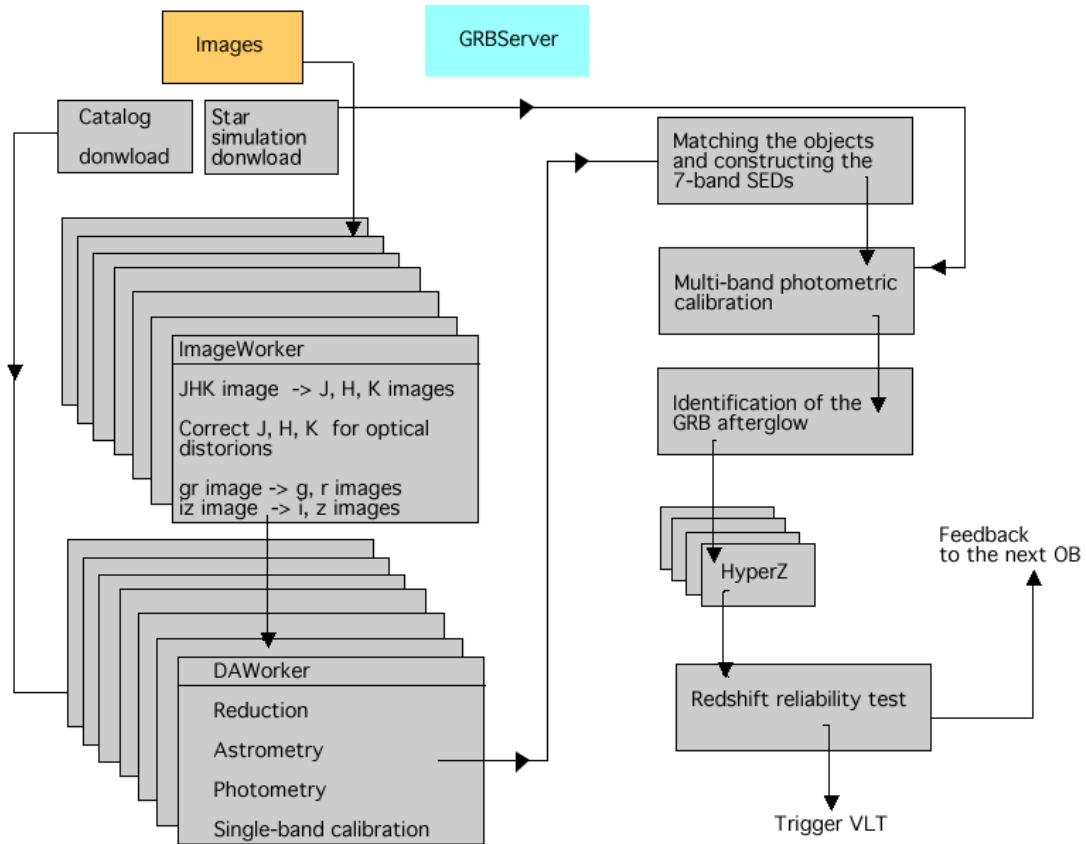


Figure 2.8: The sequence enforced by the prerequisites of events occurring inside the GRBServer process. The details of the events/processes are described in the following subsections.

2.3.1 Preparing for Analysis

There are several things a GRB process should conduct immediately after initiation. First of all, it should ensure that all its subprocesses are ready for the analysis of incoming data. These subprocesses, or in other words workers, include the pool of data-analysis workers and image pre-processing workers. Each data-analysis worker will conduct the photometric analysis of a single band data. To be able to conduct the analysis of the 7 band data at the same time, the number of data-processing workers, running simultaneously in parallel, are at least 7 (in fact 14 for back-up purposes). Similarly there is more than one image pre-processing worker each waiting for incoming images to pre-process and prepare them for the data analysis.

Another reason for starting the data analysis and image pre-processing subprocesses is the time consumed required to loading of IRAF/Pyraf libraries utilized in data analysis. IRAF⁹ is a data reduction and analysis software package of NOAO, and Pyraf¹⁰ is a Python wrapper for IRAF, provided by the Space Telescope Science Institute. At the startup, the Pyraf libraries are loaded into memory, however, taking a substantial amount of time. Therefore, by utilizing these processes as workers in a pool, started once at the very beginning and continuously serving, the system overcomes the substantial overhead caused by Pyraf startup.

Moreover, the GRB process downloads data from optical and infrared catalogs, namely USNO A-2, USNO B1, DENIS, 2MASS, NOMAD and GSC22 via internet¹¹ (Ochsenbein et al. 2000). These data are formatted to be later used by the data analysis workers for single band data photometric calibration. GRB process also downloads simulated data of galactic foreground stars¹² for the position of the GRB that it will analyse. These simulated data will be used by the 7-band relative photometric calibration code. The downloading of the catalogs depends on the conditions of the internet connection and the catalog servers, therefore the downloads are conducted at the very beginning, for later use.

2.3.2 Analysing each Observation Block

When an observation is executed, images start to appear in a certain directory, as the data handling system (DHS) of ESO pulls them from the IWS and stores them in this directory under the pipeline machine. The images are read as blocks instead of single band images by the read-out electronics of GROND; instead of single J, H, K images, for each exposure infrared data are stored as one image and similarly instead of single g, r, i, z' images, for each exposure all optical data are stored as one image. The infrared images are preprocessed in order to correct for the optical distortions due to many lenses in the

⁹see <http://iraf.noao.edu>

¹⁰see http://www.stsci.edu/resources/software_hardware/pyraf

¹¹<http://vizier.u-strasbg.fr/viz-bin/VizieR>

¹²http://bison.obs-besancon.fr/modele/modele_do.html

system. The image pre-processor utilizes the code written by J'org Brunschweiler. It also divides these blocks properly into 7 single band images. These images are then fed to data analysis processes for photometric analysis, by the GRB process, accordingly. Note that all data analysis processes can analyze any of the 7 band data. The reason for their existence in large numbers is to be able to analyze more data simultaneously, ideally, of course, all the 7 band data.

The distribution of the images to the data analysis processes depends on the structure of the OBs. There are two main reasons for this dependence. The first reason is that we need to construct a spectral energy distribution (SED) of the target object to be able to determine its photometric redshift¹³. SED of an object is a collection of magnitudes of different broadband filters obtained at the same time. Therefore we need to acquire and analyze the images in such groups that in the end we obtain the magnitudes in different bands that were acquired simultaneously.

The second reason is the need for a specific treatment to the infrared band data. The night sky, observed in infrared (IR) wavelengths, is too bright and starts to dominate over the signal from astronomical objects for exposures larger than a certain duration. Therefore it restricts the brightness limit of the observations almost independent of the exposure time, resulting in the detection of very bright objects only. Fortunately, there is a special technique, called dithering, used to overcome this problem of bright infrared night sky. The main idea is to obtain several IR images centered to slightly shifted locations on the sky. In this way a bright object does not stay at the same position on different images and therefore for a pixel the probability that it does not fall on an object but on sky is larger. The sky value is calculated for each pixel of the detector by taking the average of the values of the same pixel of the images taken before and after the current image. The outliers are rejected in the averaging procedure. In case there are fewer images than a user configurable number of images this method cannot be used and instead the median of the images are taken to form the final image. Therefore in order to discard the bright infrared sky, the infrared images cannot be analyzed one by one, but have to be analyzed in groups obtain in a dithered way around the same central position.

There are two ways to provide the dithering for IR images. The conventional one is to change the pointing of the telescope slightly around the same location. This, however, has implications. Moving the telescope results in dithering not only for the IR bands but also for all bands on the detector; i.e. for all 7 band data for GROND. However, the read-out time for the optical CCDs are generally long on the order of tens of seconds and so it is not possible to dither every 10 seconds. To overcome this problem an additional method for dithering for the K-band data has been implemented for GROND. There is a mirror in front of the K-band detector that moves and provides the same effect of pointing to different directions. However, as this is only available for the K-band detector due to spatial considerations, GROND still needs to be re-pointed by moving the telescope.

The observation blocks for GROND have been formed taking into account these needs

¹³The details of how to obtain the photometric redshift are described in section 1.2.2.

described above (see Figure 2.4, and also Steiner 2005; Krühler 2006). The analysis strategies are therefore based on these OBs. In the IR bands we are bound by the requirement of dithered analysis as explained above. However, for the optical bands the situation is different, allowing different analysis strategies. The optical bands can be analyzed as single images or a group of images obtained subsequently at the same telescope pointing position. Moreover, if the effect of dithering can be neutralized, there is also the possibility to analyze the images obtained for different pointings. Neutralising the effect of dithering on optical images is implemented by shifting the optical images such that they center on the same position, and then by adding them. In this way we lose the edges of the images since those parts are not covered by all of the images. We have defined 4 different strategies:

If the K-band mirror dithering is not used; i.e. when the dithering mirror does not work:

1. All the IR bands are analyzed at the end of the OB. That is the J,H,K band images are collected till the end of OB and then given to three data analysis processes for photometric analysis. Similarly, the optical data are also analyzed at the end of OB, using the shift-and-add method.
2. The IR images are analyzed in the same way as in option 1, but the optical images are analyzed separately at each different telescope dithering position. However, in this case after the photometric analysis a further process is required for the optical bands, to be able to construct the SED of the object, which is simultaneous with infrared.

If the K-band mirror dithering is used:

3. The K-band data are analyzed separately at each telescope dithering position taking into account the mirror dithering. The J and H bands are analyzed at the end of the OB. Optical data are also analyzed at each different telescope dithering position. As mentioned in option 2, a further process described in section 2.3.4 is necessary for the K and the optical bands, to be able to construct the SED.
4. The K-band data acquired at each telescope dithering position are reduced but not further analyzed to conduct photometry. These reduced data are collected for each telescope dither position and then analyzed at the end of the OB similar to the J and H bands. J and H are as always analyzed at the end of the OB. Optical band data are also analyzed at the end of the OB by the shift-and-add method.

All four strategies have advantages and disadvantages. The methods 1 and 4 depends on the success and quality of shift-and-add method on the optical images. On the other hand, the methods 2 and 3 requires a further step as described in subsection 2.3.4. The default strategy will be determined according to the status of the K-band dithering mirror and the reduction tests that are applied on GP.

2.3.3 Photometric Analysis

We will conduct automated photometry on all GRB afterglow data obtained by GROND, as a part of the GP. Automated photometry covers the reduction of the images, astrometry, photometric analysis and a basic photometric calibration. It is applied to all images

grouped according to the wavelength band and also as sets of images depending on the analysis strategy. Brief definitions of photometry and astrometry are given in the Concepts subsection. The details of the procedure are then described in the following paragraphs after the Concepts subsection.

Concepts

Photometry is measuring brightness of astronomical objects. This can be done by measuring the flux, which is energy per unit time per unit area, of the object at a certain wavelength range. The convenient photometric unit for brightness is magnitude.

The magnitude unit system is based on a logarithmic flux scale. It was first invented by Hipparchus around 120 B.C. Hipparchus classified the stars he observed, in units of magnitudes ranging from 1 to 6, where first magnitude stars were the brightest. By the time those stars were re-observed by modern telescopes, it was found that each magnitude is roughly 2.5 times brighter than the next larger magnitude.

Therefore, the magnitude system, re-defined based on Hipparchus' definition, can be formalized as follows:

$$m_1 - m_2 = -2.5 \log_{10}(f_1/f_2) \quad (2.1)$$

where f_1 , f_2 are the fluxes and m_1 , m_2 are the magnitudes of object 1 and 2. To solve the problem of relative magnitudes, there are different systems with different zero points where a certain star or flux value is chosen to have a magnitude of zero. The most common magnitude system is the Vega magnitude system where the star Vega is used as a zero point. In that case the magnitude of an object can be expressed as:

$$m = -2.5 \log_{10}(f/f_{vega}) \quad (2.2)$$

These are “apparent magnitudes” since they are distance dependent. The distance independent magnitudes are called “absolute magnitudes”. The absolute magnitude is defined as the brightness of an object if it were exactly 10 parsecs away.

The photometric analysis can be conducted, in general, using two different methods, namely, aperture photometry and psf photometry. In aperture photometry, the brightness is calculated by measuring the flux of the object within a certain fixed aperture size, and then subtracting the contribution of the background sky. Aperture photometry is preferred if the analysis is done interactively or for an uncrowded field. For crowded fields or automated analysis, psf photometry is preferred. In psf photometry the brightness of an object is calculated by fitting the point spread function (PSF) to field objects. Point spread function is the function that describes how a point source appears in the images.

Astrometry is the measurement of the positions of the astronomical objects. When an image of the sky is obtained by a telescope, it contains the positional information in terms of image coordinates (pixel coordinates). To translate the position information from image pixels to celestial coordinates, a system called “World Coordinate System” (WCS) was

developed. WCS is a standardized format of storing the coordinate information in the image headers allowing to transform between pixel and celestial coordinates.

Usually, the telescopes cannot point very accurately at the given coordinates. Therefore, the coordinate information that is contained in the image header is not precise. To obtain the precise positional information, an astrometric correction is applied to the fits headers of the image. Astrometry is necessary and important in the case of GRB observations, since a GRB afterglow is a new source that needs to be identified. Therefore, we need an abstract measure of the positions to identify the object of interest.

Astrometry is done in several steps. To find the correct positions we need to have a reference system to compare with our image. This reference is provided by the catalogs. By comparing the positions of the objects we observe, with that of the objects in the catalogs within the same field of view, we can obtain the correct position information of our images.

First Step: Reduction

Before doing photometric analysis, the images first need to be corrected for the additional noise, i.e. the zero level and dark current, introduced by the detector electronics, and the multiplicative effects, i.e. the gain and the illumination variations across the image.

The zero level current is determined by taking “bias” or “zero” images that have in principle an exposure time of zero seconds. The “dark” current is similarly determined by obtaining images that have a similar duration as the observations of the scientific target, but obtained without exposing the chip to light. Both bias and dark current are additive effects, therefore the image can be corrected by subtracting them from the image.

The multiplicative effects can be determined by obtaining “flat-field” images. Flat-field images are obtained either by exposing the dome or the twilight sky for a duration long enough to reflect possible imperfectness of the chips. The images are corrected for the variations in the sensitivity through the chip via division by flat-field images.

The procedure of reduction makes use of two different programs depending on the analysis strategy. For GROND, we will have one master bias and one master flat-field image per detector, and also one master dark image for infrared detectors. These master bias, master dark and master flat-field images will be a combination of bias, dark and flat-field images that are obtained and combined by the night-astronomer daily. Once these master images are ready, the reduction procedure is rather standard.

One of the two reduction methods utilized by GROND Pipeline is application of a single IRAF task called *ccdproc*. This method is applied to images that were obtained without dithering, i.e. optical images obtained at a single telescope dithering position. The *ccdproc* task corrects any number of images first by subtracting the master bias image and then by dividing by the master flat-field image. When there is more than one image, they are combined by summing up using another IRAF task called “imcombine”, after the *ccdproc* task is applied.

For some tasks utilized in the photometric analysis, including the *ccdproc* task, IRAF needs some information stored in the fits header keywords of the images. In principle, IRAF can lookup at the image headers and search for the necessary keywords for a given task. However, IRAF has a problem in reading the fits header keywords that are longer than a certain length, which is the case for ESO fits header format. Therefore instead of letting IRAF to search for the value of a fits header keyword, the fits headers are read by the photometric analysis process itself after the reduction step (independent of the method used for reduction), and the values are used when necessary.

Our other reduction method utilizes a software package of ESO called *eclipse*. Similar to the first method, it involves application of a single task called *jitter* to reduce the data. The distinguishing property of *jitter* is that it calculates the background sky flux given a set of images obtained at slightly different telescope positions. It corrects the image for additive and multiplicative noise effects by subtracting the bias and dark images and dividing by the flat-field image. After that it shifts and adds the images obtained at different telescope positions, and also corrects the value of the sky background calculated with a special algorithm, if desired. This method is applied to images obtained with dithering, i.e. infrared images obtained at several different telescope dithering positions.

Second Step: Astrometry

The first step of astrometry is to identify the objects in the image. This is realized by the IRAF task called *daofind*. *Daofind* task finds the objects in the image by fitting a gaussian with a configurable full-width-at-half-maximum (FWHM) value. Other important parameters for this task are the noise level of the background, the read-out noise and gain of the detectors, and the detection threshold that would be used to detect objects with a signal above this level.

The output coordinates of the objects detected in the image are represented using the “physical coordinates”. Physical coordinates are pixel coordinates invariant with respect to linear transformations of the physical image data, i.e. when a new image is created by extracting a section of an image, for the new image the origin of the coordinate system remains the same with that of the original image. Therefore, the coordinates will always be represented with respect to the original image no matter the modifications made on it. This representation system is the most appropriate one for the GP because although the image may be modified throughout the analysis, it would still be possible to compare the coordinates at any stage of the analysis, and also with the coordinates of the objects found by external programs utilized during the analysis.

The next step has two alternatives. One of the alternatives is to follow a two-stage procedure. First stage utilizes a publicly available FORTRAN program, written originally by Uri Givon and Eran Ofek¹⁴ and modified by Gerd Tróger, in order to compare the positions of the objects in the image with positions of the stars in the catalog for the

¹⁴<http://wise-obs.tau.ac.il/eran/iraf/index.html>

same area we are observing and find an average shift in the positions to be used as an initial guess. Second stage utilizes an IRAF task *xyxymatch* to match the positions of the objects in the image with those of the stars in the catalogs. The task *xyxymatch* has two algorithms, tolerance and triangles. The tolerance algorithm needs initial estimates for the shift in x and y coordinates, therefore the second stage needs the results of the first stage.

The other alternative is also to use the IRAF task *xyxymatch*, however this time utilizing its triangles algorithm. The triangles algorithm applies a triangle pattern to match between the coordinates of the image and catalog objects. It does not need any initial estimates. This alternative is more secure since it does not depend on any other output as in the case of the first alternative, but it is slower. To overcome the speed problem, the number of objects used for matching should be reduced. For that purpose we utilize another IRAF task *pstselect* before running *xyxymatch*. The *pstselect* task selects a user configurable number of stars in the image which are bright, unsaturated and well-fit a Gaussian profile. Hence, instead of using all the objects in the image, we only use the stars selected by the *pstselect*, as an input to the *xyxymatch* task. The last step of the astrometry is to find and apply the astrometrical solution using the result of the previous step, via the IRAF task called *ccmap*.

Third Step: Photometry

For GROND, we use the psf photometry method to conduct the photometric analysis. We apply two alternative methods to select the stars that will be used to model the PSF. The first method is to use a public photometry program called *DoPhot* (Schechter et al. 1993). As the alternative second method, we use an IRAF task to do it. In general, we follow the main items of the psf photometry procedure described in the IRAF manuals¹⁵.

DoPhot is a photometry program, which does everything, from finding the objects and classifying them to calculating their magnitudes, in one run. *DoPhot* serves two purposes for our GROND pipeline, classifying the objects in the image and calculating the FWHM. *DoPhot* calculates different FWHM depending on the type of the object, i.e. star, galaxy, etc.. In other words the same kind of objects have the same FWHM value. In the first photometric analysis method of GP, we select the objects that are classified as “star” by *DoPhot*. We also take the FWHM value of the “star” objects and use it instead of the initially configured FWHM value for the rest of the analysis. The “star” objects are then given to the IRAF task called *psf*, in order to be used as model stars for PSF shape calculation.

The second method, is to use the IRAF *pstselect* task to select the psf model stars. This task may have been already utilized during the astrometry, as described above, then the results of it are used directly without running it for a second time. The only disadvantage of this alternative without *DoPhot* is that we cannot automatically determine the FWHM

¹⁵see <http://iraf.noao.edu/docs/photom.html>

of the stars using any IRAF task. As in the first method, the objects selected via *pstselect* task, are then given to the *psf* task of IRAF, in order to model the psf function of our images.

The last step of the psf photometry is to fit the PSF function determined by the *psf* task, to all of the objects in the image that were found by the *daofind* task. This is done via another IRAF task called *allstar*. As a result of this fit, the magnitudes of the object are calculated by the *allstar* task.

Fourth Step: Single Band Photometric Calibration

The magnitudes that are obtained at the end of photometric analysis are so-called “instrumental magnitudes”. Instrumental magnitude is the magnitude of an object determined based solely on the data at hand. Therefore, it depends on the properties of the instrument that is used to observe the object, and the conditions of the observation. To have an objective measure of the magnitude of the object, we need to normalize it with a zero-point. However, since the zero-point is dependent on the conditions of the observation, it is not a fixed value.

We do two kinds of photometric calibration in the GROND pipeline. The first step is applied to each individual band, whereas the second step is applied using objects that exist in all bands as described in the next subsection.

The idea of the photometric calibration is to determine the zero-point for each observation, by comparing the instrumental magnitudes of the objects that exist both in our images and in the catalogs. For the GROND pipeline, we use the magnitudes in the catalog of the corresponding filter, to compare with the instrumental magnitudes of the objects that are both in that catalog and in our images. The filters used in GROND are different from the ones in the catalogs. Therefore before comparing the two sets of magnitudes we first convert the magnitudes taken from the catalogs to magnitudes represented in GROND’s filter system. As a result we have both the instrumental magnitudes and catalog magnitudes calculated for the same filter system. For the comparison of these two sets of magnitudes we assume a linear correlation having a slope of 45 degrees between them. We calculate the zero-point by taking the median of the differences between the catalog and instrumental magnitudes. The standard deviation of this calculation is summed quadratically with the magnitude error values for each object in order to obtain the resultant error in the magnitudes.

2.3.4 Multi-band Photometric Calibration

At the end of the automated photometry, every data analysis process outputs the coordinates, magnitudes and magnitude errors of the objects detected in the corresponding band data. Therefore, these individual data outputs should be matched. The aim is to form a big table composed of coordinates of the objects, and their magnitudes, magnitude errors for all seven bands, if available. In other words, this tabulated data contains all the

objects detected, with their magnitudes and magnitude errors in whichever bands they were detected. For non-detection in a certain band data, the magnitude and error are left NULL.

Depending on the strategy used for that analysis (see section 2.3.2), the GRB process matches the objects found in each of the 7 band data accordingly. The easiest case is for the analysis strategy type 1 and type 4 (see page 39), as the magnitudes of the objects were obtained using data acquired at the same time and for approximately the same time interval. The GRB process compares the coordinates of the objects detected in different bands and matches those within a certain configurable proximity to each other.

For strategies type 2 and type 3 (see page 39), the process is more complicated. For type 2, the IR band data are analyzed at the end of the OB and therefore the output magnitudes cover the whole OB interval. On the other hand, since the optical band data are analyzed separately for each telescope pointing, there is more than one¹⁶ output for one OB for these bands. Therefore, the GRB process should first match the objects detected in those separate analysis for each optical band, and take the average of the magnitudes found in each analysis, assuming that the magnitude of the detected object either stays constant, or changes conforming a power-law. For example, the GRB process should first match the objects detected in all g-band data of that OB, and take the average of the corresponding g-band magnitudes for each object. If the object is not detected in all of the, i.e. g-band, data of that OB, the GRB process averages the available magnitudes over the number of images in that OB for that band.

After the objects detected at each band are matched and their corresponding magnitudes and magnitude errors are calculated accordingly, the next step is to apply another photometric calibration to cross-calibrate between different bands. Since we will calculate the photometric redshift based on the SED, we do not need absolute photometry in principle. However, the cross-calibration between the bands should be correct and this is not guaranteed by the single band photometric calibration using the catalog magnitudes since the magnitudes in the catalogs are usually not accurate enough. The usual approach to do accurate photometric calibration is to observe photometric standard stars, whose magnitudes are well-established and accurate, just before or after the targeted observation. However it is difficult to find a nearby appropriate field in the sky that hosts photometric standard stars and more importantly it would cost a lot of time to point the telescope and observe such a field. In the case of newly detected rapid transient sources such as GRBs, it is usually not possible to observe photometric standard stars before the GRB observation, simply because we cannot know when and at which position a GRB may occur. To observe standard stars after observing the GRB is also disadvantageous for two reasons. First, the GRB may occur a short time before the night ends or another GRB may occur or scheduled just after it, and hence no time is left for a standard star observation. Second and more importantly, for automated observation and analysis systems like the GP system, it would delay the analysis of the whole observation since the aim of the

¹⁶The number of outputs are equal to the number of telescope pointing positions for that OB.

GROND GRB observations, that is, determination of the redshift of the GRB, requires the photometric calibration.

To accomplish the cross-calibration, the GRB process selects the set of objects, which are detected in all 7 bands, and provides these sets of 7 band magnitudes to a photometric calibration program based on a library written by Bernhard Huber. This photometric calibration program compares the colors of these input objects with those of simulated data for that given location of the sky. The simulations are provided by Robin et al. (2003) and downloaded from internet¹⁷. The calibration code assumes that the K-band magnitudes are correct, and therefore base all the relative corrections on K-band magnitudes. As the output, this photometric calibration program provides the relative corrections (as additive values) for each band except K-band. After these corrections are applied by the GRB process to all of the objects in the big table for that OB, it moves to the next step: identification of the GRB afterglow.

2.3.5 Identifying the GRB Afterglow

The GRB afterglow has several observable properties that can be used as tests for its identification, as listed on the left column of Table 2.4. These items, however, are not items to be added by an “and” to each other; the GRB afterglow does not necessarily have to satisfy all of these items. The reason is that almost all of the items have exceptions that are listed on the right column of Table 2.4.

Therefore taking into account those exceptions, we assign a probability to each item and add them up for the candidates that satisfy those items. In other words, we give a mark to the candidates according to whether they satisfy a certain item or not, and in the end the candidate with the highest score is most likely the afterglow. The only property that needs to be satisfied for being regarded as a GRB afterglow candidate is the one listed at the first row in Table 2.4; that the GRB afterglow should reside within its γ -ray position circle. If this γ -ray position is revised and changed by astronomers during ground processing, then the GRB afterglow should reside in this revised and hence probably better calculated position error-circle. If this is not satisfied, the object is not considered as the GRB afterglow candidate, and the further tests listed in Table 2.4 are not conducted on that object.

The greatest advantage of this method is that it takes into account the exceptions, which are already observed in several cases. Another great advantage is that it can be applied retrospectively if any of the items change, as we do not throw away any object. For example, if there is a new γ -ray position error circle for that GRB, the tests can be applied retrospectively; that is to all the objects that were detected in previous OBs of that GRB.

The next step is to determine the photometric redshift of the most probable candidate(s).

¹⁷http://bison.obs-besancon.fr/modele/modele_do.html

Table 2.4: GRB afterglow properties (left) and exceptions to them (right)

The GRB afterglow should coincide with the position of the GRB itself determined from γ -rays; it should reside within its γ -ray position error-circle.	There are some cases that the γ -ray position error-circle was moved after ground analysis.
The optical/NIR afterglow should coincide with the position of the X-ray afterglow (if any); it should reside within the X-ray position error-circle.	The X-ray afterglow may in fact be a cosmic-ray, therefore the X-ray position error-circle may be wrong.
The GRB afterglow is a new source, it should not coincide with a source listed in a catalog.	If the GRB host galaxy is bright, it may reside in the catalogs and in that case the position of the GRB afterglow coincides with that of a source in a catalog which is in fact its host galaxy.
The colors of the GRB afterglow should resemble those of the other GRB afterglows previously observed.	The colors of GRB afterglows has a distribution but, as expected, with exceptions.
The afterglow emission is variable; it fades like power-law.	Although the afterglow emission usually fades obeying a power-law, there are many cases that it shows re-brightenings.

2.3.6 Determining the Photometric Redshift

The photometric redshift is determined using a common, publicly available code called HyperZ (Bolzonella et al. 2000). HyperZ is normally used to determine the photometric redshift of galaxies using different galaxy model template spectra. It fits the input object SEDs with the chosen template spectra, for a given range of redshift and intrinsic extinction. It is also able to correct for the foreground extinction if the $E(B-V)$ value is supplied.

HyperZ takes the following parameters as input:

- i The model template spectra used for fitting. One can choose either the default templates delivered together with the program, or can supply his/her own template spectra in text format as ASCII files.
- ii The object SEDs; the id of the object (a number), the magnitudes, and the corresponding magnitude errors.
- iii The ids of the filters used to obtain the input SEDs, the limiting magnitudes and the one of the 4 different behaviors HyperZ follows when an object is not detected in a certain filter band. HyperZ has a set of filters curves as default, but the users can also supply filter curves for their own filters.
- iv Values of several fit parameters. The most relevant ones for GP are a) the upper limit, and b) lower limit of the redshift, c) the step size in redshift, d) the upper limit, and e) the lower limit of the intrinsic extinction as A_V , f) the step size in A_V , g) the law to be used as the reddening law. If the reddening law is set to 0, it means that there is no intrinsic extinction, and the provided upper and lower limits, as well as the step size are ignored.
- v The root name of the output files and which output files are required. One exception to this is the name of the output involving the best fitting template spectrum redshifted and extinguished to the corresponding best-fit values for each object. The names of these output files are the ids of the corresponding objects supplied as input.

When started, HyperZ first forms a set of template spectra redshifted within the user provided redshift range in user provided step sizes. Then it adds extinction to each template within the user provided range of A_V using the user provided step size and reddening law. If the reddening law is set to zero, this step is ignored. Therefore, in the end of this first step HyperZ has a set of templates with various redshift and intrinsic extinctions, which is called “hyper-cube” by its authors (Bolzonella et al. 2000). HyperZ then transforms the magnitudes of the input object SEDs into fluxes by unfolding with the corresponding filter curves, and fits these SEDs with the template spectra in the “hyper-cube” using the χ^2 fitting technique.

The disadvantage of HyperZ is that, this whole process takes the order of minutes which is too long, especially when obtaining the redshift of the candidates from sequence of

4 minute OBs. Therefore Kiran Garimella modified the HyperZ code for us in such a way that after being started, HyperZ forms the “hyper-cube” as usual, but then it waits there for the input SED, and can process a series of input SEDs sequentially. In this way, HyperZ can re-use the “hyper-cube” it formed for more than one input SEDs. A further modification made by Kiran Garimella is that HyperZ now outputs two of its most important and useful results to the screen (STDOUT), instead of output files. Therefore the GP does not need to provide output file root name, as explained in item v, but instead reads the results from the STDOUT. Note, however, that HyperZ has to be restarted if any of its input parameters, other than the SED (and item (v), which is now obsolete), need to be changed.

The redshift range that can be observed by GROND is $z \sim 3 - 13$, and the accuracy of the photometric redshift determination is $\Delta z \gtrsim 0.3$ (see Fig. 2.10). Therefore, for any GRB process, the redshift range and the step size is fixed, and only one instance of HyperZ would have been enough if redshift were the only free parameter. However, this is not the case. Since GRBs occur inside other galaxies, we expect to have intrinsic extinction effects on the GRB afterglow SED. In most cases, the host galaxies analyzed to date have moderate extinction obeying the SMC/LMC like reddening law. Note that the effect of intrinsic extinction and the redshift is similar; that is they both redden more the blue end of the spectrum. An afterglow at a high redshift and with no intrinsic extinction can look very similar to an afterglow at a lower redshift and with a significant intrinsic extinction. To account for this additional complication, a GRB process runs more than one instance of HyperZ program; without reddening and applying user configurable reddening law, range and step size of extinction.

The cause for multiple HyperZ instances is compounded by the different limiting magnitudes reached by different types of OBs. Since the limiting magnitudes of the filters are input parameters to HyperZ, it has to be re-started every time they change, that is every time the candidates of another type of OB are analyzed. In order to overcome these restarts, a GRB process has multiple instances of HyperZ; each with different input limiting magnitudes corresponding to different types of OBs configured in the system.

Therefore, a GRB process has $2 \times n$ running instances of HyperZ program; 2 to account for intrinsic extinction, times n, to account for n different configured OB types within the system. In this case, a restart may only be forced if the results of data from one (or more) of the detectors are corrupted and needs to be ignored. In this case, the behavior of HyperZ for undetected objects described in item (iii) should be re-set.

To enable HyperZ to fit the redshift correctly it should detect some features in the spectrum, which are redshifted. Two of the obvious features are the Lyman-limit and the Lyman- α absorption. However, GROND only starts to cover the Lyman-limit after redshift of $z = 3.5$. Moreover, at these redshifts neither of these absorption features is prominent. Both Lyman-limit and Lyman- α absorption becomes deeper with increasing redshift, as shown in Figure 2.9. In the case of galaxies, it is easier to determine the redshift via SED fitting, since the galaxy spectra have other significant features like the Balmer-jump or various emission and absorption lines. However, the canonical GRB spectrum is a fea-

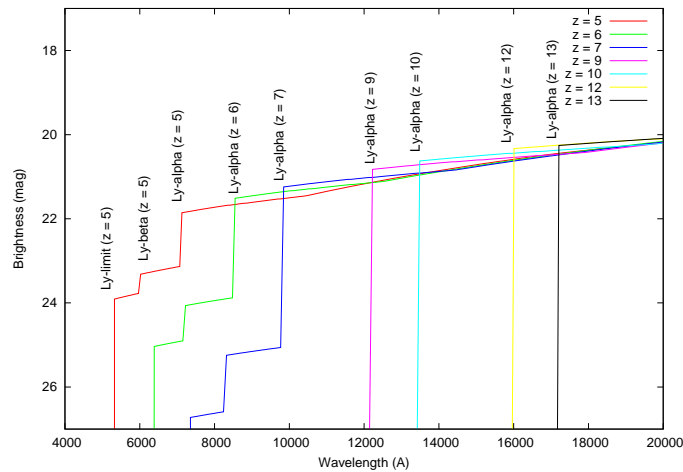


Figure 2.9: The evolution of Lyman absorption features with redshift. The depth of the Ly- α absorption increases so much that the other Lyman absorption features are not even visible after redshift of $z > 7$.

tureless power-law. In this case the only hint for HyperZ to determine the redshift is in the form of the Lyman-limit and Lyman absorption features, which start to appear after $z \sim 3.5$ for GROND observations.

The HyperZ tests we conducted with simulated and real afterglow data showed that HyperZ is able to determine the redshift with an accuracy of $\Delta z \sim 0.3 - 0.5$, if the data covers the Lyman features (see Figure 2.10). However, for the cases where the Lyman features are not covered, i.e. $z < 3.5$ for GROND, HyperZ is not able to determine the redshift of the GRB meaningfully.

Accuracy of the redshift is important for the GP system. Addition of a new module to the GP system is planned, which would generate automated triggers for the 8m ESO/VLT telescopes for further spectroscopic observations of the afterglow. Since we would not like to trigger one of the world’s largest telescopes using the wrong choice of grism because of an incorrect redshift value, we need to have an additional check to the HyperZ results. For this purpose Kiran Garimella wrote a perl-script that fits a single power-law function and a double power-law function (two power laws connected at a point) to the SED of each object, and it applies three tests on the results of these fits in order to decide whether the HyperZ results is trustworthy for that object. The reason for fitting single and double power-law functions is to compare their fit results. The double power-law function is expected to result in a good fit if the SED includes the Lyman-limit or Ly- α absorption features. In this case HyperZ is also expected to provide redshift results with a reasonable accuracy as stated in the previous paragraph. The three tests applied on the fit results are Q-test, χ^2 -test and B-test.

Q-test is applied on the results of the double power-law fit. Q is the probability that the obtained χ^2 will exceed a particular value by chance even for a correct model, for a given

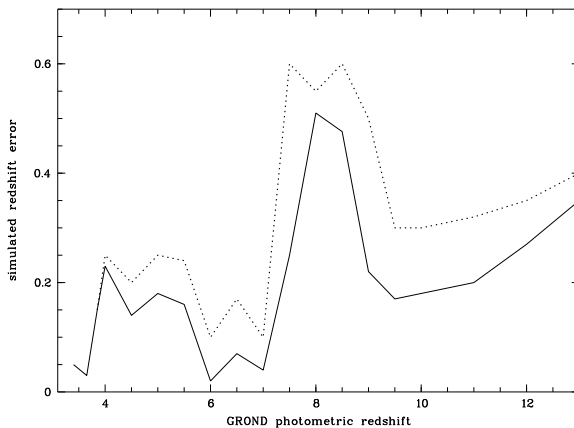


Figure 2.10: The redshift accuracy of HyperZ calculated via tests using real and simulated GRB afterglow data. The solid line shows the simulated error in redshift when assuming ± 0.5 mag relative photometric accuracy between the 7 bands. The dotted line shows the error when in addition one assumes an intrinsic extinction of $A_V = 1$. For low redshifts there is hardly any difference since the near-IR bands provide a precise lever arm. For higher redshifts it gets worse, but the redshift determination remains always possible, because J – K or H – K allow to accurately constrain A_V .

number of degrees of freedom (Press et al. 2002). $Q = 1$ means that the obtained χ^2 is the minimum that can be obtained for that number of degrees of freedom. However, this is usually too good to be true, and can be caused by overestimated observation errors. $Q = 0$ means that the obtained χ^2 is the maximum that can be obtained for that number of degrees of freedom. In other words, the fit is not acceptable. However, low Q values can also be obtained when the observation errors are not normally distributed, which is assumed during the calculation of Q . Taking that into account, the lower limit of acceptable Q values are usually set to be $Q \sim 0.001$. Therefore the double power-law fit passes the Q -test if its Q value is between a user configurable upper and lower limit.

The χ^2 -test compares the χ^2 values of the single and double power law fits. The test is passed if the χ^2 of the double power law fit is smaller than that of the single power law fit to the SED. B-test is applied on the best-fit indices of the double power law fit to the SED. Its aim is to check whether the fitted double power law resembles a broken power law shape of an SED that shows a Lyman-limit break or Ly- α absorption. The index of the power-law fit to the left-handside of the data should be larger than or equal to the index of the power-law fitting to the right-handside of the data multiplied by a user configurable factor. In addition, the index of the power-law fitting to the left-handside of the data should be smaller than or equal to a user configurable limit.

These three tests are applied to fits of the SEDs of all GRB candidates whose redshifts have been calculated by HyperZ. If a candidate passes all three tests, the redshift calculated by HyperZ is regarded as trustworthy and accurate enough. Hence, it is then

safe to automatically trigger the world's largest telescopes to obtain deep spectroscopic observations of that GRB.

2.4 Summary

I have described the GP in terms of its functions related with observation and analysis. The observation related processes are a part of the system layer of GP. These processes include receiving GRB alerts, deciding whether to follow-up the target, scheduling observations for the night, and automating the observations; i.e. initiating, continuing and ending the observations according to the schedule. The system layer also includes a management component, which is a web server to provide user interaction. The processes doing data analysis are contained by the analysis layer. The analysis layer comprises of GRB server processes, which pre-process the images and downloads catalogs to be used during astrometry and photometric calibration, organize the analysis of each observation block, apply photometric analysis on each band of the 7-band data, apply single- and multi-band photometric calibration, identify the afterglow, and determine the redshift of the GRB afterglow. The GP turns GROND into a robotic system by automating both the observations and the data analysis.

3 Nature of the Gamma-ray Burst Progenitors

3.1 Probing the close environment of GRBs through photoionization

The prompt X-ray and the X-ray/UV afterglow emission of GRBs will inevitably photoionize the circumburst material independent of its density. If the circumburst density is high, photoionization will lead to time-dependent (on an hour timescale) absorption (Perna & Loeb 1998) and emission-line features (Böttcher et al. 1999; Ghisellini et al. 1999), such as those claimed to be seen in X-rays. On longer timescales, the GRB photoionization may lead to indicative recombination line features, which allow the identification of remnants of GRBs in nearby galaxies (Band & Hartmann 1992; Perna et al. 2000, PRL in the following).

The near-IR and optical spectra of GRB hosts exhibit redshifted star formation emission lines, like the Lyman and Balmer series, [OII] and [OIII]. Often the Ne III emission line is also observed, indicating high temperatures and ionization levels, presumably related to the presence of hot massive stars.

Photoionization of the ambient medium is well-studied in the case of supernovae, which are the most similar cases to GRBs. For SN 1987A, IUE observations showed that the prominent UV lines started to increase simultaneously after 60–80 days and stayed at a constant level until 400 days after the initial exciting supernova outburst (Fransson et al. 1989). After 400 days most lines decreased quickly and reached the noise level by day 1500 (Sonneborn et al. 1997, see Fig. 3.1). Detailed modelling of the ionization zones and the line emission of the circumstellar gas, performed by (Lundqvist & Fransson 1996), allowed them to constrain the gas density.

In the case of a GRB, ionization by the prompt emission, the afterglow (photon field) and by the blast wave (shock-ionization) will appear in addition to the SN component and will largely dominate. The blast wave is expected to influence the ionization state of the gas on timescales of hundreds to thousands of years after the burst (PRL). Therefore, for the purpose of our analysis, we can safely assume that photoionization is the dominating ionization mechanism. A large fraction of the energy (e.g. kinetic, magnetic) stored in the GRB-jet ($\sim 10^{52}$ erg) is released in the afterglow. The X-ray/UV component of this radiation (with some contribution from the X-ray emission of the prompt phase) is the main responsible for the ionization of the ambient medium. For typical GRB/afterglow

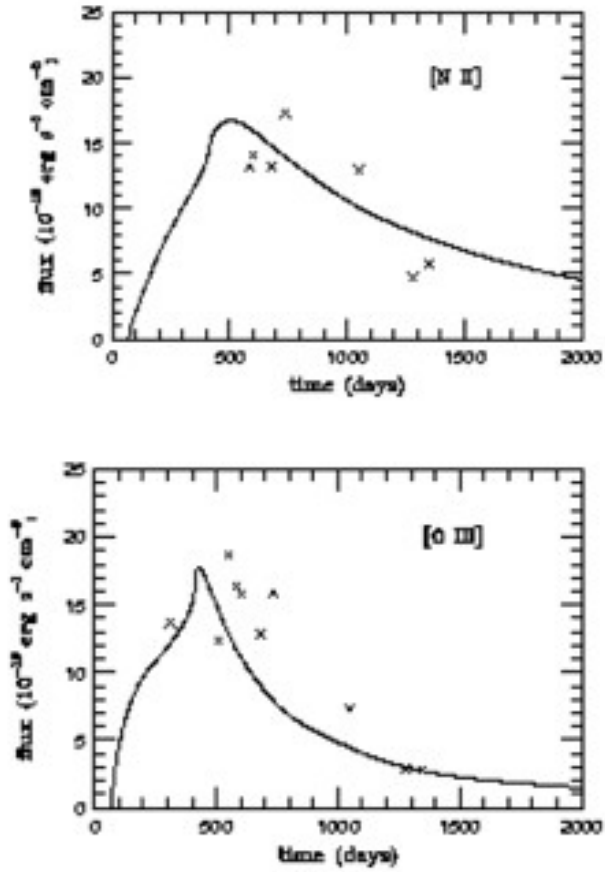


Figure 3.1: Lightcurves of SN 1987A for [NII] (*top panel*) and [OIII] (*bottom panel*) taken from (Lundqvist & Fransson 1996). Crosses represent the data and solid lines represent ionization models from (Lundqvist & Fransson 1996).

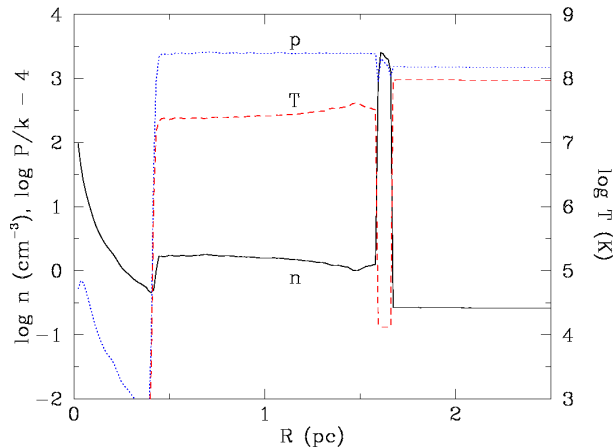


Figure 3.2: Density, temperature and pressure of the circumstellar environment at the end of the Wolf-Rayet stage (Chevalier et al. 2004).

luminosities, the size of the ionized region is on the order of 100 pc for an ISM density of $\sim 1 \text{ cm}^{-3}$ (PRL).

After being ionized, the gas then starts to cool on a timescale

$$t_{\text{cool}} \sim 10^5 (T/10^5 \text{ K}) / (n/\text{cm}^{-3}) \text{ yr} \quad (3.1)$$

where T is the temperature of the gas and n the electron density. Although cooling starts soon after the burst of radiation has passed through the medium, emission from the cooling gas increases during the early times after the GRB. If a region of radius R is heated and ionized by the burst radiation, the maximum emission will occur after a time $t \sim R/c \sim 3 \text{ yr} (R/\text{pc})$, due to light travel times from different parts of the region.

The strength and timescale of the recombination emission depends strongly on the ambient density. While the modelling of the broad-band SED of afterglows has led to densities in the range $1\text{-}10 \text{ cm}^{-3}$, there are also observational indications for much higher densities: (i) observed variable X-ray lines (Watson et al. 2002; Reeves et al. 2003; Frontera et al. 2004) and continuum absorption (Lazzati & Perna 2002) require densities of $\sim 10^5\text{-}10^6 \text{ cm}^{-3}$; (ii) some GRB afterglow data require a dense ($\sim 10^4 \text{ cm}^{-3}$) shell around some nearby low-density media ($1\text{-}10 \text{ cm}^{-3}$) (Chevalier et al. 2004, Fig.3.2). The SN-GRB connection is now clearly proven for four GRBs (Galama et al. 1998; Hjorth et al. 2003; Stanek et al. 2003; Malesani et al. 2004; Pian et al. 2006), indicating the link between long-duration GRBs and deaths of massive stars. Observations of massive, Wolf-Rayet (WR)-like stars, have shown that they lose matter via strong stellar winds. A WR stellar wind, interacting with a circumstellar medium, leads to the formation of a shell (termination shock) whose density and radial extent depend on both the progenitor characteristics (i.e. mass loss rate, wind velocity) as well as the density of the medium (e.g. Fryer et al. 2006).

An ionized shell of, say, density $\sim 10^3 \text{ cm}^{-3}$ and radial extent of a few parsecs, will reach its peak emission on a timescale of a few years (due to the light travel times) and will

cool on a timescale of tens of years. Therefore, the first few years after the burst are crucial for detecting cooling emission from these dense, compact shells produced by the wind termination shocks of the massive stars progenitors of (long) GRBs.

We have written a proposal (075.D-0771(A), PI: A. Küpcü Yoldaş) to re-observe the host galaxies of the GRBs 980703, 990712, 011121, 020405, 030329 and 031203 at 480 – 2555 days after their original outburst using FORS2 spectrograph mounted on ESO/VLT 8m telescope. The aim of the proposal is to search spectroscopically for photo-ionization signatures, since measuring emission lines for each of the hosts allows us to search for a fading of the lines compared to the previously performed VLT and Keck observations and test for different recombination time scales and gas densities. This allows for the first time to test the optical recombination for GRBs on time scales of years.

The proposed GRBs have redshifts smaller than 1 and have observable line fluxes which makes them suitable for high-resolution spectroscopic observations. The outburst dates of these GRBs cover nearly the entire range for which host galaxy observations were performed (1998–2003), thus allowing us to study a wide range of recombination time scales. Comparing the line fluxes obtained from these new observations with those of the previous observations can result in two cases: (i) line fluxes are constant, or (ii) line fluxes are variable. In the first case, either the ionized volume is not sufficiently large enough in order to produce line fluxes comparable to the emission associated with star formation in the host or the density of the circumburst medium is too high (shorter recombination time scale) or too low (longer recombination time scale). Hence, we can only put limits on the density and ionized mass. If the latter case is observed, the line flux originating in the star forming regions of the host galaxy can not simply be separated from the flux produced by the ionization due to the burst. If a line flux is decreasing in comparison to the archival first-epoch observations, the recombination timescale and the light travel time through the shell is smaller than the time difference between the two observations. If, on the contrary, a line flux is increasing, the reverse situation will apply. Thus, already the mere fact of observed variability will constrain the density and the size of the shell.

Our proposal was accepted and spectroscopic observations of the host galaxies of the GRBs 990712, 011121, 020405 and 031203 were obtained in service mode. The first example of this study is GRB 990712 which has the most extended data set spanning 6 years after the burst. The analysis and results of that work is explained in the following section.

3.2 The first example: Constraining the environment of GRB 990712

The energy output in the GRB prompt emission and afterglow phase is expected to photoionize the surrounding medium out to large radii. Cooling of this gas produces line emission, particularly strong in the optical, whose variability is a strong diagnostics of the gas density and geometry in the close environment of the burst. We present the results of a spectral time-series analysis of the host galaxy of GRB 990712 observed up to ~ 6 years

Table 3.1: Log of observations

Date	Instrument	Grism	Coverage (nm)	Exposure time (sec)
14 Jul 1999	FORS1	150I	370 – 770	2400
11 Nov 1999	EFOSC	Gr6	400 – 800	1800
06 Jun 2002	FORS1	600R	525 – 745	4320
17 Jul 2004	FORS2	600RI	512 – 845	2400
05-06 Jul 2005	FORS2	300V	445 – 850	7200

after the burst. We analyze the emission line fluxes, together with those of the previous observations of the same GRB, in search for photoionization signatures. We find that the emission line fluxes show no variation within the uncertainties up to 6 years after the burst, and we use the measured line intensities to set a limit on the density of the gas within a few parsecs of the burst location. This is the first time that emission from cooling GRB remnants is probed on time scales of years. This work has been published in A&A volume 457, page 115 together with co-authors Jochen Greiner and Rosalba Perna, whose contributions were on the initial idea and motivation, and density calculations based on the line fluxes.

3.2.1 GRB 990712

GRB 990712 was discovered by GRBM and WFC onboard BeppoSAX on July 12.69655 UT, 1999. The duration of the burst was 30s and it was first localized by WFC at R.A. = 22:31:50, Dec. = -73:24.4 with an error radius of 2' (Heise et al. 1999). Follow-up observations led to the discovery of the GRB afterglow. The redshift of the burst is $z=0.433$ (Vreeswijk et al. 2001a). Two different groups have found evidence for a SN bump from the optical lightcurve of the afterglow (Björnsson et al. 2001; Zeh et al. 2004). The BeppoSAX spectra of the prompt emission indicated a temporal emission feature located around 4.5 keV, which can be fit either with a Gaussian profile with a rest-frame energy of around 6.4 keV, which is consistent with an iron line, or with a blackbody spectrum with $kT \sim 1.3$ keV (Frontera et al. 2001). Since the iron line interpretation requires a very high density environment that would obscure the afterglow, Frontera et al. (2001) prefer the thermal component interpretation that can be accounted for by the fireball model.

The host galaxy of GRB 990712 is one of the brightest GRB host galaxies, with $V = 22.3$ mag and $R = 21.8$ mag (Sahu et al. 2000).

3.2.2 Data Reduction and Analysis

We obtained spectra of GRB 990712 on July 5 and 6, 2005, approximately 6 years after the GRB, using VLT/FORS2 under good seeing conditions ($\sim 0''.6$). The 300V/GG435 grism/filter was used with a slit width of $1''.0$. The total exposure time was 2 hours (4×30

minutes). The master bias files are created using images with the same chip binning and read-out settings as of the spectra. The master flat-field files are created similarly using images obtained with the same grism/filter and slit settings as of the spectra. The master flat-field images are then normalized. The spectra were reduced with the steps of bias and flat-field correction, and cleaned from cosmic rays using standard IRAF routines.

The spectra were calibrated using standard star G158-100 observed on July 5, 2005 with the same grism/filter and a slit width of $5''0$. The largest slit width is chosen for the standard star observation because usually the standard stars are bright and therefore their emission overfills narrower filters. In that case the flux of the standard star is underestimated leading to a wrong flux calibration. The flux calibration was further validated by folding the spectrum with the FORS R-band filter curve and comparing the obtained magnitude with that of the host galaxy given in Christensen et al. (2004a). We corrected the spectra for foreground extinction of $E(B - V) = 0.03$ (Schlegel et al. 1998). The line fluxes were determined by fitting a Gaussian to the line using the SPLIT task of IRAF. The continuum level was determined locally.

The line fluxes are compared with those derived using VLT archival data of observations obtained on July 14, 1999 (PI: Galama), November 11, 1999 (PI: Courbin), June 6, 2002 (PI: Mirabel) and on July 17, 2004 (PI: Le Floc'h) (see Tab.3.1). The spectra were treated in an identical way and calibrated using standard stars EG 274 (Sep 15, 1999), LTT 377 (at Dec 6, 1999 and at Jul 15, 2004), and LTT 3854 (Jun 05, 2002) for July 1999, November 1999, July 2004 and June 2002 data, respectively. Note that we used standard star observations obtained 2 months later for July 1999 data, and 25 days later for November 1999 data. This is due to the fact that there are no standard star observations obtained at a closer time to the original observations and also satisfies the two necessary conditions to be used as a standard star for flux calibration, i) having the same grism/filter settings with the corresponding science observations, and ii) having a large enough slit width ($5''0$) to enclose all the emission from this bright standard star. All the flux calibrations were further validated. For July 1999 data, the continuum level was compared with the afterglow brightness at that time, given for three filters V, R and I in Sahu et al. (2000). The flux values we obtain are consistent with the published values obtained by flux calibrating the same data using the afterglow brightness extrapolated in time (Vreeswijk et al. 2001a). The previously unpublished 2002 and 2004 fluxes were similarly validated by comparing the magnitude obtained by folding the spectrum, with that of the host galaxy given in Christensen et al. (2004a), as in the case of 2005 spectra. The line fluxes are shown in Table 3.2. The flux errors in Table 3.2 only include the uncertainties in the continuum level. The estimated error in the flux calibration is about 10% for all data. Figure 3.3 shows all five spectra from July 1999 to July 2005.

All of the observed lines, which are [O II], [Ne III], $H\gamma$, $H\beta$ and [O III] ($\lambda\lambda 4959, 5007$) lines, are observed to have constant fluxes over ~ 6 years after the burst (see Fig.3.4). To overcome the difficulty of comparing line fluxes from different spectra obtained with different settings, i.e. instrument, grism, night conditions etc., we derive our results on the circumburst environment based particularly on the [O III] $\lambda 5007$ and the $H\beta$ lines.

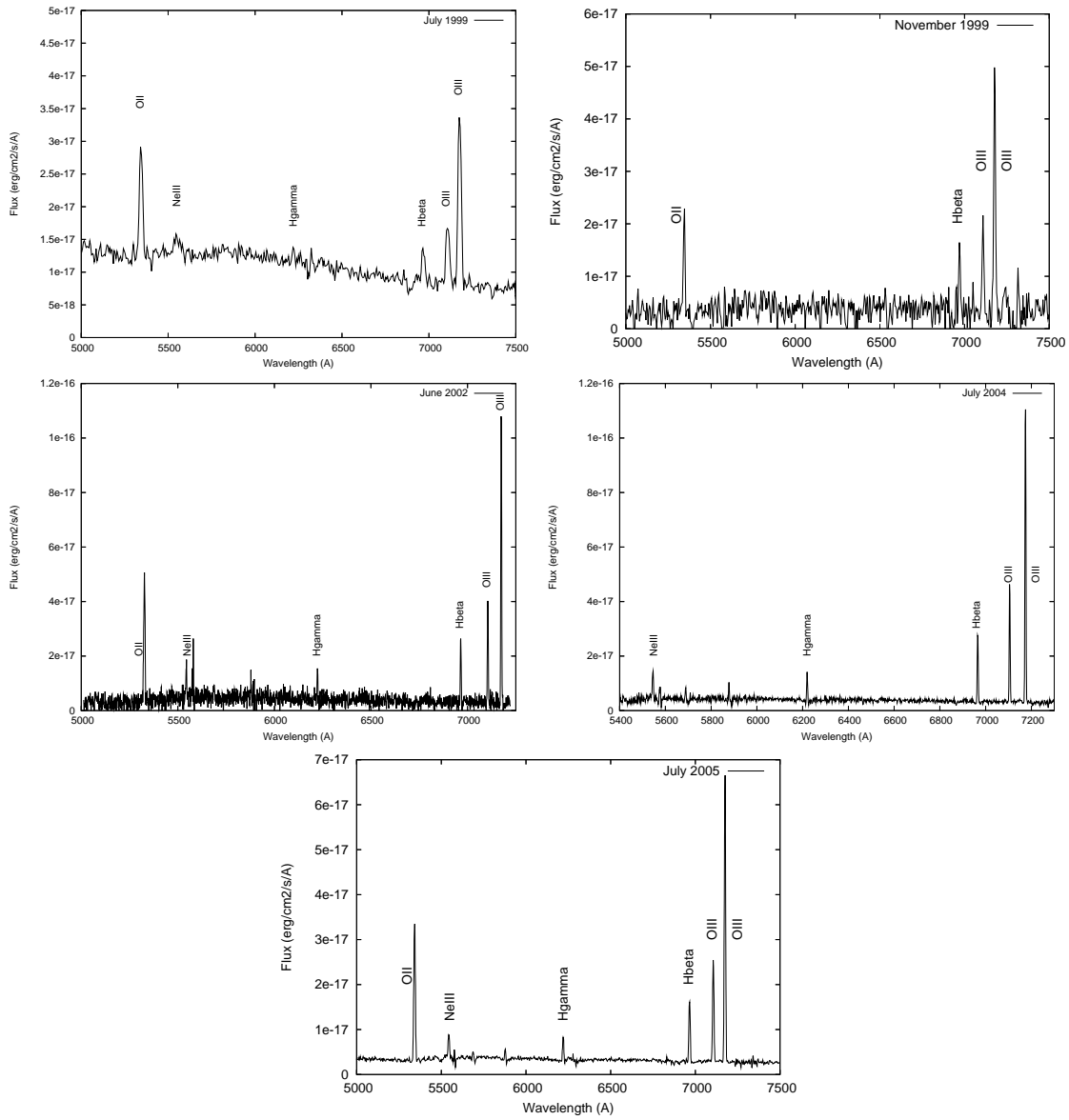
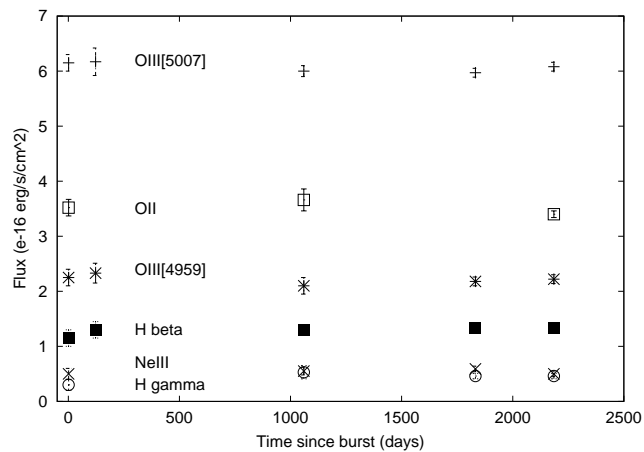


Figure 3.3: Spectra of the host galaxy of GRB 990712 obtained in July 1999, November 1999, June 2002, July 2004 and July 2005, respectively.

Table 3.2: Emission line fluxes

Line	Flux (10^{-16} erg s $^{-1}$ cm $^{-2}$)				
	at day 1.5	at day 123	at day 1060	at day 1832	at day 2185
[O II](λ 3727)	3.52 \pm 0.15		3.66 \pm 0.20		3.40 \pm 0.60
[NeIII](λ 3869)	0.5 \pm 0.1		0.55 \pm 0.07	0.59 \pm 0.05	0.50 \pm 0.05
H γ (λ 4340)	0.3 \pm 0.1		0.53 \pm 0.12	0.46 \pm 0.05	0.46 \pm 0.05
H β (λ 4861)	1.15 \pm 0.15	1.30 \pm 0.15	1.29 \pm 0.09	1.34 \pm 0.04	1.33 \pm 0.05
[OIII](λ 4959)	2.25 \pm 0.15	2.33 \pm 0.18	2.10 \pm 0.15	2.18 \pm 0.08	2.22 \pm 0.08
[OIII](λ 5007)	6.15 \pm 0.15	6.17 \pm 0.25	6.00 \pm 0.10	5.97 \pm 0.08	6.08 \pm 0.08

**Figure 3.4:** [Ne III], H γ , H β , [O II] and [O III] 4959, 5007 line flux light curves for GRB 990712. Error bars are smaller than the symbol size, if not visible.

These are close enough in wavelength space to overcome the possible effects of different flux calibrations, and at the same time, as discussed below, they are especially strong discriminators of photoionization vs. collisional ionization.

3.2.3 The circumburst environment

A distinctive signature of photoionized gas is a high [O III] $\lambda 5007/H\beta$ ratio ($\gtrsim 5$), which is not generally produced in steady shocks for solar abundances (Shull & McKee 1979). This ratio increases with the ionization parameter and, for typical X-ray/UV photoionizing fluxes of GRBs and their afterglows, it reaches a value on the order of 100 (PRL). Our observations at about 6 years after the burst, as well as the previous ones at earlier times, show that [O III] $\lambda 5007/H\beta \sim 4.6$ in the host of GRB 990712. Combined with the log ([O II]/ $H\beta$) value of 0.4 ± 0.1 , this value is rather typical of an HII galaxy, as can be seen by comparison with the sample of emission line galaxies at redshifts $0 \lesssim z \lesssim 0.3$ from the Canada-France redshift survey (Rola et al. 1997; see also Vreeswijk et al. 2001a). Therefore, the constraints that we are able to put on the close environment of GRB 990712 can be derived from the lack of contribution from photoionized gas to the brightest expected line ([O III] $\lambda 5007$) from the cooling gas, within the observational uncertainties. The measured flux of this line is $\sim 6 \times 10^{-16}$ erg/s/cm² to within $\sim 10\%$ uncertainty (see Table 2). At a redshift of 0.433, this flux corresponds to a luminosity of $\sim 3.8 \times 10^{41}$ erg/s for a LCDM cosmology with Hubble parameter $h=0.73$ (Spergel et al. 2006). Since the luminosity is constant to within the 10% uncertainty value of $\sim 3 \times 10^{40}$ erg/s, the contribution from the cooling GRB remnant cannot be larger than this value at any given time during the observation window.

Numerical simulations of cooling GRB remnants (PRL) show that the radiation flux from a typical GRB and its afterglow ionizes a region on the order of ~ 100 pc for an ISM density of ~ 1 cm⁻³. For a gas of solar metallicity, the corresponding luminosity of the [O III] $\lambda 5007$ line from the cooling gas is found to reach a value of $\sim 10^{38}$ erg s⁻¹ over a time $t_{\text{cool}} \sim$ a few $\times 10^4$ yr (see Fig.3 in PRL; the details of the computation of the cooling radiation can also be found in PRL). The brightness of the line scales with $n n_e$, where n_e is the electron density. For a gas metallicity not too far from solar (so that the particle number is dominated by H) and a highly ionized gas, one has $n_e \sim n$, and the line luminosity can be scaled, to a first approximation, as¹ $\sim 10^{38}(n/\text{cm}^{-3})^2 (R_e/100 \text{ pc})^3$ erg s⁻¹.

Our observations, up to 6 years after the burst, allow us to probe an emitting region, R_e , of at most 2 pc in size, due to light delay effects, as discussed in subsection 3.1. Since no flux variation has been observed within the 10% flux error (corresponding to a luminosity of about 3×10^{40} erg s⁻¹), we deduce that the line luminosity due to the cooling gas has

¹Note however that, as the density increases, the maximum size of the region that can be ionized will decrease. Furthermore, note that the details of the rise time also depend on the extent of the beaming of the ionizing radiation, but we do not worry about secondary effects here since the data only allow us to set upper limits.

to be below this level, i.e.

$$L_{5007} \sim 10^{38} (n/\text{cm}^{-3})^2 (R_e/100 \text{ pc})^3 \text{erg s}^{-1} \lesssim 3 \times 10^{40} \text{erg s}^{-1} \quad (3.2)$$

which yields the limit on the density $n \lesssim 6 \times 10^3 \text{ cm}^{-3}$ for $R_e = 2 \text{ pc}$.

This limit can be used to constrain the range of allowed parameters for the GRB host and ISM densities. For example, Fryer et al. (2006) find that, for a progenitor star with mass loss $\dot{M} = 10^{-5} M_\odot \text{ yr}^{-1}$ and wind velocity $\sim 1000 \text{ km/s}$, expanding in a medium of density in the range $\sim 10^3 - 10^4 \text{ cm}^{-3}$, the inner radius of the shell is on the order of tenths of a parsec, and the outer radius is $> 2 \text{ pc}$ (with the shell density being on the order of the ISM density). These high shell densities, filling a region up to the observed emitting volume of $\sim 2 \text{ pc}$, are not favored by our observations, since they would likely result in a variable [O III] $\lambda 5007$ flux over the 6 years of observations. On the other hand, termination-shock shells produced from the impact of the wind with a lower-density medium are consistent with this lack of variability. Also note that, given the 6 year timescale of the observations, termination shocks located at distances $\gtrsim 2 \text{ pc}$ cannot be ruled out by the currently available data.

Generally speaking, observations at longer timescales allow one to probe shell termination shocks over a wider range of distances from the GRB progenitor star. However, since more distant termination shocks are generally associated with lower ISM densities (and hence a lower luminosity of the [O III] $\lambda 5007$ line), in order to separate the eventual contribution of this line due to the cooling gas in the close GRB environment, from that due to the host galaxy itself, a higher signal-to-noise ratio in the observations as well as a consistent set of observations (i.e. observations obtained with the same instrument and settings) is necessary.

3.2.4 Star formation rate and metallicity

The star formation rate (SFR) of the host galaxy of GRB 990712 has been previously calculated based on radio non-detection limit, line fluxes and ultra-violet flux (Hjorth et al. 2000; Vreeswijk et al. 2001a,b; Christensen et al. 2004a). In particular, Vreeswijk et al. (2001a,b) derived the SFR both from the [O II] line emission ($2.7 \pm 0.8 M_\odot/\text{yr}$) and from the radio non-detection ($< 100 M_\odot/\text{yr}$), and compared them after correcting the SFR_{OII} for the intrinsic extinction derived using the $\text{H}\gamma/\text{H}\beta$ ratio.

Using the line fluxes of our July 2005 spectrum and the same method used by Vreeswijk et al. (2001a), we calculated $\text{SFR}_{OII} = 2.8_{-0.9}^{+0.4} M_\odot/\text{yr}$ and $A_V = 1.7_{-0.8}^{+0.9} \text{ mag}$ based on the $\text{H}\gamma/\text{H}\beta$ ratio. Our A_V value is on average lower than the $A_V = 3.4_{-1.7}^{+2.4}$ derived by Vreeswijk et al. (Vreeswijk et al. (2001a)), therefore our extinction corrected SFR value ($\text{SFR}_{OIIcorr} = 10_{-6}^{+15} M_\odot/\text{yr}$) is also lower than their calculation. Nonetheless both A_V and the extinction corrected SFR are in agreement with Vreeswijk et al. (2001a,b) values within the errors.

We did not detect the [O III] $\lambda 4363$ line that is necessary to determine the electron temperature T_e by means of lines (like [O III], [Ne III], etc.) from high ionization-zone

elements. Therefore, we cannot estimate the oxygen and neon abundance based on the electron temperature. However, we can still estimate the oxygen abundance based on the ratio $R_{32} = ([\text{OII}]\lambda 3727 + [\text{OIII}]\lambda\lambda 4959, 5007)/H\beta$. Kewley & Dopita (2002) suggest using the relation given by Zaritsky et al. (1994) to obtain an estimate of the oxygen abundance. Using the formulae given in Zaritsky et al. (1994), we obtain $\log(\text{O}/\text{H}) = -3.7 \pm 0.1$. However, that formula is calibrated for metal rich galaxies and overestimates the metallicity for values of $\log(\text{O}/\text{H}) < -3.5$ (see Kobulnicky et al. 1999, Kewley & Dopita 2002). Therefore we used Eq. (16) in Kobulnicky & Kewley (2004), which is adapted from the relation given by Kewley & Dopita (2002) and parameterized for the lower metallicity branch ($\log(\text{O}/\text{H}) < -3.6$). The result is $\log(\text{O}/\text{H}) = -3.7 \pm 0.1$, which is the same as our initial estimate using the relation given by Zaritsky et al. (1994). Similarly, Vreeswijk et al. (2001a) obtained -3.7 ± 0.4 for $\log(\text{O}/\text{H})$, which agrees with our estimate. The oxygen abundance we obtained is just a bit lower than the solar value ($\log(\text{O}/\text{H}) = -3.34$; e.g. Asplund et al. 2000). Therefore our assumption that the metallicity of the gas near the GRB is not far from solar is reasonable in our derivation of the [O III] line luminosity of the cooling gas.

It should be noted that, in the context of GRBs, studying the photoionization signatures of cooling gas not only helps in understanding the nature of the GRB progenitor star, but it also helps reduce possible biases in the determinations of two important properties of the GRB host galaxy, such as the SFR and the metallicity. In fact, SFR and metallicity calculations based on emission lines generally rely on observations obtained at a single epoch. However, in order to properly assess the possible level of contamination by the cooling GRB remnant, multiple epochs of observations spanned over a long timescale are necessary.

3.2.5 Summary

We have presented the results of the spectral analysis of the host galaxy of GRB 990712. With the last set of observations taken about 6 years after the burst, this is the longest time coverage for a GRB host galaxy to date. Though we do not detect line variations, timescales of a few years are important for detecting cooling radiation from the heated shells produced by the wind termination shocks of the massive star progenitors of the GRBs. For the case of the GRB 990712 host, the lack of time variability in the [O III] $\lambda 5007$ line, combined with the $\lesssim 5$ ratio of the [O III] $\lambda 5007/H\beta$ lines, has allowed us to set an upper limit to the contribution from the cooling gas. This limit, in turn, could be used to constrain the allowed range of densities within a region of about 2 pc surrounding the burst. We have therefore shown how this type of observation provides a useful complement to the studies of the close environment of GRB progenitors and, therefore, can help reconstruct the characteristics of the GRB progenitor star.

Finally, we have pointed out how, if a substantial contamination to the galaxy spectra is provided by the GRB cooling radiation, inferences of the SFR and metallicity that are drawn from measurements of line ratios can be biased. To be able to assess the degree of

this contamination, long-term monitoring of the GRB host galaxies is necessary.

4 Host Galaxies – An interesting case study: The Host Galaxy of GRB 011121

We present a detailed study of the host galaxy of GRB 011121 (at $z = 0.36$) based on high-resolution imaging in 5 broad-band, optical and near-infrared filters with HST and VLT/ISAAC. This work has been done in collaboration with 5 co-authors and submitted to *Astronomy & Astrophysics*. The following contributions were made to the data analysis: Daniele Pierini on the modelling and fitting of the population synthesis and radiative transfer models, and Mara Salvato on the introduction of the usage of the morphological analysis program *Galfit*. In addition, Jochen Greiner, Elena Pian and Arne Rau contributed to discussions on the analysis methods and results.

4.1 GRB 011121

GRB 011121 was detected by the Gamma-ray Burst Monitor/Wide-field Camera on board *BeppoSAX* on 2001 November 21, 18:47:21 UT (Piro 2001). Piro et al. (2005) suggested that there is absorbing gas associated with a star-forming region within a few parsec around the burst in connection with a decreasing column density from $N_H = 7 \pm 2 \times 10^{22} \text{ cm}^{-2}$ to zero during the early phase of the prompt emission. The optical/near-IR afterglow was discovered independently by several groups (e.g., Wyrzykowski et al. 2001; Greiner et al. 2001). Further observations revealed excess emission in the light curve associated with a supernova (Bloom et al. 2002b; Price et al. 2002; Garnavich et al. 2003; Greiner et al. 2003). The optical and X-ray data of the afterglow favor a wind environment instead of a steady interstellar medium (Greiner et al. 2003, Piro et al. 2005). The spectroscopic redshift of GRB 011121 is $z=0.362$ from Greiner et al. (2003) which was determined by fitting the strong host emission lines, i.e. $H\alpha$, $H\beta$, [OII], [OIII], underlying the spectrum of the afterglow.

The host galaxy of GRB 011121 is one of the most extensively and deeply imaged hosts. High resolution images are available in optical and near-IR filters covering the rest-frame wavelength range of $\sim 3200 - 8000$. This gives us the unique possibility to study the host galaxy properties through the parameter space from morphology to stellar mass.

Here we present the morphological and spectral energy distribution analysis of the host galaxy of GRB 011121 using archival HST/WFPC2 and VLT/ISAAC data. In Sections 2, 3 and 4 we present the data reduction, morphological analysis and the photometry of this galaxy, respectively. In Sect. 5 we analyse the spectral energy distribution of the

host galaxy and derive properties of the stellar population and the interstellar medium (ISM). In Sect. 6 we calculate the star formation rate and specific star formation rate and compare the values with other galaxies. Finally, we summarize our results in Sect. 7.

We adopt $\Omega_\Lambda = 0.7$, $\Omega_M = 0.3$ and $H_0 = 65 \text{ km s}^{-1} \text{ Mpc}^{-1}$ throughout this paper. The luminosity distance at the redshift of the host ($z = 0.362$) is $D_L = 2080.2 \text{ Mpc}$, and 1 arcsecond corresponds to 5.43 kpc.

4.2 Data reduction

Imaging of the field of GRB 011121 has been performed at many epochs. For the present analysis we have chosen the data acquired by the HST Wide Field Planetary Camera 2 (WFPC2) and the VLT Infrared Spectrometer And Array Camera (ISAAC), sufficiently late after the GRB so that the afterglow does not contribute significantly to the brightness of the host galaxy. The HST data were acquired approximately 5 months after the burst, using 4 filters: F450W, F555W, F702W and F814W (see Tab.4.1). These data were obtained as a part of a large program (ID: 9180, PI: Kulkarni) intended to probe the environment of GRBs. The total exposure time in each filter is 4500 seconds. An independent analysis of these data has been published in Bloom et al. (2002b), concentrating on the supernova signature underlying the afterglow lightcurve.

The HST imaging data were pre-processed via “on the fly” calibration, i.e. with the best bias, dark, and flat-field available at the time of retrieval from the archive. The Wide Field (WF) chips of WFPC2 have a pixel scale of $0''.1/\text{pixel}$. The images for each filter were dithered by subpixel offsets (resulting in a pixel scale of $0''.05/\text{pixel}$) using the IRAF/Dither2 package to remove cosmic rays and produce a better-sampled final image. For all HST observations, the host position falls near the serial readout register of WF chip 3 which minimizes the correction for charge transfer efficiency (CTE) to around 5 per cent in count rate, therefore we ignore the CTE correction for the photometry.

The VLT/ISAAC data were obtained in the J_s -band on February 9, 2002 with an exposure of 1800 seconds (see Tab.4.1), and reported earlier in Greiner et al. (2003). These data were also obtained as a part of a large program (ID: 165H.-0464, PI: van den Heuvel) intended to understand the physics of GRBs and the nature of their hosts. The J_s -band images were reduced using the ESO Eclipse package (Devillard 2005).

Zero-point magnitudes for the HST filters were taken from Dolphin (2000)¹. For the VLT images, two local photometric standard stars given by Greiner et al. (2003) were used to obtain the photometric calibration. Both for the HST and the VLT data, the background values of the images were calculated using IRAF/*imexamine* in the corresponding filters. The 1σ surface brightness limits are calculated using the formula given by Temporin (2001):

$$\mu_{lim} = -2.5 \times \log[\sigma/(t \times s^2)] + \mu_0 \quad (4.1)$$

¹see also http://purcell.as.arizona.edu/wfpc2_calib/

Table 4.1: Log of observations and morphological parameters

Filter	Date	Tele/Instr	Exposure sec	Sersic index n	Effective radius kpc	Position angle degree	Ellipticity ¹
F450W	2002-04-21 (day 161)	HST/WFPC2	4500	2.1±0.3	7.4±1.4	30.7±2.9	0.52±0.03
F555W	2002-05-02 (day 172)	HST/WFPC2	4500	1.8±0.1	7.2±0.5	31.6±7.5	0.13±0.02
F702W	2002-04-29 (day 169)	HST/WFPC2	4500	2.7±0.1	9.3±0.6	27.5±3.0	0.15±0.01
F814W	2002-04-29 (day 169)	HST/WFPC2	4500	2.4±0.1	7.6±0.5	20.6±4.8	0.13±0.02
J _s	2002-02-09 (day 90)	VLT/ISAAC	1800	1.0±0.5	3.9±2.2	19 ²	0.12 ³

¹ Defined as $1 - (\text{semi-minor-axis}/\text{semi-major-axis})$.

² The best-fit position angle value with an upper limit of 135° .

³ The best-fit ellipticity value with an upper limit of 0.42.

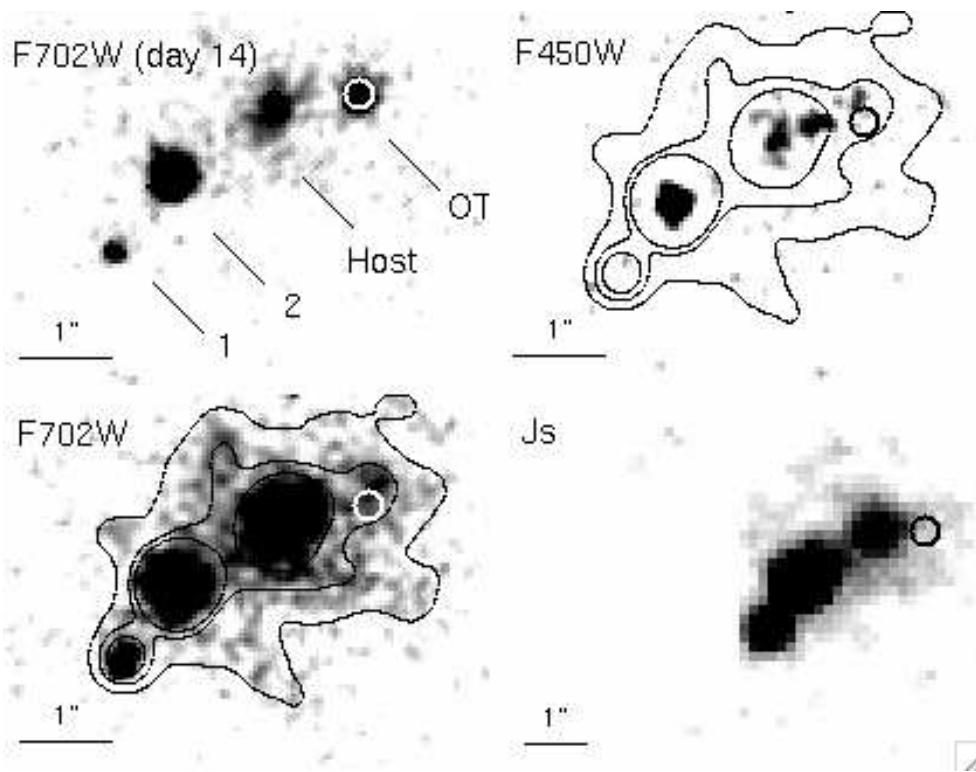


Figure 4.1: *Top left:* F702W image taken ~ 14 days after the GRB. Two foreground stars, the positions of the host, and of the optical afterglow (circle in all panels) are indicated. *Top right and Bottom left:* F450W and F702W images taken ~ 5 months post-burst. The contours show the light distribution in the F702W filter. *Bottom right:* J_s image taken 3 months after the burst. All images are tophat smoothed. North is up and East is to the left. The scale of $1''$ is indicated for all images.

where σ is the standard deviation from the mean of the background, μ_0 is the zero-point, t is the exposure time in seconds and s is the pixel scale.

4.2.1 Astrometry

Images obtained at different epochs and different filters were registered relatively to an early F702W image where the optical transient (OT) is clearly visible (top left image of Figure 4.1), using standard MIDAS routines. We used at least three isolated stars to find the relative shift and rotation of two images. The centers of the stars were computed assuming a point source. We did not re-scale the images since the HST images have the same scale. The estimated accuracy of our relative astrometry is 10 milliarcseconds given by the rms error of the mapping using MIDAS routines. We note that the uncertainties due to optical distortion for the HST images are rather small and are largely removed by the dithering process (Fruchter & Hook 2002). The relative position of the OT in the J_s – band, as shown in the bottom right image of Figure 4.1, is similarly estimated using an early VLT/ISAAC J_s – band image from Nov 24, 2001 (see Greiner et al. 2003), with an rms of 30 mas.

4.2.2 Extinction

It is necessary to correct the brightness values of the host galaxy for Galactic extinction. The study of Schlegel et al. (1998), based on COBE and IRAS extinction maps, gives a value of Galactic reddening along the line of sight of GRB 011121 equal to $E(B - V) = 0.49$ mag. However, different authors have argued that extinction estimates based on far-IR measurements overpredict the true value by about 30% (Dutra et al. 2003; Cambr esy et al. 2005). In particular, Dutra et al. (2003) recommend to scale the value of $E(B - V)$ given by Schlegel et al. (1998) by a factor of 0.75 for lines of sight corresponding to regions with $|b| < 25^\circ$ and $E(B - V) > 0.25$ mag. This holds for the line of sight of GRB 011121, hence we assume $E(B - V) = 0.37$ mag as the correct value of Galactic reddening. This value corresponds to a V-band extinction $A_V = 1.15$ mag using the standard Galactic extinction curve of Cardelli et al. (1989), where $R = A_V/E(B - V) = 3.1$. We correct the observed photometry of the host-galaxy of GRB 011121 for Galactic extinction according to this law.

Garnavich et al. (2003) estimated $E(B - V) = 0.43 \pm 0.07$ mag, and Price et al. (2002) estimated $A_V = 1.16 \pm 0.25$ mag for the *total* (i.e. Galactic plus internal) reddening, both from the broad-band spectral energy distribution of the OT of GRB 011121. These two analyses offer consistent results as for the *total* extinction and reddening, within the uncertainties. However, note that these authors implicitly assumed that the solution of radiative transfer for the light through the host-galaxy of GRB 011121 is the same as for the light from a star in the Galaxy.

Our assumed values of Galactic reddening and extinction are consistent with the previous *total* values, within 1σ . However, we do not conclude that the extinction produced by dust

in the host-galaxy of GRB 011121 is negligible. In fact, the optical spectra of two slightly different regions (due to different slit widths) containing the OT of GRB 011121, taken by Greiner et al. (2003) 4 and 21 days after the GRB event, give values of the Balmer-line flux ratio H_α/H_β equal to $4.8_{-1.1}^{+1.6}$ and $6.4_{-1.9}^{+3.5}$, respectively, after correcting the line fluxes for foreground extinction. Both Balmer-line flux ratios derived from Greiner et al. (2003) are higher (by $> 2 \sigma$) than the value of 2.86 predicted for the standard case B recombination² (e.g. Osterbrock 1989) and implies an A_V of $1.6_{-0.8}^{+0.9}$ and $2.5_{-1.9}^{+1.4}$, respectively, derived using the extinction curve of Cardelli et al. (1989). Higher than predicted Balmer-line flux ratios are due to dust present in the small-/large-scale environment of H II regions (Cox & Mathews 1969; Mathis 1970). Hence the presence of a non-negligible amount of dust extinction in the host-galaxy of GRB 011121 is a feasible working hypothesis.

4.3 Morphology of the host galaxy

The high-resolution data in 5 broad-band filters allow a colour-resolved morphological analysis. Figure 4.1 and Figure 4.2 show images of the host galaxy of GRB 011121 in all five filters. This galaxy exhibits a different structure in the F450W band compared to the redder band data (see Fig. 4.2). In the F702W image we see a nearly face-on extended structure. On the other hand, the F450W image – despite the lower sensitivity – reveals three emission regions, most probably indicating the sites of enhanced star formation in the galaxy, considering that the size of a star forming region (\sim few pc) is much smaller than the sizes of these blue emission regions (\sim 1-2 kpc). The difference of morphology in different filters is reflected in the F450W – F702W color image of the galaxy (see Fig. 4.3). The center of the galaxy is red with $F450W - F702W = 3.0 \pm 0.1$ mag, the background value being $F450W - F702W = 0.2 \pm 0.2$ mag. The three emission regions seen in the F450W filter exhibit $F450W - F702W$ equal to 2.6 ± 0.1 mag, 1.5 ± 0.1 mag and 0.95 ± 0.15 mag, respectively.

The morphological analysis of the host galaxy of GRB 011121 was performed using *Galfit* (Peng et al. 2002). *Galfit* is a 2D galaxy and point-source fitting algorithm which can fit an image with multiple analytical models simultaneously. An initial model assuming a classical de Vaucouleurs bulge+exponential disk profile did not provide a good representation for the host galaxy of GRB 011121. Therefore, we made use of a Sersic profile (Sersic 1968) which can be represented as following:

$$\Sigma(r) = \Sigma_e \exp(-\kappa((r/r_e)^{1/n} - 1)). \quad (4.2)$$

Σ_e is the surface brightness at the effective radius r_e which is the radius containing half of the galaxy flux. The parameter n is the Sersic index that determines the steepness of

²Although the blast wave of the GRB may cause shock-ionization, Perna et al. 2000 showed that it is expected to influence the ionization state of the gas on timescales of hundreds to thousands of years after the burst. Therefore we take the case B recombination as representative of the dust-free case, and assume that the photo-ionization effect of GRB prompt and afterglow emission on the circumburst environment is negligible (see Küpcü Yoldaş et al. 2006).

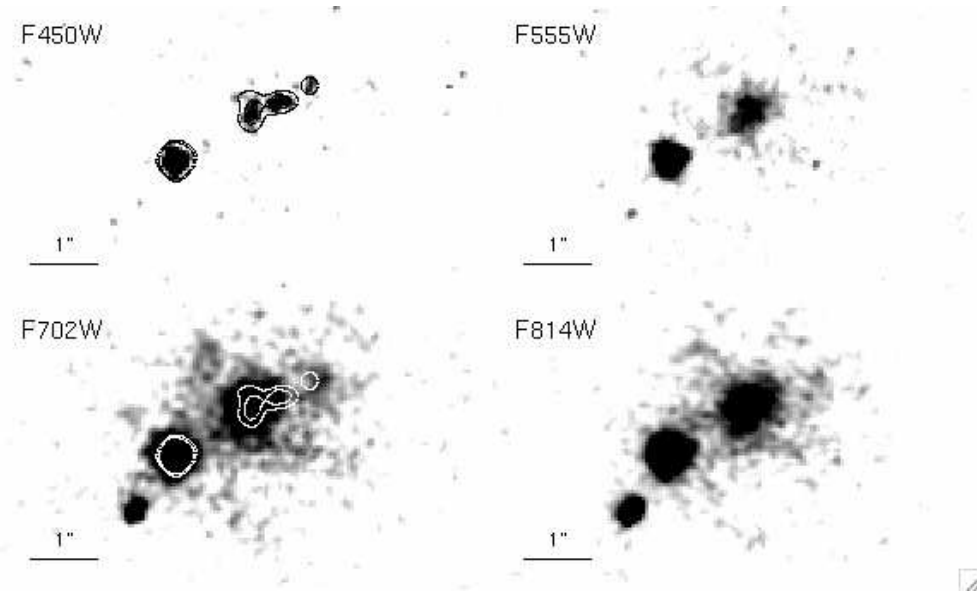


Figure 4.2: F450W (*top left*), F555W (*top right*), F702W (*bottom left*) and F814W (*bottom right*) images of the field of GRB 011121 taken ~ 5 months post-burst. The contours displayed on the top left and bottom left images show the light distribution in the F450W filter. All images are smoothed. North is up and East is to the left.

the profile. An example special case is the classical de Vaucouleurs profile which can be obtained by setting $n = 4$ and $\kappa = 7.67$. For our Sersic profile fit, all the related parameters (i.e. effective radius, Sersic index, position angle) were left free. The top panel of Figure 4.5 shows the image of the field of the host galaxy in the F814W band, and the residual image after the subtraction of the galaxy model. The results of the best fits obtained with *Galfit* for each filter are listed in Table 4.1.

The best-fit values for ellipticity and position angle are in agreement with each other for all filters, except the ellipticity for the F450W filter (see the bottom panel of Fig. 4.5). There is a similar agreement for the effective radius and the Sersic index parameters. We note that the values for the F450W fit should be evaluated carefully, considering that the galaxy image has a relatively lower signal-to-noise ratio due to the sensitivity of the detector and therefore probably probes only the high surface brightness regions. Nevertheless, the values except the ellipticity are still in agreement for all images, indicating that we actually trace the profile of the galaxy in a representative way.

Galaxies at cosmological redshifts are commonly classified according to their Sersic index as disk systems ($n < 2$) and bulge-dominated systems ($n > 2$, see Ravindranath et al. 2004). However, we note that a central, dust-enshrouded starburst can produce a Sersic profile with index of about 2 and a redder F450W – F702W colour in the inner region of a disk system as seen for the host of GRB 011121 (see Fig.4.3). The detection of a

bulge can be hindered by the fact that the galaxy is observed nearly face-on, the best-fit ellipticity value being 0.13 (0.50 for F450W). Although the Sersic index of our reddest band data (J_s -band) is consistent with values typical of a disk-dominated galaxy, this is still consistent with an extended disk structure dominating a small, unresolved bulge, since the spatial resolution of the J_s -band image is almost three times worse than that of the HST images. We also inspected the $F555W - J_s$ radial colour profile and found that it is constant within the errors, indicating that there is no significant difference in the radial profile of the galaxy in different filters except for F450W. Therefore, the host galaxy of GRB011121 can be either a disk system with a small bulge as also indicated by the enhanced traces of spiral arms in Figure 4.4, i.e. an Sbc-like galaxy, or a disk system experiencing dust-enshrouded starburst activity in its central regions.

Similar results on the morphology of the host galaxy of GRB011121 were obtained by two other groups using different methods. Wainwright et al. (2005) performed a morphological analysis using *Galfit* on the same HST data as used here plus the F850L filter data; they concluded that the galaxy is a disk system. Our results are generally in agreement with those of Wainwright et al. (2005), except for the F450W filter, for which there is a $\sim 4\sigma$ difference in the effective radius. Note that we cannot quantify the difference since Wainwright et al. did not quote any errors for their results. On the other hand, also Conselice et al. (2005) performed a morphological analysis based on the concentration and asymmetry parameters using the F702W filter data taken ~ 3 months after the GRB. They concluded that the host is probably a late-type spiral consistent with our results.

The OT of GRB011121 was clearly distinguishable in earlier images taken with HST/WFPC2 since it is located in the outskirts of its host galaxy (top left image of Fig.4.1). None of the emission regions seen in the F450W band data coincides with the OT position (see the top right image Fig.4.1).

In addition, we investigated the nature of the two objects in the vicinity of the host galaxy. The radial surface brightness profile of these objects is described by the point spread function in the HST images, as estimated from the stars in the field. Furthermore, there was no X-ray emission associated with these objects in the X-ray imaging of the afterglow. Hence we conclude that the objects marked as number 1 and 2 in Figure 4.1 (top left) are most probably foreground stars. We conducted the photometry of these objects including also the H and K data from Nov 24, 2001 (ID: 165H.-0464, PI: van den Heuvel) acquired by VLT/ISAAC, in order to estimate the spectral type assuming that they are stars. The colors of object 2 are $V - R = 1.16 \pm 0.10$ mag, $J - H = 0.62 \pm 0.05$ mag and $H - K = 0.14 \pm 0.03$ mag. These colors indicate that object 2 is a main-sequence star of spectral type of M2 (Tokunaga 2000). The colors of object 1 are much redder with $V - R = 2.85 \pm 0.10$ mag, $J - H = 0.17 \pm 0.10$ mag and $H - K = 0.61 \pm 0.12$ mag. These colors fit marginally with that of a late M-type or an early L-type star (Tokunaga 2000; Leggett et al. 2003). However, we do not exclude the possibility that object 1 may be an unresolved high-redshift galaxy.

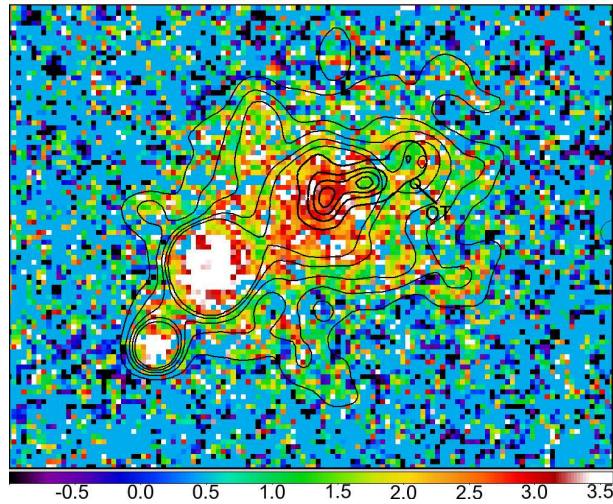


Figure 4.3: F450W – F702W color image of the field of GRB 011121. The position of the OT is indicated with an arrow. The thin-line contour is the the contour of the galaxy in the F702W filter and the thick-line is the contour in the F450W filter, overplotted on the color image.

4.4 Photometry

Photometry was extracted using the IRAF/*Ellipse* task which performs aperture photometry inside elliptical isophotes. The 1σ surface brightness limit and the metric radius were calculated for each image in order to determine the size of an aperture which covers the galaxy and minimizes the contamination by the background noise. The metric radius is defined as the radius where the Petrosian index $\eta = 0.2$, the Petrosian index being the ratio of the average surface brightness within a radius r to the surface brightness at r (Petrosian 1976; Djorgovski & Spinrad 1981). Both values correspond to a semi-major axis length of 2.1 – 2.4 arcsec for all images except for the F450W filter image for which the surface brightness limit is reached at $\sim 1''$. In order to conduct a consistent analysis, we performed aperture photometry on each image with the same semi-major axis length of 2.25 arcseconds. Table 4.2 shows the resulting magnitudes and errors. The errors in magnitudes were calculated assuming Poisson noise and include the readout noise and zero-point errors. The background fluctuation values were obtained by calculating the standard deviation from the mean background values measured for several different areas near the galaxy. Then a correction due to dithering was applied to the background noise of the HST images, assuming that the dither pattern is uniform (see Fruchter & Hook 2002).

Magnitudes were computed using i) the best-fit ellipticity and position angle for each filter obtained by *Galfit*, and ii) fixing the ellipticity and position angle to 0.13 and $27^\circ.5$, respectively for all filters. The results were the same for both cases. *Ellipse* also provides

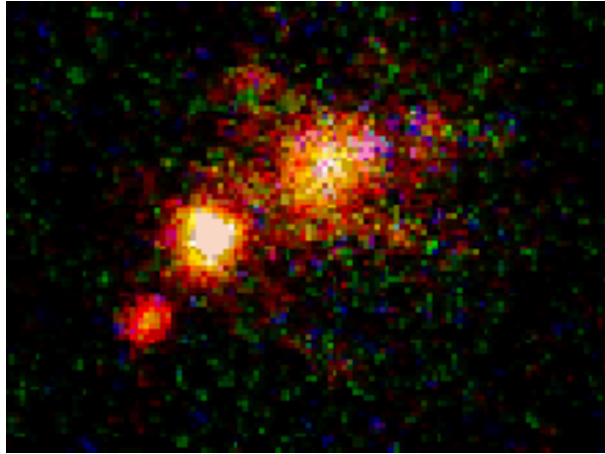


Figure 4.4: A white image of the field of GRB 011121 constructed using the images in the F450W (*blue*), F555W (*green*), F702W and F814W (*red*) filters.

the magnitudes inside a circular area having the same radius of the semi-major axis of the elliptical isophote. We compared the magnitudes determined within the circular and elliptical areas and found that the difference is <0.02 mag. This indicates the reliability of the $2''.25$ extent, the position angle and the ellipticity of the galaxy.

The value of M_B^* (uncorrected for dust attenuation) for redshifts between 0 and 0.5 is given by Dahlen et al. (2005) as $-21.06^{+0.10}_{-0.06}$ for $h = 0.65$. It is derived by fitting a Schechter luminosity function and using all types of galaxies, i.e. early type, late type and starbursts. From this value, we determine a luminosity ratio of $L_B/L_B^* = 0.26$ for the host galaxy of GRB 011121, which indicates that this galaxy is subluminal.

4.5 Analysis of the Spectral Energy Distribution

In the following sections we discuss the spectral energy distribution (SED) of the host galaxy of GRB 011121. We use the SED to deduce galaxy properties like characteristic age and metallicity of the stellar populations and the SFR. We employ the publicly available HyperZ code (Bolzonella et al. 2000) in addition to our own modelling in order to explore the galaxy properties.

4.5.1 Analysis using HyperZ

Following the seminal work on GRB host galaxies by Christensen et al. (2004a; 2004b), we avail of *HyperZ* (Bolzonella et al. 2000). This code employs a large grid of models based on 8 different synthetic star-formation histories (Bruzual & Charlot 1993), roughly matching the observed properties of local field galaxies (starburst, elliptical, spiral, and irregular

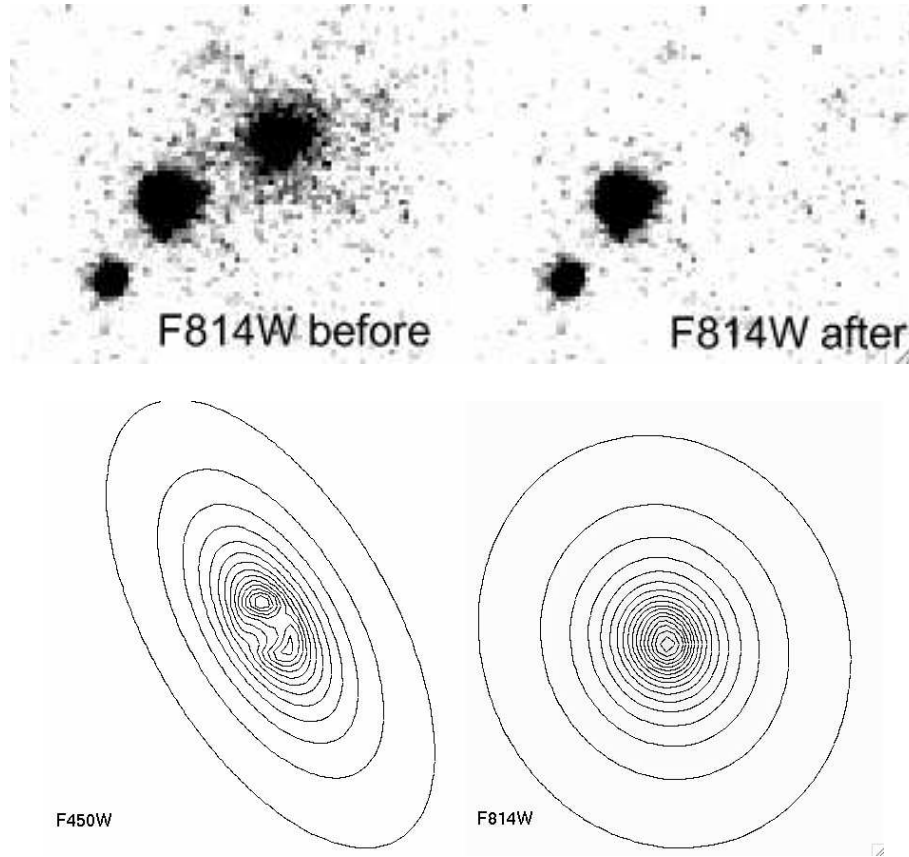


Figure 4.5: *Top Panel Left:* The image of the field in the F814W filter in April 2002. *Top Panel Right:* The residuals after subtracting the best-fit *Galfit* galaxy model from the original image. *Bottom Panel:* The contours of the best-fit model of the *Galfit* analysis for the F450W data (on the left) and for the F814W data (on the right).

Table 4.2: Results of the Photometry

Filter	Brightness ¹ mag	Foreground extinction mag	Absolute magnitude ^{2,3} mag
F450W	23.44±0.04	1.43	-19.5
F555W	22.64±0.02	1.14	-20.3
F702W	21.63±0.01	0.86	-20.6
F814W	21.18±0.02	0.67	-21.1
J _s	19.87±0.06	0.32	-22.1

¹ Magnitudes are not corrected for Galactic extinction.

² The absolute magnitudes are corrected for Galactic extinction.

³ The absolute magnitudes are given for the filters B, V, R, I, J in respective order.

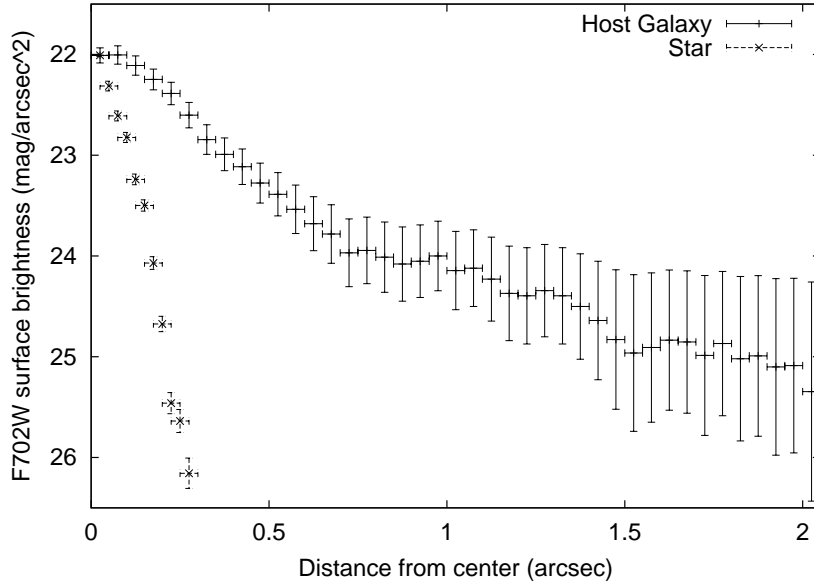


Figure 4.6: The surface brightness profile of the host galaxy and a star in the F702W filter. The surface brightness values of the star are normalized to those of the galaxy for presentation purposes.

ones). For all models, metallicity is fixed to the solar value ($Z = 0.02$). The empirical formula of Calzetti et al. (2000) for nearby starbursts is used to describe attenuation by dust in galaxies, independent of the star-formation history and morphology. Finally, a Miller & Scalo (1979) initial mass function with an upper mass limit for star formation of $125 M_{\odot}$ is used.

We find that old ages (i.e. $\geq 1 - 2$ Gyr) are not favoured (best-fit values of 45 Myr for starbursts and up to 720 Myr for spirals and irregulars) from the fitting of the broad-band photometry of the host galaxy of GRB 011121 with *HyperZ* models. Furthermore the amount of internal extinction is non-negligible ($A_V = 0.80 - 1.0$ mag, rest frame) for all models producing equally valid fits with $\chi^2_{\nu} < 0.26$. An A_V of $0.80 - 1.0$ mag corresponds to $E(B - V) = 0.20 - 0.25$ mag for a so-called Calzetti law. We note that this value of reddening by internal dust refers to the whole galaxy and, thus, is not directly comparable in a quantitative way to the values estimated from spectroscopy of the OT region, once the contribution of Galactic reddening is removed.

These results hold independent of the synthetic star-formation history of the model, which mirrors the fact that the 4000 -break is not very prominent in stellar populations younger than ~ 1 Gyr and, thus, does not offer a robust constraint to discriminate different evolutionary patterns. Finally, we note that an even broader range of possible values for age and extinction exists if we consider fits with $\chi^2_{\nu} < 1$. This increase in degeneracy of the solutions is not a shortcoming of *HyperZ* because it was designed to find photometric

redshifts and provides only a rough estimate of the SED type (see Bolzonella et al. 2000), independent of morphology.

4.5.2 Broad-band SED fitting

In order to exploit the information on morphology available for the host galaxy of GRB 011121 and better link the mode of star-formation and the properties of dust attenuation, we build our own set of physically motivated models. We combine various composite stellar population models and models of radiative transfer of the stellar and scattered radiation through different dusty media. We use a tailored grid of parameters in order to probe the very wide parameter space available for models in an efficient way. A large suite of synthetic SEDs is built as a function of total (gas+stars) mass, age (i.e. the time elapsed since the onset of star formation) and a characteristic opacity of the model, as described in the following subsections. These three free model parameters are determined from the comparison of synthetic broad-band apparent magnitudes (observed frame) and the apparent magnitudes determined for the host galaxy of GRB 011121 (see Sect. 4) through the standard least-square fitting technique.

Stellar population models

We model the intrinsic (i.e. not attenuated by internal dust) SED of the host galaxy of GRB 011121 as a composite stellar population. We make use of the stellar population evolutionary synthesis code PÉGASE (Fioc & Rocca-Volmerange 1997) (version 2.0) in order to compute both the stellar continuum emission and the nebular emission. Gas is assumed to be transformed into stars of increasing metallicity as the time elapsed since the onset of star formation increases and the initial metallicity of the ISM being equal to zero. The stellar initial mass function (IMF) used is that of Salpeter (1955), with lower and upper masses equal to 0.1 and 120 M_{\odot} , respectively. Adopting a different IMF mainly affects the determination of the stellar mass; for instance, a Chabrier (2003) IMF produces stellar masses lower by about 30 per cent than a Salpeter (1955) one.

The mass-normalized SFR of the models is assumed either to be constant (*starburst* models) or to decline exponentially as a function of time (*normal star-forming galaxy* models). For models of a normal star-forming galaxy, we adopt e-folding times equal to 1 and 5 Gyr to describe the star-formation histories of the bulge and disk components, respectively. The value of bulge-to-total mass ratio is set to 0.05, 0.1, 0.15 or 0.2. For starburst models, a range of 18 ages between 0.1 and 9 Gyr is considered³ using a fine time step of 0.1 Gyr up to an age of 1 Gyr and coarse step of 1 Gyr thereafter. For normal star-forming galaxy models, a range of 28 ages between 0.5 and 7 Gyr is considered. For these models, a fine time step is adopted for ages between 1 and 3 Gyr in order to follow the different evolution of the stellar populations of the bulge and disk components in more detail. Finally, we

³Models older than 9 Gyr do not offer a physical representation of a galaxy at $z = 0.362$ as the host of GRB 011121.

assume that the total mass of the system ranges from 10^9 to $2 \times 10^{11} M_{\odot}$ with 200 steps in mass being considered.

Dust attenuation models

As a statistical description of dust attenuation in starbursts, we make use of the Monte Carlo calculations of radiative transfer of the stellar and scattered radiation by Witt & Gordon (2000) for the SHELL geometry. In this case, stars are surrounded by a shell where a two-phase clumpy medium hosts dust grains with an extinction curve like that of the Small Magellanic Cloud (SMC), as given by Gordon et al. (1997). We note that these models describe dust attenuation in nearby starburst galaxies (Gordon et al. 1997) as well as in Lyman Break Galaxies at $2 < z < 4$ (Vijh et al. 2003). We consider 14 values of the opacity τ_V (0.25 – 9), where τ_V is the radial extinction optical depth from the center to the edge of the dust environment in the V-band, assuming a constant density, homogeneous distribution. We note that τ_V gives the total amount of dust in the shell, once the radius of the shell is fixed.

In the case of the normal star-forming galaxy models, we assume that dust attenuation is described by the Monte Carlo calculations of radiative transfer of the stellar and scattered radiation for an axially symmetric disk geometry illustrated in Pierini et al. (2004b) and based on the DIRTY code (Gordon et al. 2001). These models have been applied successfully to interpret multiwavelength photometry of edge-on late-type galaxies in the local Universe (Kuchinski et al. 1998). The physical properties of the dust grains are assumed to be the same as those in the diffuse ISM of the Milky Way (from Witt & Gordon 2000). Furthermore, we use the central opacity $\tau_V^{c,0}$ parameter which refers to the face-on extinction optical-depth through the centre of the dusty disk in the V-band. For the disk models, the central opacity is set to 0.5, 1, 2, 4, 8, and 16.

An inclination of about 18 degrees is determined from the observed ellipticity of the host galaxy of GRB 011121 (see Tab. 4.1), for an intrinsic axial ratio of 0.2. Hence we adopt disk galaxy models with only this inclination because the effect on the total luminosity is small for inclinations much less than 70 degrees in a disk-dominated system (e.g. Pierini et al. 2003) such as the host galaxy of GRB 011121. In fact, the Sersic index fitted to different light profiles of the host galaxy of GRB 011121 (see Tab. 4.1) is consistent with the presence of a small bulge like in Sbc galaxies. Greiner et al. (2003) estimated the bulge-to-disk (B/D) J_s -band luminosity ratio to be about 0.28 using a de Vaucouleurs+exponential model to reproduce the J_s -band surface brightness profile of the host galaxy of GRB 011121. Hence, we use a bulge-to-disk J_s -band luminosity ratio between 0.23 and 0.33 as a further constraint for our bulge+disk models allowing for mismatches between the fitting model of Greiner et al. (2003) and the structure of the system described in Pierini et al. (2004b).

Finally, for all models we assume that the gas emission at a given wavelength is attenuated by the same amount as the stellar emission at that wavelength, independent of whether the gas emission is in a line or in the continuum (see Pierini et al. 2004a for a discussion).

Table 4.3: Results for the starburst and normal star forming Sbc-like galaxy models

Galaxy model	$\tau_V/\tau_V^{c,0}$	age Gyr	Z 10^{-3}	M_\star $10^9 M_\odot$	χ_ν^2
Starburst	1.5 – 0.5	0.4 – 2	0.3 – 1.6	3.1 – 4.8	< 6.91
Sbc-like	16 – 2	1.3 – 1.9	3.9 – 5.8	4.9 – 6.9	< 6.91

Results

Synthetic SEDs and magnitudes are computed and evaluated against the observed broadband SED of the host galaxy of GRB 011121 for a suite of 50,400 starburst models plus 124,800 normal star-forming models (see Sect. 4). Reassuringly, each suite of models brackets the best-fit solution although the parameter space is not spanned in a uniform way. Hereafter we describe the basic aspects of those fit solutions that are called “plausible”, being characterized by $\chi_\nu^2 < 6.91$, that corresponds to a probability of 0.001 for two degrees of freedom (given by 5 photometric points minus 3 model parameters). Results for the starburst and the normal star forming Sbc-like galaxy models are presented in Table 4.3.

Plausible solutions for the starburst case imply ages between 0.4 and 2 Gyr and, accordingly, an opacity decreasing from 1.5 to 0.5 as illustrated in Figure 4.7. This domain is narrower than the explored parameter space, nevertheless it still reflects the well-known age–opacity degeneracy for starbursts (Takagi et al. 1999). The values of the bolometric luminosity-weighted metallicity in stars increases from 3×10^{-4} to 1.6×10^{-3} , while the total mass of the system drops from 18.5 to $6.3 \times 10^{10} M_\odot$. The latter range corresponds to a range of $3.1 - 4.8 \times 10^9 M_\odot$ in stellar mass. In particular, the best-fit model for the starburst case has an age of 0.5 Gyr, a bolometric luminosity-weighted metallicity in stars equal to 3.7×10^{-4} , a stellar mass of $3.6 \times 10^9 M_\odot$ and an opacity equal to 1.5^4 . We note that $\tau_V = 1.5$ corresponds to an attenuation of the total flux at V-band (rest frame) $A_V = 0.76$ mag and a reddening $E(B - V) = 0.20$ mag on the scale of the system.

Alternatively, plausible solutions for the normal star-forming case have a bulge-to-total mass ratio equal to 0.15. They imply ages between 1.3 and 1.9 Gyr and, accordingly, a central opacity of the disk decreasing from 16 to 2 (see Fig. 4.8). At the same time, the bolometric luminosity-weighted metallicity in stars of the disk increases from 3.9×10^{-3} to 5.8×10^{-3} . The total mass of the system drops from 2.5 to $1.7 \times 10^{10} M_\odot$ from the youngest and most opaque systems to the oldest and least opaque ones. The range in stellar mass spanned by these plausible solutions is $4.9 - 6.9 \times 10^9 M_\odot$. In particular, the best-fit model for the normal star-forming case has an age of 1.3 Gyr, a bolometric luminosity-weighted metallicity in stars of the disk equal to 3.9×10^{-3} , a stellar mass of $5.7 \times 10^9 M_\odot$ and a central opacity of the disk equal to 16. We note that $\tau_V^{c,0} = 16$ corresponds to an attenuation (along the line of sight) of the total rest-frame V-band

⁴The two-phase, clumpy SHELL model of Witt & Gordon (2000) with SMC-type dust and $\tau_V = 1.5$ produces an attenuation curve that best matches the so-called Calzetti law for nearby starbursts (see Calzetti et al. 2000 and references therein).

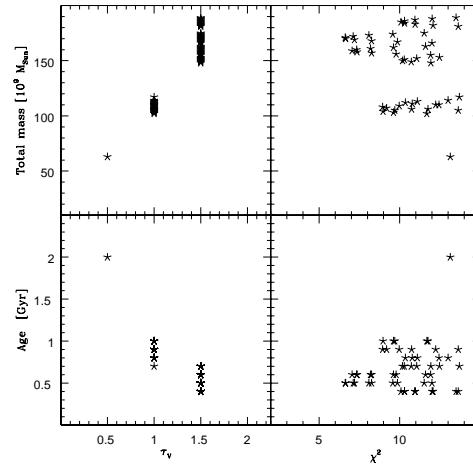


Figure 4.7: SED fit solutions with $\chi_\nu^2 < 6.91$, using starburst models. *Left:* Total (gas+stars) mass (*top*) and age (*bottom*) versus τ_V , *Right:* Total mass (*top*) and age (*bottom*) versus χ_ν^2 . The plausible values for the opacity τ_V varies between 0.5 and 1.5 where the age ranges from 0.4 to 2 Gyr and the total mass ranges from 6.3 to $18.5 \times 10^{10} M_\odot$ (see text for a more detailed discussion).

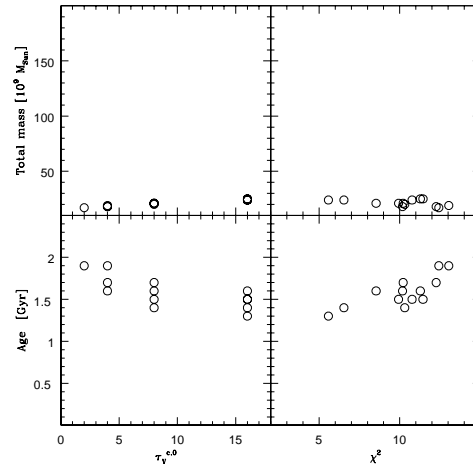


Figure 4.8: SED fit solutions with $\chi_\nu^2 < 6.91$ for normal star-forming galaxy models. *Left:* Total (gas+stars) mass (*top*) and age (*bottom*) versus $\tau_V^{c,0}$, *Right:* Total mass (*top*) and age (*bottom*) versus χ_ν^2 . The plausible central opacity values varies between 2 – 16 where the age of the galaxy ranges from 1.3 to 1.9 Gyr and the total mass ranges from 1.7 to $2.5 \times 10^{10} M_\odot$ (see text for a more detailed discussion).

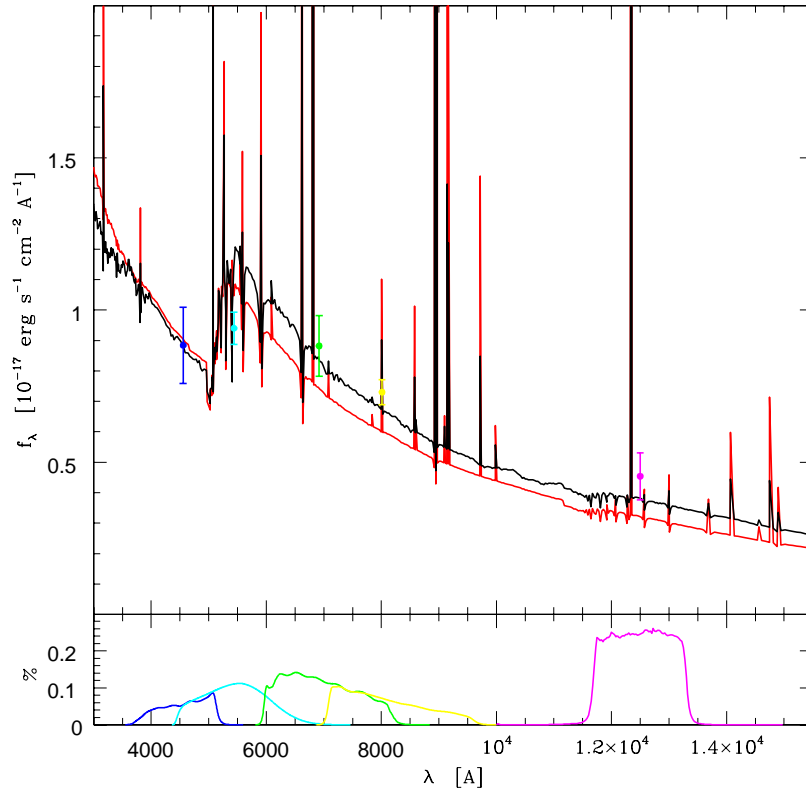


Figure 4.9: The best-fit normal star-forming galaxy model (in black), and the best-fit starburst model (in red). The points are the fluxes of the host galaxy derived from the observed magnitudes corrected for the foreground extinction. The filter curves are shown in the lower panel, for the corresponding filters.

flux $A_V = 0.57$ mag for an inclination of 18 degrees. In terms of reddening of the stellar component of the only disk, the best-fit Sbc-like model implies $E(B - V) = 0.08$ mag on the disk scale. Even smaller values of reddening will apply to a peripheral region of the disk, where the OT of GRB 011121 was actually located. Hence plausible solutions for a normal star-forming bulge+disk system comfortably meet the constraints on a low amount of reddening in the OT region of GRB 011121.

The best-fit models for a starburst system and a normal star-forming bulge+disk system, and the observed photometry of the host galaxy of GRB 011121 are presented in Figure 4.9. The comparison with the data reveals that both best-fit models underpredict the observed J_s -band magnitude by about 0.1 mag, i.e. almost 2σ . This is the main reason for their rather high values of χ_ν^2 . A posteriori, we interpret this discrepancy as due to the fact

Table 4.4: Results of Starburst Model Fits with (*first row*) and without (*second row*) J_s-band data

τ_V	age Gyr	Z 10^{-3}	M_\star $10^9 M_\odot$	χ_ν^2
0.25 – 1.5	0.4 – 2.0	0.3 – 1.6	3.1 – 4.9	< 5.41
1	0.8 – 0.9	0.6 – 0.7	3.5 – 3.8	< 1.00

that PÉGASE (version 2.0) does not include the contribution to the total emission from the thermally pulsating asymptotic giant branch (TP-AGB) phase of stellar evolution (see Maraston 2005). TP-AGB stars are cool giants exhibiting very red optical/NIR colours (e.g. Persson et al. 1983). They are expected to play a significant role in the rest-frame visual-to-near-IR emission of galaxies containing 1-Gyr-old stellar populations (Maraston 1998; 2005). The best-fit models contain stellar populations that are up to 0.5 or 1.3 Gyr old (starburst or Sbc-like model, respectively), hence it is plausible that they can slightly underpredict the flux in the observed J_s-band magnitude⁵.

We tested that the previous results are not biased by the absence of the contribution to the total emission from the TP-AGB stars in PÉGASE (version 2.0). We performed new fits where the range in the J_s-band B/D allowed by the estimate of Greiner et. al. (2003) and/or the J_s-band flux were not used to constrain the solutions. In this case, plausible solutions were characterized by $\chi_\nu^2 < 5.41$, that corresponds to a probability of at least 0.001 for the only one degree of freedom for both starburst and Sbc-like models. The new plausible solutions for starburst models allowed a slightly larger parameter space but without major changes with the exception that a limited number of plausible solutions with a $\chi_\nu^2 < 1$ did exist now (see Table 4.4 and also Table 4.3 for comparison). Also for normal star-forming bulge+disk models the parameter space allowed by the new plausible solutions became slightly larger (see Table 4.5); in particular, the bulge-to-total mass ratio was unconstrained. These new solutions spanned the whole range in central opacity, the least opaque models ($\tau_V^{c,0} = 0.50$) having older ages (1.5 – 2.9 Gyr) than the most opaque ones (with $\tau_V^{c,0} = 16$ and an age of 1.0 – 1.7 Gyr). Models with larger bulge-to-total mass ratios tended to be younger, independent of the central opacity; however, the stellar mass was still a few to several times $10^9 M_\odot$ overall. This time plausible solutions with a $\chi_\nu^2 < 1$ did exist also for Sbc-like models, without major changes in terms of properties of the stellar populations and mass of the system (see Table 4.3 for comparison).

⁵We note that the models of Bruzual & Charlot (1993) included in *HyperZ* (Bolzonella et al. 2000) do not include the contribution to the total emission from the TP-AGB stars (see Maraston 2005) as well. However, they have stellar populations with only solar metallicity, which are redder than those with lower metallicity.

Table 4.5: Results of Sbc-like Model Fits with and without J_s-band data

B/T ¹	$\tau_V^{c,0}$	age Gyr	Z 10 ⁻³	M _★ 10 ⁹ M _☉	χ_ν^2
0.05	0.50 – 16	1.0 – 2.9	3.0 – 8.5	3.6 – 6.4	< 5.41
0.05	4, 16	1.3 – 1.5	3.9 – 4.6	4.8 – 5.0	< 1.00
0.10	0.50 – 16	1.0 – 2.6	3.0 – 7.7	3.3 – 6.4	< 5.41
0.10	0.50 – 8	1.5 – 2.1	4.6 – 6.3	4.4 – 5.1	< 1.00
0.15	0.50 – 16	1.0 – 2.5	3.0 – 7.5	3.9 – 6.9	< 5.41
0.15	0.50, 4, 8	1.3 – 1.8	3.9 – 5.5	4.4 – 4.9	< 1.00
0.20	0.50 – 16	1.0 – 2.3	3.0 – 6.9	3.6 – 6.8	< 5.41
0.20	0.50, 1, 4, 16	1.2 – 1.9	3.6 – 5.8	4.6 – 5.6	< 1.00

¹ Bulge-to-total mass ratio.

4.6 Star Formation Rate

The previous plausible solutions give values of the SFR equal to $3.1 - 9.4 M_\odot \text{ yr}^{-1}$ (starburst models) or $2.4 - 4.1 M_\odot \text{ yr}^{-1}$ (normal star-forming, Sbc-like models) while the value of SFR decreases as the time elapses since the start of star formation⁶. For the same models, the SFR per unit stellar mass is equal to $0.6 - 2.9 \times 10^{-9} \text{ yr}^{-1}$ or $0.4 - 0.7 \times 10^{-9} \text{ yr}^{-1}$, respectively. Consistently, for this subluminal galaxy ($L_B/L_B^* = 0.26$), the SFR per unit luminosity is equal to $11.9 - 36.1 M_\odot \text{ yr}^{-1} (L_B/L_B^*)^{-1}$ or $9.2 - 15.8 M_\odot \text{ yr}^{-1} (L_B/L_B^*)^{-1}$.

These values of the SFR per unit stellar mass are high compared to those of simulated galaxies in Courty et al. (2004), in agreement with their conclusion that the GRB-host galaxies are identified as the most efficiently star-forming objects. Other GRB-host galaxies have similarly high values of the SFR per unit luminosity (cf. Christensen et al. 2004a), though not as high as our estimates. Recent calculations by Gorosabel et al. (2005) and Sollerman et al. (2005) give similar values of the extinction-corrected SFR per unit luminosity for the host galaxies of the two low-redshift GRB 030329 and GRB 031203.

Finally, we compared the values obtained for the SFR per unit galaxy stellar mass of the host galaxy of GRB 011121 with those of observed galaxies selected from the MUNICS and FORS deep field surveys (Bauer et al. 2005) in the same redshift range $0.25 < z < 0.4$ as the previous GRBs and GRB 011121 itself. The values of the specific SFR (SSFR) given by Bauer et al. (2005) were determined from the [OII] line flux without any correction for dust extinction. This comparison confirms that the host galaxy of GRB 011121 is among the galaxies with highest specific SFR at these redshifts even after allowing for an extreme correction factor of 10 for the SSFRs given by Bauer et al. (2005).

⁶For a *different region of the host galaxy GRB 011121 containing the OT*, Greiner et al. (2003) estimated values of the SFR from [OII] and H α emission-line diagnostics *at times when the afterglow was present*. These values are: $1.2 M_\odot \text{ yr}^{-1}$ (SFR_[OII]) and $0.61 - 0.72 M_\odot \text{ yr}^{-1}$ (SFR_{H α}). It is clear that these values do not refer to the whole galaxy and are not corrected for the intrinsic extinction.

4.7 Summary

The existence of high-resolution imaging in 5 broad-band, optical and near-infrared filters with HST and VLT/ISAAC for the host galaxy of GRB 011121 (at $z = 0.36$) allows a detailed study of both the morphology and the spectral energy distribution of this galaxy. Multi-band, high signal-to-noise ratio, high-resolution imaging of GRB host galaxies is still a luxury, only affordable for the brightest and most nearby galaxies.

Firstly, we find that the surface brightness profile of the host galaxy of GRB 011121 is best fitted by a Sersic law with index $n \sim 2 - 2.5$ and a rather large effective radius (~ 7.5 kpc). In combination with the F450W - F702W colour image, this suggests that this galaxy is either a disk-system with a rather small bulge (like an Sbc galaxy), or one hosting a central, dust-enshrouded starburst.

Alternative to the previous studies on GRB host galaxies, we combine stellar population models and Monte Carlo calculations of radiative transfer to reproduce the observed SED. Furthermore, we make use of the morphological information to constrain these models. Plausible solutions meeting all the morphological and/or photometric constraints indicate that the host galaxy of GRB 011121 has a stellar mass of a few to several times $10^9 M_{\odot}$, stellar populations with a maximum age ranging from 0.4 to 2 Gyr, and a bolometric luminosity-weighted metallicity in stars (of the disk, in case) ranging from 1 to 29 per cent of the solar value.

In particular, normal star-forming, Sbc-like models provide plausible solutions pointing to a system as massive as $4.9 - 6.9 \times 10^9 M_{\odot}$, with a bulge-to-total mass ratio equal to 0.15, an age of 1.3 - 1.9 Gyr, and a bolometric luminosity-weighted metallicity in stars of the disk equal to 20 - 29 per cent solar. Alternatively, starburst models provide plausible solutions biased towards a lower stellar mass ($3.1 - 4.8 \times 10^9 M_{\odot}$), a younger age (0.4 - 2.0 Gyr) and a much lower metallicity (1 - 8 per cent solar). As for the opacity, normal star-forming, Sbc-like models indicate the host galaxy of GRB 011121 as a system with a central opacity $\tau_V^{c,0}$ in the range 2 - 16, i.e. larger than the central opacity of local disks (0.5 - 2, see Kuchinski et al. 1998). Nevertheless, the attenuation along the line of sight is moderate ($A_V = 0.12 - 0.57$ mag) on the scale of the system, since the host galaxy of GRB 011121 has a low inclination (18 degrees). On the other hand, starburst models suggest this galaxy to be nearly as opaque ($\tau_V = 0.5 - 1.5$) as local starburst galaxies (with $\tau_V \sim 1.5$, see Gordon et al. 1997), the attenuation along the line of sight being $A_V = 0.27 - 0.76$ mag on the scale of the system.

The SFR per unit stellar mass is equal to $0.6 - 2.9 \times 10^{-9} \text{ yr}^{-1}$ (starburst) or $0.4 - 0.7 \times 10^{-9} \text{ yr}^{-1}$ (normal star-forming galaxy), while the SFR per unit luminosity is equal to $11.9 - 36.1 M_{\odot} \text{ yr}^{-1} (L_B/L_B^*)^{-1}$ or $9.2 - 15.8 M_{\odot} \text{ yr}^{-1} (L_B/L_B^*)^{-1}$, respectively.

This large (effective radius of ~ 7.5 kpc) but subluminal ($L_B/L_B^* = 0.26$) galaxy exhibits a specific SFR that is larger than that of the average galaxy at the same redshift (e.g. Bauer et al. 2005) but consistent with the values determined for two other blue, low-metallicity, low- z GRB host galaxies (i.e. GRB 030329 and GRB 031203, see Gorosabel

et al. 2005, Sollerman et al. 2005). Therefore, we conclude that the host galaxies of GRB011121 and, possibly, GRB030329 and GRB031203 are caught at relatively early phases of their star formation histories.

5 Conclusions

Gamma-ray bursts are known as the most distant explosions in the Universe and can be observed up to very high redshifts¹ due to their unique features such as the very energetic prompt γ -ray emission and the following afterglow emission from X-rays to radio. Therefore, GRBs and their host galaxies can be used to probe the early Universe and help solving the mysteries regarding the first galaxies, cosmic re-ionization era or the star formation history of the Universe. The mechanisms underlying their observational features and thus the nature of the GRBs must be understood in order to use them as cosmological probes.

GRBs are known for over 30 years, nonetheless the major breakthrough in GRB science was achieved with the discovery of the afterglows and host galaxies in 1997. Since then observations of afterglow emission and host galaxies have become major branches of GRB research in combination with the observations of the prompt emission. The work presented in this thesis is related to different aspects of GRBs and their host galaxies studied based on afterglow and host galaxy observations using various methods; i.e. morphological, photometric and spectral analysis.

Afterglow observations are proved to be one of the most powerful tools to understand the nature of GRBs and to measure their redshift. To strengthen the power of this tool and to reduce the statistical biases introduced by observational limitations, the specifically developed instrument GROND presents a genuine opportunity. The GROND Pipeline system is a complementary part of the instrument that brings along two important and necessary advancements. The first one is that the GP analyses the data in a special way that is required in order to construct the spectral energy distribution of the observed objects out of the 7-band data of GROND, and thus necessary to derive the redshift of the GRBs. The second advancement introduced by the GP is that it automates both the observations and the data analysis in order to take the full advantage of the rapid afterglow observations and feedback the analysis results to the process of observation. The afterglow flux decreases with time, making it difficult to observe the sources later in time. Therefore rapidity is of vital importance in order to use the results of the analysis to conduct further deep observations, i.e. to conduct spectroscopy, to detect the host galaxy etc., via world's largest optical and near-infrared telescopes.

The pipeline system of GROND utilizes the instrument and its telescope as a robotic system where the initial observation approval and guide star selection are the sole points requiring human-intervention. The application of automated photometric analysis and red-

¹Current highest redshift is $z = 6.3$ which is measured spectroscopically for GRB 050904.

shift determination combined with automated observations will be applied for the first time in the field rapid transient observations. Both the system/observation related part, i.e. scheduling of observations, user interaction etc., and the data analysis part, i.e. photometric analysis, identification of the GRB afterglow etc., conduct intelligent analysis normally done by astronomers. There are no pipeline systems in the world that conduct all of these jobs automatically. Therefore, GROND is a leading system not only with its instrumental capabilities, but also with its pipeline system. The outlook for GROND is that it will be one of the first systems that will be able to observe and determine the redshift of the very high redshift GRBs ($z \sim 3 - 13$) and allow further deep observations potentially leading further science results. Moreover, the GROND system will conduct the follow-up observations and analysis of many GRBs systematically.

Similar to the afterglows of the GRBs, their host galaxies play a key role in understanding the nature of the GRB progenitors. One of the indicators about the nature of the GRB progenitor is the density of the circumburst environment, which can be studied via the emission lines of the GRB host galaxies. The spectral time-series analysis of the host galaxy of GRB 990712 is the first case that emission from cooling GRB remnants is probed on a time scale of years. It is part of a larger program (075.D-0771(A), PI: A. Küpcü Yoldaş) that involves 3 other GRB hosts that were re-observed spectroscopically with FORS2 on ESO/VLT telescope. These other hosts are the host galaxies of GRB 011121, 020405 and 031203 whose observations span to approximately 3.5, 3 and 1.5 years after the burst, respectively. The analysis of the data set of the host of GRB 990712 is the first example, and combining it with the analysis of the other three GRB host galaxy observations will be the first step of forming a statistical sample and also a feasibility study.

The host galaxy of GRB 990712 has the longest time coverage up to date with its five spectroscopic observations dispersed over 6 years after the burst. This distinguished data set allowed us to constrain the density of the inner 2 parsec of the circumburst environment of GRB 990712. We derive a limit of $n \lesssim 6 \times 10^3 \text{ cm}^{-3}$ using the uncertainty in the [O III] $\lambda 5007$ luminosity, which alone disfavours high shell densities within 2 parsec. However, there are models allowing high density shells that exist beyond the inner 2 parsec, therefore long term (on the order of decades) monitoring of the GRB host galaxies is necessary to constrain a larger volume. Constant monitoring would also allow modelling of the circumburst environment in more detail. Moreover, observations with better sensitivity are required to constrain the density more accurately. Considering the difficulties in cross calibrating the data obtained at different times with different instruments, the best approach is to use the same instrument and settings to obtain high resolution, high signal-to-noise ratio data.

Furthermore, the possible contribution from the photoionized circumburst environment may also lead to incorrect values for SFR and metallicity of the host galaxy and of the circumburst region. These two important galaxy properties are usually calculated based on emission line fluxes which are obtained at a single epoch of observation. Therefore, multiple epochs of observations spanned over a long time scale will also serve to properly assess the possible level of contamination by the cooling GRB remnant.

The observations of GRB host galaxies are also important to derive the host galaxy properties. The galaxy properties contribute to two important domains: the nature of the GRB progenitor and the early Universe. The nature of the progenitor can be constrained via existence of a possible relation between GRBs and their host galaxies. The current sample of long duration GRB host galaxies have ~ 80 members spanning a redshift range of $0.0085 - 6.3$, however there is no consensus whether the GRB hosts galaxies prefer a certain type. Statistical studies applied to ~ 40 hosts led to the conclusion that they are mostly compact disk galaxies with a significant fraction of merging and interacting systems. However, these studies are based mostly on the single band data covering the rest-frame blue or ultraviolet wavelength domain. Spectroscopic or SED analysis are only available for a smaller subsample ($\lesssim 20$) of these galaxies, mostly indicating that they are sub-luminous (and thus, dwarf) and blue galaxies.

On the other hand, GRB host galaxies are not selected by flux or limited by volume as the galaxies detected by surveys. Furthermore, with fast and accurate follow-up observations of the bright early afterglow emission, via dedicated instruments like GROND, we may be able to localize the host galaxy which would probably be missed otherwise by optical/IR high-redshift galaxy surveys. Consequently, GRB hosts can be used to study the galaxy formation models and the star-formation history of the Universe, if they are not biased, or any possible bias can be predicted and well defined. Therefore, it is important to understand the properties of the GRB hosts both in connection with the progenitor theories and in view of future observations of hosts at very high redshifts.

The data set of the host galaxy of GRB 011121 is one of the most extensive and deep imaging data set available for GRB hosts, providing the the unique possibility to study the host galaxy properties through the parameter space from morphology to stellar mass. The advantage of multi-color morphology revealed itself in the form of consistent analysis results, despite the difference of the galaxy morphology in the blue wavelengths compared to the redder wavelengths. Furthermore, we used the results of the morphological analysis to restrict the parameter space to model the SED, and to combine different stellar population models with radiative transfer models. This allowed us to constrain the galaxy properties more reliably and accurately. The results of the analysis suggest that this host galaxy is a rather large disk-system in a relatively early phase of its star formation history. This indicates that not all GRB host galaxies are dwarf galaxies. However, the stellar mass, colors and metallicity of the host of GRB 011121 are in agreement with those of a relatively well studied subsample of GRB host galaxies, and thus this host galaxy could have been classified as a dwarf galaxy without the constraints obtained from the morphological analysis. In other words, this analysis and its results shows that the properties derived from the SED alone may be insufficient to derive reliable conclusions on the type of the galaxy, and the morphological analysis plays a key role. Therefore it highlights the necessity for a morphological analysis combined with a detailed SED analysis to derive reliable conclusions based on statistical or individual analysis results of the host galaxies. Furthermore, applying this method to a larger sample of host galaxies with multi-color high spatial resolution imaging data would allow us to determine whether the host of GRB

011121 is an outlier compared to the rest of the sample or not.

All of the three topics studied in this thesis have different contributions to the GRB research, covering the hot topics of the GRB science such as the afterglow observations, the nature of the progenitor and host galaxy properties. Furthermore, all studies involve approaches applied for the first time to their particular field of study. The results on the environment of GRB 990712 and the host galaxy of GRB 011121 presented in this thesis show the importance of the kind of analysis applied on these fields, and point out the necessity of forming statistical samples of multi epoch high resolution spectroscopic or multi-band photometric observations analysed using these methods for a better understanding and reliability. On the other hand, GROND will start operating in early 2007. It is expected to yield remarkable scientific results with the essential help of its pipeline system. It will also increase the statistical sample of multi-band rapid observations of GRB afterglows and also spectroscopic observations of host galaxies via triggering further deep observations, which will lead to the necessary sample of observations required for future advances suggested by this thesis.

Bibliography

- Allen, C. W. & Cox, A. N. 2000, *Allen's Astrophysical Quantities* (4th ed. New York: AIP)
- Allen, J. F. 1983, *Comm. ACM* 26(11), 832
- Asplund, M., Grevesse, N., Sauval, A. J. 2005, *ASPC* 336, 25
- Band, D. L. & Hartmann, D. H. 1992, *ApJ* 386, 299
- Bauer, A. E., Drory, N., Hill, G. J., & Feulner, G. 2005, *ApJ* 621, L89
- Barthelmy, S. D., Cline, T. L., Butterworth, P. et al. 2000, *AIPC* 526, 731
- Bell, E. F., Papovich, C., Wolf, C. et al. 2005, *ApJ* 625, 23
- Berger, E., Chary, R., Cowie, L. L. et al. 2006, [astro-ph/0603689](#)
- Björnsson, G., Hjorth J., Jakobsson P. et al. 2001, *ApJ* 552, L121
- Bloom, J. S., Kulkarni, S. R., Djorgovski, S. G. 2002a, *AJ* 123, 1111
- Bloom, J. S., Kulkarni, S. R., Price, P. A. et al. 2002b, *ApJ* 572, L45
- Bolzonella, M., Miralles, J.-M., Pelló, R. 2000, *A&A* 363, 476
- Bouwens, R. J. et al. 2004, *ApJ* 606, L25
- Böttcher, M., Dermer, C. D., Crider, A. W., & Liang, E. P. 1999, *A&A* 343, 111
- Bromm, V. & Loeb, A. 2006, *ApJ* 642, 382
- Bruzual, G., & Charlot, S. 1993, *ApJ* 405, 538
- Bunker, A., Stanway, E. R., Ellis, R. S., & McMahon, R. G. 2004, *MNRAS* 355, 374
- Calzetti, D., Armus, L., Bohlin, R. C. et al. 2000, *ApJ* 533, 682
- Cambrésy, L., Jarrett, T. H., Beichman, C. A. 2005, *A&A* 435, 131
- Cardelli, J. A., Clayton, G. C., & Mathis, J. S. 1989, *ApJ* 345, 245
- Chabrier, G. 2003, *PASP*, 115, 763
- Chary, R., Becklin, E. E., & Armus, L. 2002, *ApJ* 566, 229

- Chevalier, R., Li, Z-Y., Fransson, C. 2004, ApJ 606, 369
- Christensen, L., Hjorth, J., Gorosabel, J. et al. 2004a, A&A 413, 121
- Christensen, L., Hjorth, J., & Gorosabel, J. 2004b, A&A 425, 913
- Conselice, C. J., Vreeswijk, P. M., Fruchter, A. S. et al. 2005, ApJ 633, 29
- Costa, E., Frontera, F., Heise, J. et al. 1997, Nature 387, 783
- Courty, S., Björnsson, G., Gudmundsson, E. H. 2004, MNRAS 354, 581
- Cox, D. P., Mathews, W. G. 1969, ApJ 155, 859
- Dahlen, T., Mobasher, B., Somerville, R. S. et al. 2005, ApJ 631, 126
- DePoy, D. L., Atwood, B., Belville, S. R. et al. 2003, Proc. SPIE 4841, 827
- Devillard, N., 2005, Eclipse Users Guide, at URL
<http://www.eso.org/projects/aot/eclipse/eug/index.html>
- Djorgovski, S. & Spinrad, H. 1981, ApJ 251, 417
- Dopita, M. A., Sutherland, R. S. 1996, ApJS 102, 161
- Drakengren, T., Jonsson, P. 1997, JAIR 7, 25
- Dutra, C. M., Ahumada, A. V., Clariá, J. J., Bica, E., Barbuy, B. 2003, A&A 408, 287
- Eldridge, J. J., Genet, F., Daigne, F., & Mochkovitch, R. 2006, MNRAS 367, 186
- Fan, X., Hennawi, J. F., Richards G.T. et al 2004, AJ 128, 515
- Fenimore, E., Epstein, R., Ho, C., Klebesadel, R.W., Lacey, C. et al 1993, Nature 366, 40
- Fioc, M., & Rocca-Volmerange, B. 1997, A&A, 326, 950
- Fishman, G. & Meegan, C. 1995, ARAA 33, 415
- Fox, D. B., Frail, D. A., Price, P. A. et al. 2005, Nature 437, 845
- Fransson, C., Cassatella, A., Gilmozzi, R. et al. 1989, ApJ 336, 429
- Frontera, F., Amati, L., Lazzati, D. et al. 2004, ApJ 614, 301
- Frontera, F., Amati L., Vietri M. et al. 2001, ApJ 550, L47
- Fruchter, A. S. & Hook, R. N. 2002, PASP 114, 144
- Fruchter, A. S., Levan, A. J., Strogler, L. et al. 2006, Nature 441, 463
- Fryer, C. L., Woosley, S. E., Herant, M., Davies, M. B. 1999, ApJ 520, 650

- Fryer, C. L., Rockefeller, G., Young, P. A. 2006, astro-ph/0604432
- Fynbo, J. U., Holland, S., Andersen, M. I. et al. 2000, ApJ 542, 89
- Gabasch, A., Salvato, M., Saglia, R. P. et al. 2004, ApJ 616, L83
- Galama, T. J., Vreeswijk, P. M., van Paradijs, J. et al. 1998, Nature 395, 670
- Garnavich, P. M., Stanek, K. Z., Wyrzykowski, L. et al. 2003, ApJ 582, 924
- Gehrels, N., Sarazin, C. L., O'Brien, P. T. et al. 2005, Nature 437, 851
- Giavalisco, M. et al. 2004, ApJ 600, L103
- Ghisellini, G., Haardt, F., Campana, S. et al. 1999, ApJ 517, 168
- Gordon, K.D., Calzetti, D., Witt, A. N. 1997, ApJ 487, 625
- Gordon K. D., Misselt K. A., Witt A. N., Clayton G. C. 2001, ApJ 551, 277
- Gorosabel, J., Klose, S., Christensen, L. et al. 2003a, A&A 409, 123
- Gorosabel, J., Christensen, L., Hjorth, J. et al. 2003b, A&A 400, 127
- Gorosabel, J., Pérez-Ramírez, D., Sollerman, J. et al. 2005, A&A 444, 711
- Greiner, J., Klose, S., Zeh, A. et al. 2001, GCN Circ. 1166
- Greiner, J., Klose, S., Salvato, M. et al. 2003, ApJ 599, 1223
- Harrison, F. A., Bloom, J. S., Frail, D. A. et al. 1999, ApJ 523, L121
- Heise, J., in't Zand, J., Tarei, G. et al. 1999, IAU Circ. 7221
- Heise, J., in 't Zand, J., Kippen, R. M., & Woods, P. M. 2001, in Gamma-ray Bursts in the Afterglow Era, ed. E. Costa, F. Frontera, & J. Hjorth (Berlin: Springer), 16
- Hjorth, J., Sollerman, J., Miller, P. et al. 2003, Nature 423, 847
- Hjorth, J., Holland S., Courbin, F. et al. 2000, ApJ 534, L147
- Hopkins, A. M., Connolly, A. J., Haarsma, D. B., & Cram, L. E. 2001, AJ 122, 288
- Janka, H.-T., Eberl, T. Ruffert, M., Fryer, C. L. 1999, ApJ 527, 39
- Kawai, N., Kosugi, G., Aoki, K. et al. 2006, Nature 440, 184
- Kennicutt, R. C. 1998, ApJ 498, 541
- Kewley, L. J. & Dopita, M. A. 2002, ApJS 142, 35
- Kippen, R. M. et al. 2003, in AIP Conf. Proc. 662, Gamma-Ray Bursts and Afterglow Astronomy, ed. G. R. Ricker & R. K. Vanderspek (New York: AIP), 244

- Klebesadel, R., Strong, I. & Olson, R. 1973, *ApJ* 182, L85
- Kobulnicky, H. A., Kennicutt, R. C., & Pizagno, J. L. 1999, *ApJ* 514, 544
- Kobulnicky, H. A. & Kewley, L. J. 2004, *ApJ* 617, 240
- Krühler, T. 2006, Diploma Thesis, Technical University of Munich
- Kuchinski L. E., Terndrup, D. M., Gordon, K. D., Witt, A. N. 1998, *AJ* 115, 1438
- Küpcü Yoldaş, A., Greiner, J. & Perna, R. 2006, *A&A* 457, 115
- Lazzati, D., Perna, R. 2002, *MNRAS* 330L, 383
- Lazzati, D. 2005, *NCimC* 28, 575
- Le Floch, E., Duc, P.-A., Mirabel, I. F. et al. 2003, *A&A* 400, 127
- Leggett S.K., Golimowski D.A., Fan X., Geballe T.R., Knapp G.R., 2003, in "Cool stars, stellar systems and the Sun", Proc. 12th Cambridge workshop, University of Colorado, p. 120
- Lilly, S. J., Le Fèvre, O., Hammer, F., & Crampton, D. 1996, *ApJ* 460, L1
- Lundqvist, P., Fransson, C. 1996, *ApJ* 464, 924
- Madau, P., Pozzetti, L., & Dickinson, M. 1998, *ApJ* 498, 106
- Madau, P. et al. 1996, *MNRAS* 283, 1388
- Malesani, D., Tagliaferri, G., Chincarini, G. et al. 2004, *ApJ* 609, 5
- Maraston, C. 1998, *MNRAS* 300, 872
- Maraston, C. 2005, *MNRAS* 362, 799
- Matheson, T., Garnavich, P. M., Stanek, K. Z. et al. 2003, *ApJ* 599, 394
- Mathis, J. S. 1970, *ApJ* 159, 263
- Mészáros, P., & Rees, M. 1997, *ApJ* 476, 232
- Miller, G. E., & Scalo, J. M. 1979, *ApJS* 41, 513
- Mirabal, N., Halpern, J. P., Chornock, R. et al. 2003, *ApJ* 595, 935
- Mirabal, N., Halpern, J. P., An, D., Thorstensen, J. R., Terndrup, D. M. 2006, *ApJ* 643, 99
- Nagayama, T., Nagashima, C., Nakajima, Y. et al. 2003, Proc. SPIE 4841, 459
- Ochsenbein, F., Bauer, P., Marcout, J. 2000, *A&AS* 143, 221

- Osterbrock, D. E. 1989, *Astrophysics of gaseous nebulae and active galactic nuclei*, University Science Books
- Paczynski, B., & Rhoads, J. 1993, *ApJ* 418, L5
- Peng, C. Y., Ho, L. C., Impey, C. D., & Rix H-W. 2002, *AJ* 124, 266
- Perna, R., Loeb, A. 1998, *ApJ* 501, 467
- Perna, R., Raymond, J. & Loeb, A. 2000, *ApJ* 533, 658
- Persson, S. E., Aaronson, M., Cohen, J. G., Frogel, J. A., Matthews, K. 1983, *ApJ* 266, 105
- Petrosian, V. 1976, *ApJ* 209, L1
- Pian, E., Mazzali, P. A., Masetti, N. et al. 2006, *Nature* 442, 1011
- Pierini D., Gordon K. D., Witt A. N. 2003, in *Galaxy Evolution: Theory & Observations*, eds. V. Avila-Reese, C. Firmani, C. S. Frenk & C. Allen, *RMxAC*, 17, p. 200
- Pierini, D., Maraston, C., Bender, R., Witt, A. N. 2004a, *MNRAS* 347, 1
- Pierini, D., Gordon, K. D., Witt, A. N., Madsen, G. J. 2004b, *ApJ* 617, 1022
- Piro, L. 2001, *GCN Circ.* 1147
- Piro, L., De Pasquale, M., Soffitta, P. et al. 2005, *ApJ* 623, 314
- Preece, R. D., Briggs, M. S., Mallozzi, R. S. et al. 2000, *ApJS* 126, 19
- Press, W. H., Teukolsky, S. A., Vetterling, W. T., Flannery, B. P. 2002, *Numerical Recipes in C*, 2nd Ed. (USA: Cambridge University Press)
- Price, P. A., Berger, E., Reichart, D. E. et al. 2002, *ApJ* 572, L51
- Prochaska, J. X., Bloom, J. S., Chen, H.-W. et al. 2006, *ApJ* 642, 989
- Rau, A., Salvato, M., Greiner, J. 2006, *A&A* 444, 425
- Ravindranath, S., Ferguson, H.C., Conselice, C. et al. 2004, *ApJ* 604, L9
- Rees, M. J. & Meszaros, P. 1992, *MNRAS* 258, 41
- Rees, M. J. & Meszaros, P. 1998, *ApJ* 496, L1
- Reeves, J. N., Watson, D., Osborne, J. P., Pounds, K. A., O'Brien, P. T. 2003, *A&A* 403, 463
- Reid, I.N., Kirkpatrick, J.D., Gizis, J.E., et al. 2000, *AJ* 119, 369
- Reichart, D., Nysewander, M., Moran, J. et al. 2005, *NCimC* 28, 767

- Robin, A. C., Reylé, C., Derrière, S. & Picaud, S. 2003, *A&A* 409, 523
- Rola, C. S., Terlevich, E., Terlevich, R. J. 1997, *MNRAS* 289, 419
- Sahu, K. C., Vreeswijk, P., Bakos, G. et al. 2000, *ApJ* 540, 74
- Salpeter, E. 1955, *ApJ*, 121, 161
- Sari, R., & Piran, T. 1997, *ApJ*, 485, 270
- Sari, R., Piran, T. & Narayan, R. 1998, *ApJ* 497, L17
- Savaglio, S. & Fall, S. M. 2004, *ApJ* 614, 293
- Schlegel, D. J., Finkbeiner, D. P., & Davis, M. 1998, *ApJ* 500, 525
- Schechter, P. L., Mateo, M., Saha, A. 1993, *PASP* 105, 1342
- Sersic, J. L. 1968, *Atlas de Galaxias Australes* (Cordoba: Obs. Astron.)
- Shull, J. M., McKee, C. F. 1979, *ApJ* 227, 131
- Spergel, D. N., Bean, R., Dore, O. et al. 2006, astro-ph/0603449
- Sokolov, V. V., Fatkhullin, T. A., Castro-Tirado, A. J. et al. 2001, *A&A* 372, 438
- Sollerman, J., Östlin, G., Fynbo, J. P. U. et al. 2005, *New Astr.* 11, 103
- Sonneborn, G., Fransson, C., Lundqvist, P. et al. 1997, *ApJ* 477, 848
- Stanek, K. Z., Matheson, T., Garnavich, P. M. et al. 2003, *ApJ* 591, L17
- Steiner, I. 2005, Diploma Thesis, University of Dortmund
- Tagliaferri, G., Antonelli, L. A., Chincarini, G. et al. 2005, *A&A* 443, L1
- Takagi, T., Arimoto, N., Vansevicius, V. 1999, *ApJ* 523, 107
- Temporin, S. G. 2001, PhD Thesis, Leopold-Franzens-Universität Innsbruck (Austria)
- Tokunaga A.T., 2000, in Allen's "Astrophysical Quantities", 4th edition, ed. A.N. Cox, Springer-Verlag, NY, p. 143
- van Paradijs, J., Groot, P. J., Galama, T. et al. 1997, *Nature* 386, 686
- Vijh, U., Gordon, K. D., Witt, A. N. 2003, *ApJ* 587, 533
- Vreeswijk, P., Fruchter, A., Kaper, L. et al. 2001a, *ApJ* 546, 672
- Vreeswijk, P., Fender R. P., Garrett, M. A. et al. 2001b, *A&A* 380, L21
- Wainwright, C., Berger, E., & Penprase, B. E. 2005, *AAS* 207, 1908

- Watanabe, M., Nakaya, H., Yamamuro, T. et al. 2005, *PASP* 117, 870
- Watson, D., Reeves, J. N., Osborne, J. et al. 2002, *A&A* 393, L1
- Waxman, E. 1997, *ApJ* 485, L5
- Wijers, A. M. J., Rees, M. J., & Mészáros, P. 1997, *MNRAS* 288, L51
- Willott, C. J., Delfosse, X. Forveille, T. et al. 2005, *ApJ* 633, 630
- Witt, A. N., Gordon, K. D. 2000, *ApJ* 528, 799
- Woosley, S. E. 1993, *ApJ* 405, 273
- Woosley, S. E. & Heger, A. 2006, *ApJ* 637, 914
- Wyithe, J. S. B. & Loeb, A. 2002, *ApJ* 581, 886
- Wyrzykowski, L., Stanek, K. Z., & Garnavich, P. M. 2001, *GCN Circ.* 1150
- Yoon, S. C., Langer, N. 2005, *A&A* 443, 643
- Zaritsky, D., Kennicutt, R. C., & Huchra, J. P. 1994, *ApJ* 420, 87
- Zeh, A., Klose, S., Hartmann, D. H. 2004, *ApJ* 609, 952
- Zerbi, F. M., Chincarini, G., Ghisellini, G. et al. 2004, *Proc. SPIE*, 5492, 1590
- Zhang, W., Woosley, S. E., MacFayden, A. I. 2003, *ApJ* 586, 356

Acknowledgements

This thesis would have not been possible without the support and contributions of numerous people and organizations to whom I would like to express my gratitudes:

Prof. Günther Hasinger for providing me the opportunity to work at MPE, and for his guidance and support on the development of this work.

Jochen Greiner for being my supervisor; for all his guidance, support and good cheer despite his busy schedule, and for encouraging me for independent research and a fruitful scientific career.

My husband and my colleague Abdullah Yoldaş for being my companion, my road friend, my “yoldaş”, and for always being resolute in questioning, wondering, and hard-working, and thus reminding me of the importance and enthusiasm of this work.

Daniele Pierini, Rosalba Perna, Mara Salvato, Arne Rau and Elena Pian, for their contributions to the work presented in this thesis and for the fruitful discussions.

IMPRS for the scholarship that financially enabled my PhD studies at MPE, for interesting lectures, and for providing the opportunity to meet with other students who later compromised most of my friends.

The Gamma group, for their support, interest and for delicious cakes.

Sheila McBreen for the language editing and for helpful suggestions on the layout of this thesis.

Prof. Ali Alpar, my masters supervisor Şölen Balman, the Astrophysics group at METU and its former members who are now all over the world, for their support that helped initiating my PhD studies at MPE.

In addition, I would like to thank to my friends Almudena, Ayşe, Paola and Cecilia for sharing the good and bad days of my PhD with me in Munich; I have always felt their support. I would also like to thank to my dear close relatives, my parents-in-law and brother-in-law for their support. Finally and inevitably, I would like to thank my mother Şenay Küpcü, my father Hakkı Küpcü, who was my only supporter when I decided to study Physics, and my brother Alptekin Küpcü, for their support and belief, and for showing the patience that every PhD student needs.